

A Six-Degree-of-Freedom Compliant Micro-Manipulator  
for Silicon Optical Bench

by

Shih-Chi Chen

B.S. with highest distinction, Power Mechanical Engineering  
National Tsing Hua University (Taiwan), 1999

Submitted to the Department of Mechanical Engineering  
in Partial Fulfillment of the Requirements for the Degree of

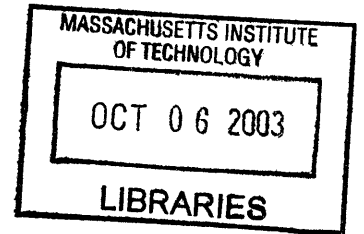
Master of Science in Mechanical Engineering

at the

Massachusetts Institute of Technology

September 2003

© 2003 Massachusetts Institute of Technology  
All Rights Reserved



Signature of Author.....  
Department of Mechanical Engineering  
August 8, 2003

Certified by.....  
Martin L. Culpepper  
Assistant Professor of Mechanical Engineering  
Thesis Supervisor

Accepted by.....  
Ain A. Sonin  
Chairman, Department Committee on Graduate Students

A Six-Degree-of-Freedom Compliant Micro-Manipulator  
for Silicon Optical Bench

by

Shih-Chi Chen

Submitted to the Department of Mechanical Engineering  
on August 8, 2003 in Partial Fulfillment of the  
Requirements for the Degree of  
Master of Science in Mechanical Engineering

ABSTRACT

The concept of the Micro-Hexflex originated from the HexFlex™, a monolithic six-degree-of-freedom compliant mechanism. The Micro-Hexflex—a miniaturized version of HexFlex—uses sandwich structures with U-shaped electro-thermal actuators to achieve six-axis displacement via in-plane actuators. The Micro-Hexflex is designed to maneuver an optical fiber, but it can also be applied to other communication technologies.

This thesis describes the development of a six-degree-of-freedom actuator concept that provides simultaneous in-plane and out-of-plane displacement. Thermal actuation is achieved by using two identical silicon layers joined by thermal oxide. Accordingly, the device creates out-of-plane displacement when the actuators of a single layer are energized. In-plane motion is achieved by actuating both layers simultaneously. The thickness of each layer, on the order of five microns, controls the maximum out-of-plane displacement.

The Micro-Hexflex has a predicted working volume of  $5 \times 5 \times 3$  cubic microns and a force output of 200 micro-Newtons. A macro-scale model was built and tested. The macro-scale model has demonstrated linearity over the 50 cubic microns testing volume. The experimental results agree with the finite element analysis to within 7 percent error.

Thesis Supervisor: Martin L. Culpepper  
Title: Assistant Professor of Mechanical Engineering

# Acknowledgements

---

First I would like to acknowledge Professor Martin Culpepper for giving me the opportunity to work on this challenging and stimulating project at my second year at MIT. Marty has been an excellent advisor to work for and with. From him, I not only obtain the scientific and engineering knowledge but most importantly the ways to perceive things and solve a problem. Marty passes me a TREASURE BOWL. He is my teacher, my mentor, and my friend.

Thanks to all the fellow labmates in PSDAM, past and now. I really owe you a lot. Thanks to Gordon and Patrick who always pay attention to my questions and being reachable at every midnight. You're the spirit of PSDAM. Thanks to Hinmeng, Tzu Liang and Naomi, who supported and encouraged me through most of my master's period. The conversations we had, from the evolution theory to the tasty restaurants in Boston, were always fun and inspiring. Also, thanks to Dariusz and Spencer, the new blood joining PSDAM, who gave me a lot of useful advices on compiling the thesis and finishing and final testing.

I would like to pay special thanks to Professor Carol Lovemore and the staffs in Micro System Laboratory—Kurt Broderick, Vicky Diadiuk, Dave Terry, just to name a few. Without their valuable experiences and training, I would never learn the sophisticated micro-fabrication process.

Finally, I'd like to thank my parents, Mou and Polly, my brother Mu-Fan, my grand parents, and my lovely girlfriend Ting-Fang for their unbounded love and support.

# Contents

---

Abstract .....	2
Acknowledgements .....	3
Contents .....	4
Figures .....	8
Tables .....	12
Chapter 1 Introduction .....	14
1.1 Background .....	14
1.1.1 The need for precision alignment.....	16
1.2 Active Alignment Technology .....	18
1.3 The Micro-Hexflex Manipulator.....	20
1.4 Thesis overview.....	21
Chapter 2 Theory and Design .....	22
2.1 System Requirements.....	22
2.2 Design of Prototype: Micro-Hexflex.....	28
2.2.1 Design Schematic .....	28
2.2.2 Actuator Design.....	29
2.2.2.1 Self-Heating Effect.....	34

2.2.2.2	Hear Conduction, Convection, and Thermal radiation consideration .....	38
2.2.2.3	Finite Difference Temperature Static Solution .....	40
2.2.2.4	Finite Difference Temperature Transient Solution .....	45
2.2.2.5	Dimensional analysis.....	50
2.2.2.6	Finite element Solution from COSMOS Works .....	55
2.2.3	In-Plane Compliant Mechanism Design .....	59
2.2.4	Out-of-Plane Actuation Design.....	64
2.3	Fixation Design .....	70
2.4	Packaging .....	73
Chapter 3	Device Fabrication .....	75
3.1	Review of Micro-Fabrication Process to be Used.....	77
3.1.1	Wafers .....	77
3.1.2	Lithography .....	78
3.1.3	Metal Evaporation .....	81
3.1.4	Etching .....	81
3.1.4.1	Wet etching .....	81
3.1.4.2	Dry etching.....	83
3.1.4.2.1	Deep Reactive Ion Etching (DRIE).....	83

3.2 Design of Fabrication Process.....	85
3.2.1 Single Layer Prototype Fabrication.....	85
3.2.2 Double Layer: 6DOF Micro-Hexflex.....	88
3.3 Fabrication Considerations.....	92
3.3.1 Stiction effect .....	92
3.3.2 Variations .....	93
3.3.2.1 Pattern Transfer of Photoresist.....	93
3.3.3 Alternative Fabrication Process .....	94
3.4 Summary .....	95
Chapter 4 Testing and Characterization.....	96
4.1 Proposed Testing Setup for Micro-Hexflex .....	96
4.1.1 Static Response .....	96
4.1.2 Dynamic Response.....	96
4.2 Testing of Macro-Scale Hexflex .....	98
4.3 Macro-Scale Model Testing Setup.....	100
4.4 Test Result from the Macro Model .....	102
Chapter 5 Market Analysis .....	105
5.1 Potential Market .....	105
5.2 Budget Analysis of Mass Fabrication: Micro-Hexflex .....	107

5.2.1 Case Study.....	109
Chapter 6 Summary .....	110
6.1 Summary and Conclusion .....	110
6.2 Future Work .....	110
6.2.1 Single Mode Fiber Equations .....	115
References .....	111
Appendix A Single Mode and Multi Mode Fiber Equation.....	114
Appendix B Macro-Version Hexflex Drawing .....	117

# List of Figures

---

Figure 1-1 Typical optoelectronic system structure.....	16
Figure 1-2 Examples of V-groove and diluted waveguide .....	17
Figure 1-3 A micro- assembly of an active alignment package.....	18
Figure 1-4 Demonstration of Hexflex displacement generation .....	20
Figure 2-1 A fiber placed in V-groove which connects to other optical elements.....	22
Figure 2-2 Six possible misalignments that might cause .....	25
Figure 2-3 Insertion loss versus misalignment.....	26
Figure 2-4 Demonstration of different micro-actuators .....	33
Figure 2-5 Lumped model for a resistor with a current input. ....	35
Figure 2-6 Lumped model for a resistor with a voltage input.....	36
Figure 2-7 A U-shaped electrothermal actuator and its lump model .....	40
Figure 2-8 Dimension of a u-shaped electrothermal actuator .....	42
Figure 2-9 Plot of 1D finite difference solution.....	44
Figure 2-10 A Matlab plot of 1D finite difference solution with variable beam width (w step =0.1 $\mu$ m) .....	45
Figure 2-11 Finite difference temperature transient Solution .....	46
Figure 2-12 A Matlab plot of transient time solution of thin beam (Voltage=10V).....	50



Figure 2-13 Length(L),Gap(G),Neck(N),Width(W), and Thickness (H) .....	51
Figure 2-14 Dimensional analysis from (a) to (g).....	53
Figure 2-15 Mesh (52136 elements, 12833 corner nodes, 254982 D.O.F.).....	55
Figure 2-16 Thermal solution of conduction case and conduction/ convection case.....	56
Figure 2-17 Thermal solution with conduction, convection, and radiation effects.....	57
Figure 2-18 Stress and strain results .....	57
Figure 2-19 Displacement (exaggerated by factor of 20) .....	58
Figure 2-20 Concept of the in-plane compliant mechanism .....	59
Figure 2-21 Different designs of in plane compliant mechanisms.....	61
Figure 2-22 Optimized in plane compliant mechanism .....	62
Figure 2-23 Sandwich model and its mesh .....	64
Figure 2-24 Temperature solution of sandwich structure .....	65
Figure 2-25 Out-of-plane actuation (exaggerated by factor of 25).....	65
Figure 2-26 A demonstration of out-of-plane actuation. (exaggerated).....	66
Figure 2-27 Fiber loaded (pivoted at 10 mm) .....	67
Figure 2-28 Demonstration of 6 degree of freedom.....	67
Figure 2-29 Device thickness versus out of plane motion .....	68
Figure 2-30 A front view demonstration of Micro-Hexflex. (Diameter = 1mm) .....	70
Figure 2-31 A cross section of the Micro-Hexflex from (Figure 2-30 (b)).....	71

Figure 2-32 Step 1 and step 2.....	71
Figure 2-33 Step 3 to step 6 .....	72
Figure 2-34 Top view and back view of the Micro-Hexflex die.....	74
Figure 2-35 Original die of Micro-Hexflex and its packaging.....	74
Figure 3-1 Fabrication flow chart.....	76
Figure 3-2 Standard lithography process (in yellow area) .....	79
Figure 3-3 Buffered Oxide Etch (BOE) releases the oxide underneath the hot beam .....	83
Figure 3-4 Top view of prototype 1 .....	87
Figure 3-5 Picture of Micro-Hexflex .....	91
Figure 3-6 Comparison of different exposure time of photoresist .....	94
Figure 4-1 Testing setup for Micro-Hexflex .....	96
Figure 4-2 Computer Microvision System Setup [30].....	97
Figure 4-3 Exploded view of macro-scale testing model.....	99
Figure 4-4 Macro-scale model testing setup .....	100
Figure 4-5 Macro-scale model system setup.....	101
Figure 4-6 Y axis output original data .....	102
Figure 4-7 Y axis output displacement after backlash compensation .....	103
Figure 4-8 Z axis output displacement.....	104
Figure 4-9 Z axis rotational output.....	104

Figure 5-1 Comparison of optical fiber assembly cost ..... 105

Figure 5-2 Boeing’s in-package micro-aligner compared to a dime [34] ..... 109

# List of Tables

---

Table 1-1 Optoelectronics compared to electronics (coaxial cable) .....	15
Table 1-2 Digital telephone transmission rates .....	16
Table 2-1 Basic information for a single mode optical fiber. ....	23
Table 2-2 Error from fiber geometry.....	23
Table 2-3 Error from planar waveguide geometry.....	24
Table 2-4 Error from thermal effect.....	24
Table 2-5 Function and system requirement.....	27
Table 2-6 Actuator matrix for Hexflex .....	29
Table 2-7 Stress, strain, and power density.....	31
Table 2-8 Comments and comparison from Table 2-6and Table 2-7 .....	31
Table 2-9 Property values of single crystal silicon .....	38
Table 2-10 Conduction, convection, and radiation comparison .....	39
Table 2-11 Dimension of the lumped model in Figure 2-8(b) .....	42
Table 2-12 Properties of test parameters.....	43
Table 2-13 Thermal properties of test parameters .....	43
Table 2-14 Capacitance of test parameters .....	46
Table 2-15 Frequency analysis.....	58

Table 2-16 Compliant flexures comparison table with respect to Figure 2-21 .....	61
Table 2-17 Micro-Hexflex in plane displacement.....	63
Table 2-18 Micro-Hexflex predicted performance .....	63
Table 2-19 Frequency analysis.....	66
Table 2-20 Performance of Micro-Hexflex.....	68
Table 2-21 Double-layered Micro-Hexflex predicted performance .....	69
Table 3-1 Fabrication of prototype 1.....	85
Table 3-2 Fabrication of prototype 2.....	88
Table 3-3 Alternative fabrication solution for Micro-Hexflex.....	94
Table 5-1 Total world market (1997) for fiberoptic products in communication applications. CGAR= Compounded Annual Growth Rate. ....	106
Table 5-2 Cost for the material .....	107
Table 5-3 Process cost at MTL .....	107
Table 5-4 Product price estimation .....	108

# Chapter 1 Introduction

---

## 1.1 Background

Integrated circuits allow a large number of transistors to be fabricated on the same silicon wafer and enable them to be interconnected into functional circuits. Today, optoelectronics is at the same stage that electronics was twenties years ago: though high-performance optoelectronic devices have been developed, most of optical systems are assembled piece by piece. In 1969, Miller proposed the concept of “integrated optics”[1], in which he envisioned active optical devices interconnected by optical waveguides, similar to the way transistors are interconnected by wires in integrated circuits, where comes in the idea of in-package or on chip active alignment. The reason people intend to integrate the optics into electronics is because the optical elements and interconnections can avoid some fundamental drawbacks from electronics, which are listed in Table 1-1 [2].

Optical systems, unlike the electronic system can let many signal channels operate at the same time with slightly differing wavelengths (wavelength division multiplexing, WDM). Using WDM, an optical fiber, would have a theoretical maximum data capacity up to 25,000 gigabytes per second. This ultimate data capacity has not been reached; however, major advances are being made steadily. Table 1-2 shows a comparison of traditional coaxial cable and optical fiber in telephone industry. The coaxial system has long been established. The fiber optic capacities shown are for synchronous optical network (SONET). The fiber’s high bandwidth allows transmissions of signals requiring much greater bandwidth than a voice channel. Television and teleconferencing, for example, require a channel capacity 14 to 100 times that of a digitally encoded voice. The bandwidth of a fiber allows these signals to be multiplexed through the fiber, permitting voice, data, and video to be transmitted simultaneously. The demands for these services mean that fibers will move from being only long distance carriers to being carriers right to the home and business.

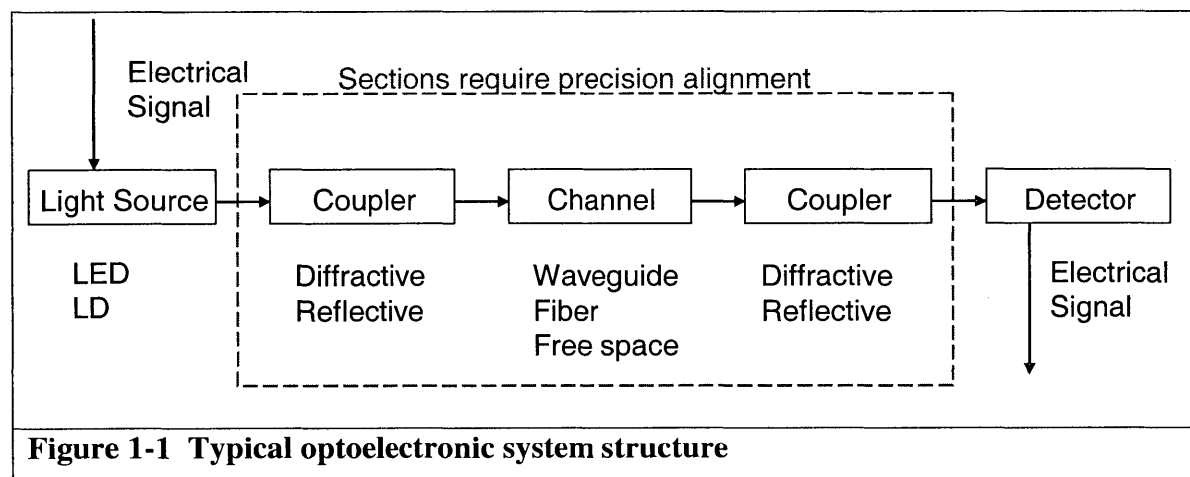
<b>Disadvantages of Electronics</b>	<b>Advantages of Optoelectronics</b>
<ol style="list-style-type: none"> <li>1. High-Power Line-Driver requirements</li> <li>2. Thermal management problems</li> <li>3. Dispersion: interconnection delay varies with frequency</li> <li>4. Attenuation: signal attenuation varies with frequency</li> <li>5. Crosstalk: capacitive and inductive coupling from signals on neighboring traces</li> <li>6. Power-Supply: noise caused by inductive and resistive voltage drops in supply lines</li> <li>7. Synchronizing problems</li> <li>8. High-Sensitivity to Electromagnetic Interference(EMI)</li> <li>9. Bulky, heavy, inflexible</li> </ol>	<ol style="list-style-type: none"> <li>1. Higher interconnection densities</li> <li>2. Higher packing densities of gates on integrated circuit chips</li> <li>3. Lower power dissipation</li> <li>4. Easier thermal management on systems</li> <li>5. Less signal dispersion than comparable electronic schemes</li> <li>6. Less signal distortion</li> <li>7. Greater immunity to EMI</li> <li>8. Higher operation speed</li> </ol>

Figure 1-1 is a typical demonstration of optoelectronic system, where the electrical signals are transformed into optical signals with a light emitting diode (LED) or a laser diode (LD). At the first coupler, the incoming signals are combined into a fiber at slightly different wavelengths. The signals then travel in the fiber, waveguide, or free space (channels) to the destiny. Finally, the signals in the channels are diffracted out from the fiber through the second coupler and transformed into electrical signals.

<b>Medium</b>	<b>Bit Rate Designation</b>	<b>[Mbps]</b>	<b>Voice Channels</b>	<b>Repeater Spacing [km]</b>
Coaxial Cable	DS-0	0.064	1	1-2
	DS-1	1.544	24	
	DS-1C	3.152	48	
	DS-2	6.312	96	
	DS-3	44.736	672	
Fiber (SONET)	OC-1	51.840	672	40 (Laser)
	OC-3	155.520	2016	
	OC-12	622.080	8064	
	OC-48	2488.320	32,256	
	OC-96	4796.640	64,512	
	OC-192	9953.280	129,024	

### 1.1.1 The need for precision alignment

Due to the geometry of optics and waveguides, precision alignment is required to a sub-micron level between the optical elements. As shown in Figure 1-1, optical elements require precision alignment. Up to now no practical solutions for active six-axis in-package alignment have been developed.

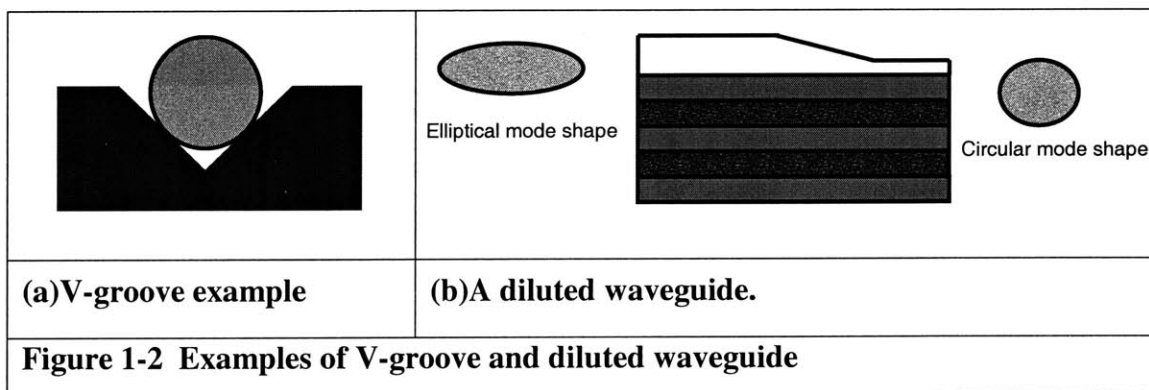


**Figure 1-1 Typical optoelectronic system structure**



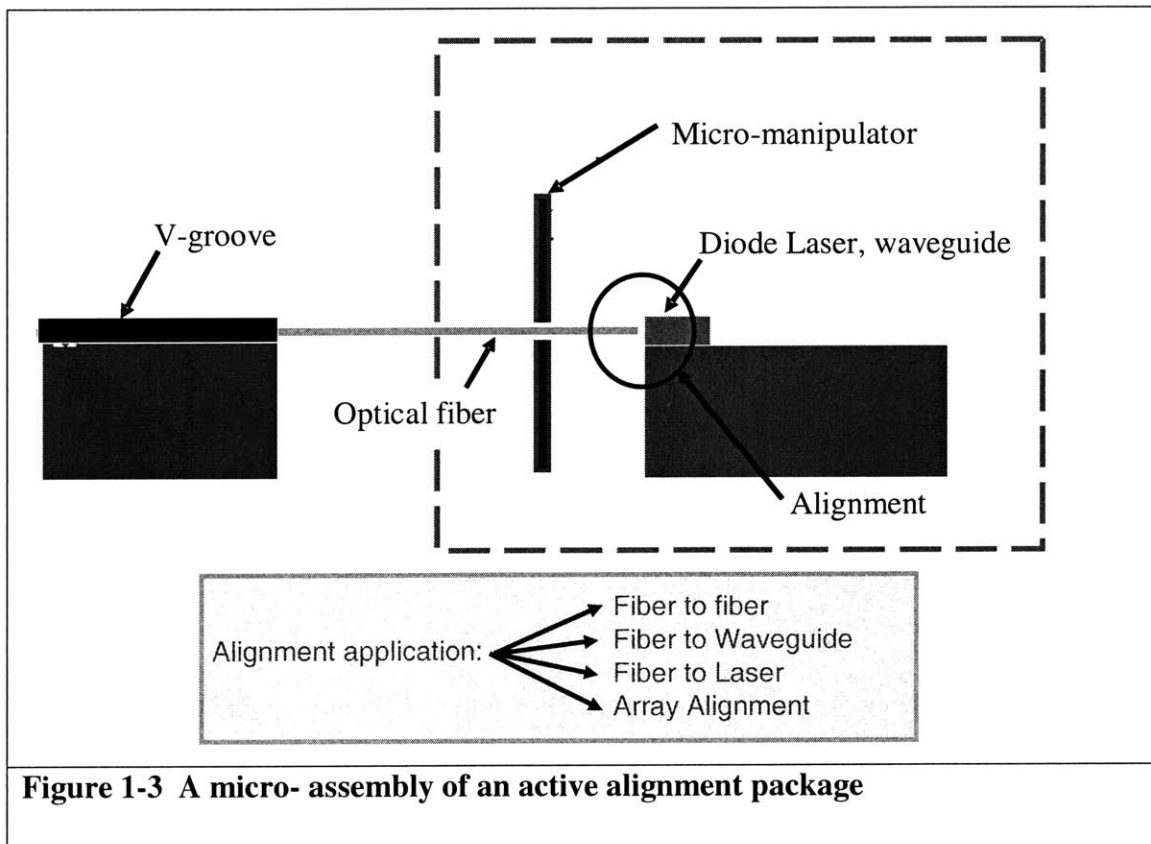
In passive alignment, silicon V-grooves (Figure 1-2 (a)) have been coupled with precision placement of solder bumps and surface tension alignment to provide one-dimensional fixturing and alignment of fibers. Although the passive alignment approach is potentially more cost-effective than active alignment, passive systems haven't achieved the manufacturing tolerances required to accurately align single mode fibers and optics. Using V-groove for laser diode to optical fiber yields misalignment of approximately 2.8 microns [3], not suitable for single mode packaging [4].

In an alternative method, one may change the waveguide so that it will not require precision alignment. For instance, to reduce the coupling loss, the concept of a tapered waveguide may be used. A tapered waveguide (diluted waveguide) changes the elliptical mode shape of a laser to a circular distribution that is compatible with a single mode optical fiber. The diluted waveguide, as shown in Figure 1-2 (b), achieves a butt coupling efficiency of 66% at a two micron misalignment [5]. Unfortunately, it is difficult and expensive to fabricate a tapered deposition layer. Furthermore, the tapered waveguide only solves the problem between waveguides and lasers. It does not address time variable errors. For the connection of other optical elements, active alignment is the only practical solution.



## 1.2 Active Alignment Technology

To achieve in-package, self-alignment, a micro-stage must work with passive alignment technology to reach the goal of integrated optics. Fortunately, this can be done by building the optical elements and active alignment mechanical components on the same silicon wafer through micro-electro-mechanical-system (MEMS) technology. Figure 1-3 shows a design concept of in-package, self-alignment as an example. Within the dashed line in Figure 1-3 is a hermetically sealed package. When a fiber is inserted to the package, a micro-manipulator can align components. The elements in the dashed line, which includes diode laser, waveguide, and micro-manipulator, are integrated and built by MEMS process.



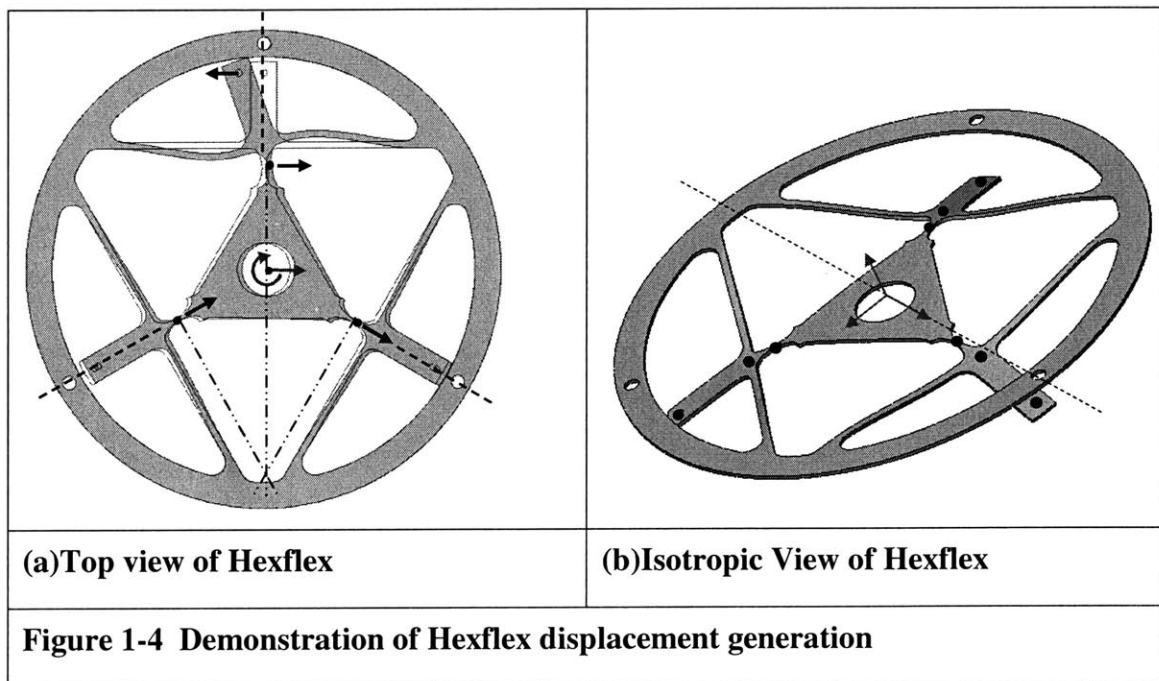
In the field of MEMS, there are many micro-actuator designs [6] [7]. For instance, a six-degree-of-freedom actuator (comb drive actuated) designed by Professor Dennis Freeman's group at MIT [8]. The purpose of this actuator is to test a nano-level, dynamic

analyzer device, called the *Computer Microvision system*, which will be mentioned in chapter four. For the purpose of fiber alignment, a device with least five-degree-of-freedom, large force, and a small packaging volume is needed. State-of-the-art MEMS actuators are generally not strong enough to hold and manipulate fibers.

In 1998, Boeing proposed a three-degree-of-freedom in-package active alignment device [9] [10], which uses MEMS three pairs of thermal actuators with a maximum output displacement range at ten microns. This is the first device that monolithically packages the active alignment system into a hermetically sealed package. There are other three-degree-of-freedom stages and actuators [11], which perform robotic mechanism. However, it is critical to develop a micro-stage with at least five-degree-of-freedom, and preferably a six-degree-of-freedom aligner. The sixth degree of freedom is needed for virtual center of rotation capability and alignment of non-axisymmetric components. For example, waveguides with eight degree taper.

### 1.3 The Micro-Hexflex Manipulator

This thesis covers the design of a micro-manipulator based on the Hexflex mechanism, depicted in Figure 1-4. The Hexflex is a planar, six-degree-of-freedom compliant mechanism for nano-manipulation [12]. Figure 1-4 (a) illustrates in-plane displacement generation via a Hexflex: The circular ring serves as the ground. When a tab is displaced in-plane, the stage will displace in-plane and rotate in a clockwise direction. Figure 1-4 (b) explains the out-of-plane displacement generation of Hexflex. When three tabs are displaced in the Z direction, the center stage will have a displacement in the Z direction. Six-degree-of-freedom displacements can be achieved by superposition of actuations from three different tabs.



The goal of the research is to develop a design for a micro-scale Hexflex, the Micro-Hexflex. The Micro-Hexflex is to provide a six-degree-of-freedom manipulation and must be able to be integrated into a silicon optical bench (SiOB).

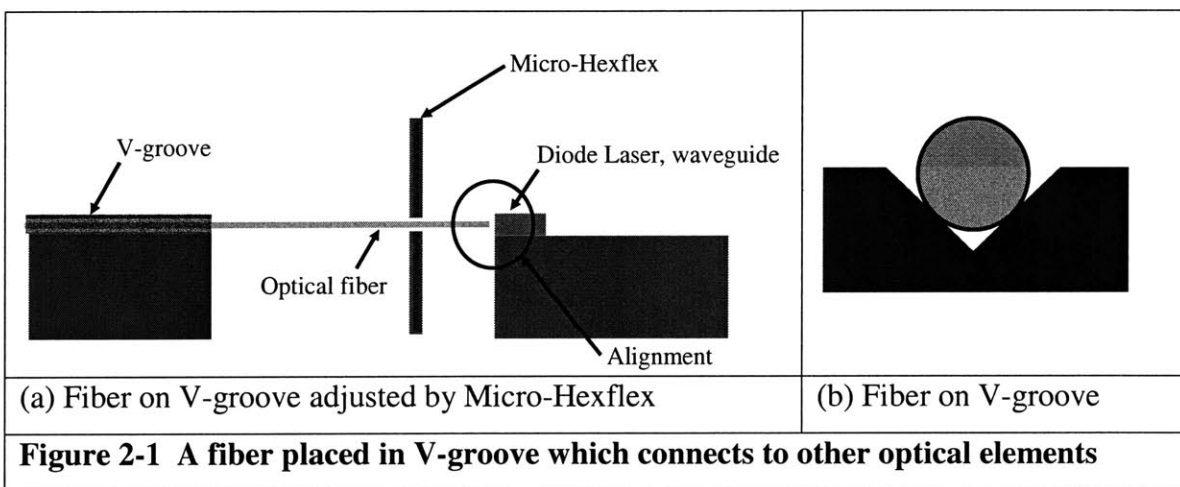
## **1.4 Thesis overview**

This thesis emphasizes the modeling/analysis, design, fabrication, and testing process of the Micro Hexflex. Chapter two presents the system requirements and the modeling/design theory of the micro-actuator. Chapter three presents fabrication methods and processes. Chapter four presents the experimental results of macro-scale, bench-level prototype. Chapter 5 presents a study of the market for the device. Chapter 6 presents the conclusion, summary, and the potential future work generated by this thesis.

# Chapter 2 Theory and Design

## 2.1 System Requirements

Consider a device wherein a fiber is placed in a V-groove. A pigtail is fixed to the Micro-Hexflex, which then connects to other optical elements, for instance, a fiber or waveguide, as shown in Figure 2-1.



To estimate the manipulation requirements of the in-package automatic alignment system, all errors should be taken into account. These errors include the variation of fiber diameter, core eccentricity, ellipticity<sup>1</sup>, and the errors in placement and orientation of the V-groove. Other errors, such as thermal errors are generally small in comparison to all

<sup>1</sup> Given a spheroid with equatorial radius  $a$  and polar radius  $c$ , the ellipticity is defined by

$$e \equiv \begin{cases} \sqrt{\frac{a^2 - c^2}{a^2}}, c < a & (\text{oblate spheroid}) \\ \sqrt{\frac{c^2 - a^2}{c^2}}, c > a & (\text{prolate spheroid}) \end{cases}$$

Ellipticity is commonly denoted using the symbols  $e$  or  $\epsilon$  (Beyer 1987).

the errors listed above. For instance, thermally induced errors are less than 1% of geometric errors. The following tables (from Table 2-1 to Table 2-4) list normal sizes and typical errors for components involve in Figure 2-1.

<b>Table 2-1 Basic information for a single mode optical fiber.</b>		
	<b>Average [micron]</b>	<b>Diameter Tolerance [micron]</b>
<b>Diameter</b>	125	+/- 1.0
<b>Core</b>	5-9	+/- 0.3

Table 2-2 lists possible error types and their typical tolerances [13].

<b>Table 2-2 Error from fiber geometry</b>			
Error Type	Tolerance [micron]	Variations [micron]	Comment
Mean Diameter	1 $\mu$ m	+/- 0.5 $\mu$ m	Causes problems in passive alignment
Core Eccentricity	0.7 $\mu$ m	~0.3 $\mu$ m	The fiber may offset or spiral in the core. There also is a sinusoidal relationship between vertical and horizontal error in core position. To estimate the error by a 0.3 $\mu$ m offset is acceptable [13].
Fiber Ellipticity	less than 1%	0.1%-0.2%	Horizontal and vertical errors are not independent. It is reasonable to assume the vertical eccentricity is less than 0.05 $\mu$ m and horizontal eccentricity is less than 0.1 $\mu$ m [13].

In Table 2-3, errors due to fabrication are considered.

	Errors [micron]	Comment
Planar Waveguide	Less than $0.5\mu\text{m}$ (with a groove width about $100\mu\text{m}$ .)	Etching process is fairly slow, thus the errors from the depth variation is well controlled.
V-groove	$0.15\mu\text{m}$	Deposition process is very slow, thus the error mainly comes from the misalignment of the mask, which is about $0.15\mu\text{m}$ at its maximum.

Now, we consider thermal effects as if there is a temperature variation within the optical alignment system. If the optical device has a length of one centimeter, the corresponding thermal expansion coefficients and strains are listed in Table 2-4. Since the error from thermal effects is about two orders smaller than other errors from Table 2-1 to Table 2-3, we will neglect the errors from thermal effect in the following section.

Material	Condition (Temperature Difference) [ $^{\circ}\text{K}$ ]	Thermal Expansion Coefficient [ $^{\circ}\text{K}^{-1}$ ]	Strain	Predicted Error [micron]
Silicon	15	$2.3 \times 10^{-6}$	$3.45 \times 10^{-5}$	$\sim 3.45 \times 10^{-3}$
Silica	15	$0.5 \times 10^{-6}$	$7.50 \times 10^{-6}$	$\sim 7.50 \times 10^{-4}$
Metal(Al)	15	$2.5 \times 10^{-5}$	$3.75 \times 10^{-4}$	$\sim 3.75 \times 10^{-2}$



The worse case geometric error,  $E_T$ , is the sum of the errors from the fiber,  $E_F$ , errors from the V-groove,  $E_V$ , and the errors from the waveguide,  $E_W$ ,

$$E_T = E_F + E_V + E_W \tag{2-1}$$

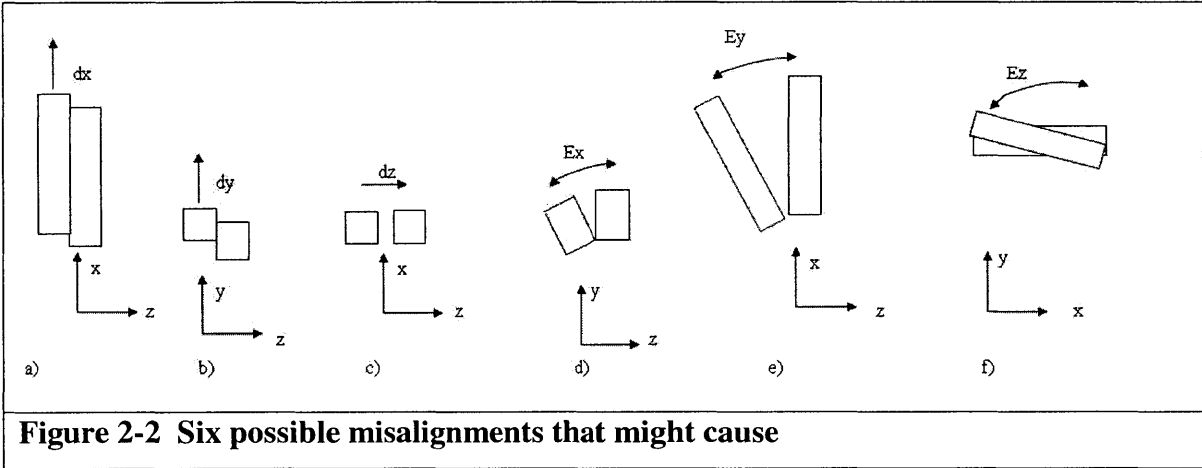
From equation (2-1), Table 2-1, and Table 2-2, we can conclude that the total lateral error is:

$$0.1\mu\text{m} < E_T < 0.5\mu\text{m} \tag{2-2}$$

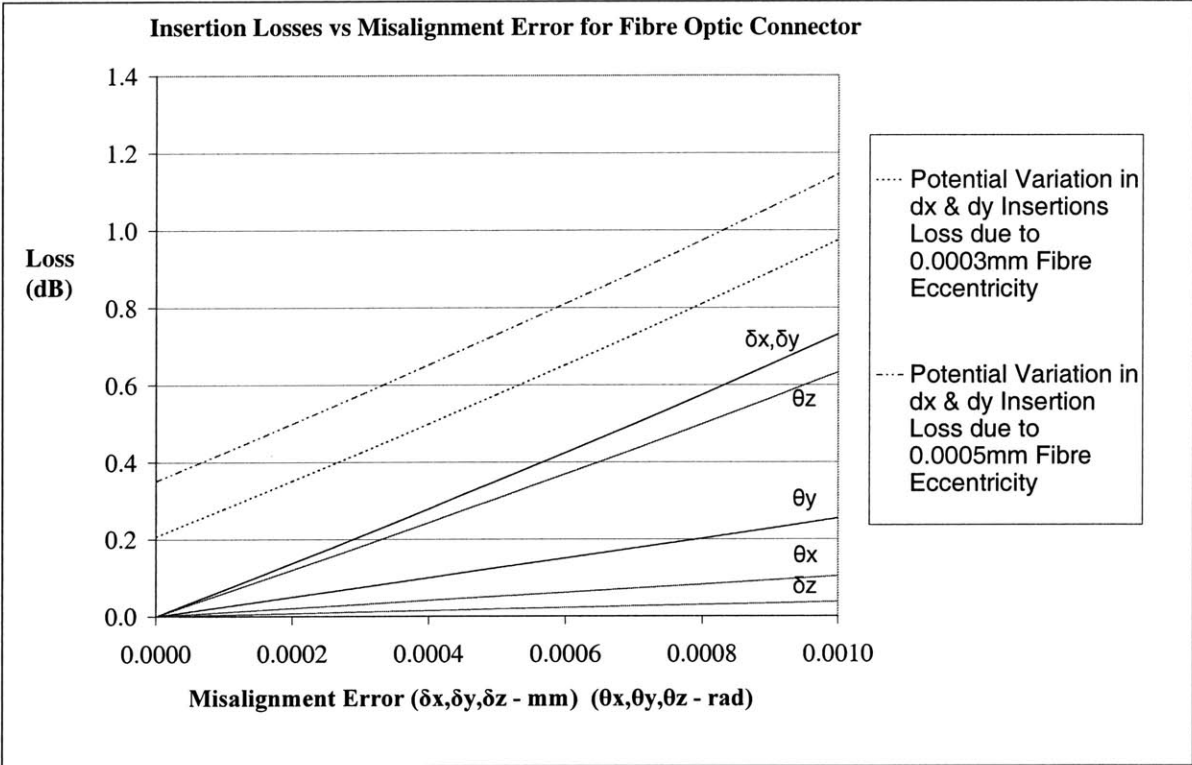
In the vertical position, the errors come from the height of the waveguide, fiber ellipticity, core eccentricity, and also the variations of the fiber diameter, thus the total error should be larger then the lateral error:

$$1.1\mu\text{m} < E_T < 1.37\mu\text{m} \tag{2-3}$$

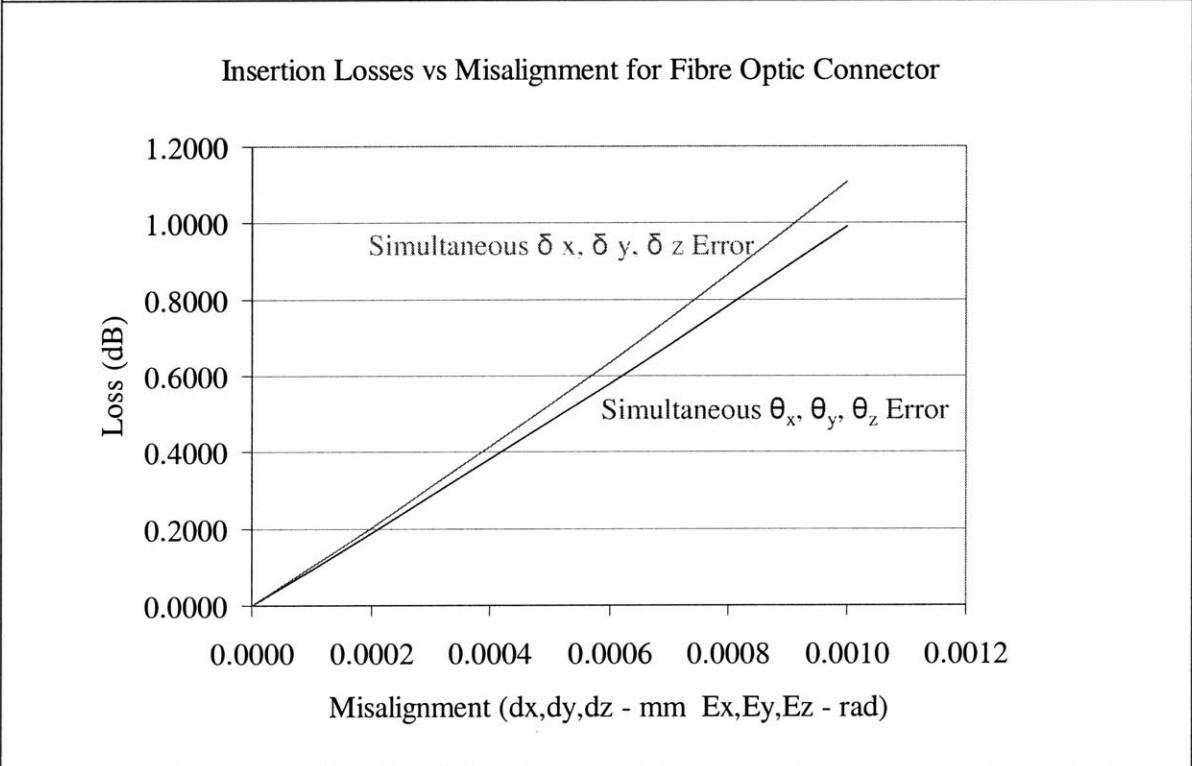
In reality coupling loss is due to misalignment in six different axes, as shown in Figure 2-2.



To calculate the sensitivity of misalignment in each degree of freedom, the single mode and multimode fiber equations [Appendix A] are used. The results are presented in Figure 2-3 (a) and Figure 2-3 (b) [14].



**(a) Insertion Loss versus Misalignment for each degree of freedom**



**(b) Insertion loss versus misalignment for fiber optic connector**

**Figure 2-3 Insertion loss versus misalignment**

Accordingly, by the combination of geometrical errors, we obtain the results for 3dB (50%) loss in Table 2-5.

<b>Table 2-5 Function and system requirement</b>					
$\delta x$ [micron]	$\delta y$ [micron]	$\delta z$ [micron]	$\theta x$ (radian)	$\theta y$ (radian)	$\theta z$ (radian)
0.5	1.0	<1	0.0087	0.0087	0.0000

## **2.2 Design of Prototype: Micro-Hexflex**

### **2.2.1 Design Schematic**

Important function requirements for this design:

1. Device size
2. Displacement
3. Output force
4. Power consumptions
5. Fixation
6. Dynamic response
7. Market driven needs
8. Cost

These important factors are discussed in detailed later in this chapter. Market and cost analysis are covered in chapter five.

The design procedure of Micro-Hexflex is listed as following:

1. Choose and design the most appropriate type of micro actuators
2. Generate concepts for the planar compliant mechanism
3. Optimize actuator and compliant mechanism to achieve required displacement and force
4. Design the out of plane motion mechanisms

### 2.2.2 Actuator Design

Micro-scale devices generally don't have space to place an external actuator, thus a built-in micro-actuator is designed with the Micro-Hexflex Stage. The following criteria were used to choose the appropriate actuators for the Micro-Hexflex,

1. An integrated circuit (IC) compatible actuating voltage, which is between 5-15V
2. Force output larger than  $170\mu\text{N}$  for moving the single mode fiber pivoted at five millimeter away
3. Displacement at least 1.5 microns to fulfill the function requirement in Table 2-5
4. Minimize device volume to lower the cost
5. Minimize switching/operating speed

The actuator comparison matrices in Table 2-6 to Table 2-8 are used to compare the candidate MEMS actuators and provide the background for discussion.

Table 2-6 provides information on actuator operating current/voltage, power, temperature, speed, displacement and resolution.

Actuation Type	Type	Time Constant [femto second]	Operating Temperature [ $^{\circ}\text{K}$ ]
Electrostatic	Comb Drive	$\sim 10\text{fs}$ (1/RC)	$\sim 300$
	Cantilever	$\sim 10\text{fs}$	$\sim 300$
Thermal	Bent-beam(V-shaped)	$\sim 1.2 \times 10^9\text{fs}$ (1.2 kHz)	$\sim 700$
	U-shaped	$\sim 0.5 \times 10^9\text{fs}$ (0.4 - 1.6 kHz)	$\sim 800$
Piezoelectric	ZnO with Al film	$\sim 10\text{fs}$	$\sim 300$
Magnetic	Self-generated B field. (Parallel current)	$\sim 10\text{fs}$	$\sim 300-400$

Actuation Type	Voltage [V]	Current [A]	Power [W]
Electrostatic (Comb drive)	~15V	No current in DC system	Very Low
Electrostatic (Cantilever)	~15V	No current in DC system	Very Low
Thermal (Bent-beam)	~30V	~8mA	~250mW
Thermal (U-shaped)	0-15V	~5mA	~50mW
Piezoelectric Actuator	~10-20V	No current	Very Low
Magnetic	~20V	~100mA	High Power (~0.1-1W)
Actuation Type	Displacement [micron]	Resolution [nm]	
Electrostatic (Comb drive)	1-2 $\mu$ m	10nm	
Electrostatic (Cantilever)	<1 $\mu$ m	10nm	
Thermal (Bent-beam)	~20 $\mu$ m	250nm	
Thermal (U-shaped)	~15 $\mu$ m	250nm	
Piezoelectric	~0.1 $\mu$ m	0.1nm	
Magnetic	~30 $\mu$ m		

Table 2-7 compares the micro-actuator, piezoelectric actuator, human muscle, and shape memory alloy.

<b>Table 2-7 Stress, strain, and power density</b>			
Actuation Type	Stress(MPa)	Strain (%)	Strain Rate(Hz)
Electrostatic	~0.04	>10	>1
Cardiac Muscle (human)	0.1	>40	4
Piezoelectric Polymer (PVDF)	3	0.1	>1
Shape memory alloy (NiTi bulk fiber)	>200	>5	3
Actuation Type	Power Density [W/Kg]	Efficiency [%]	
Electrostatic	>10	>20	
Cardiac Muscle (human)	>100	>35	
Piezoelectric Polymer (PVDF)	>100	<1	
Shape memory alloy (NiTi bulk fiber)	>1000	>3	

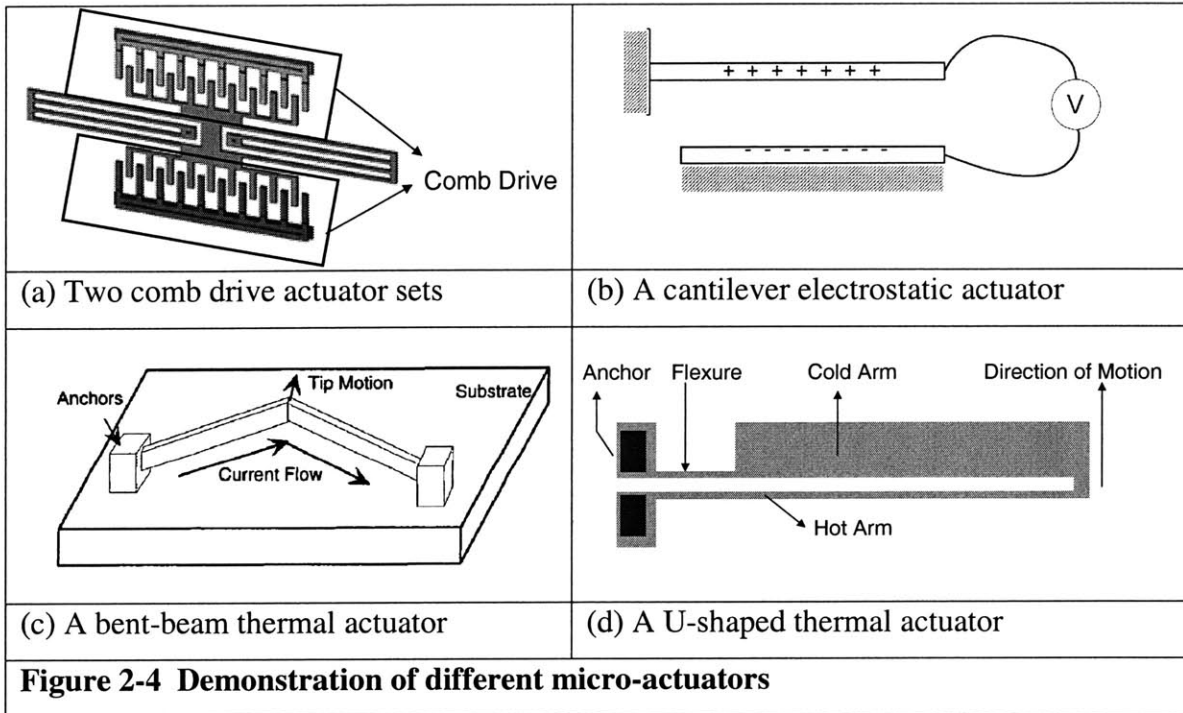
Conclusion and comments from Table 2-6 and Table 2-7 are summarized in Table 2-8.

<b>Table 2-8 Comments and comparison from Table 2-6 and Table 2-7</b>		
Actuation Type	Comments	Drawback
Electrostatic (Comb drive)	Fast response  Low power low temperature  High resolution	Large working area  Low force density compared to cantilever type.
Electrostatic (Cantilever)	Fast response  Low power low temperature  High resolution	Low force compared to electro-thermal actuator

Thermal (Bent-beam)	Large force	Need more space compared with U-shaped thermal actuator
Thermal (U-shaped)	IC compatible Large force Simple fabrication process	High power Slow reaction
Piezoelectric	High Bandwidth High energy density High Stress(tens of MPa)	Complex fabrication process Low strain and displacement
Magnetic	Ability to attract and repel High force	High power consumption Unintended interactions

The electric comb drive actuator, shown in Figure 2-4 (a), has the longest and the most stable working distance. However, it is difficult to use the comb drive to design a powerful six-degree-of-freedom mechanism. Because of its lower power density compared to other actuators in Table 2-6 and Table 2-7, the comb drive must occupy a larger area. Therefore, the comb drive will not fulfill the function requirement of the Micro-Hexflex, which necessitates a minimized die area. Although the cantilever electrostatic actuator, shown in Figure 2-4 (b), has a suitable working area due to a denser power concentration, it has an effective, stable working distance of only two microns, which also does not satisfy the functional requirement for the Micro-Hexflex.





A piezoelectric actuator has sufficient force output; however, its stroke (nanometer level) is too small for fiber alignment. Complex force amplification mechanism through thin piezoelectric film for six-degree-of-freedom actuation is not effective and practical.

A thermal actuator will provide enough force output and displacement (up to 10 micron). Accordingly, it is the most appropriate MEMS actuator for in-package fiber alignment. A bent-beam actuator, as shown in Figure 2-4(c) has sufficient force output. The stroke for a chevron thermal actuator is ten times smaller than that of a comparably sized U-shaped thermal actuator [15]. Arrays of U-shaped thermal actuators of different lengths and sizes had been built to find the maximum force output, load, and maximum displacement by Comtois in 1997 [16] [17]. For fiber alignment, this actuator needs a thicker structure to handle a fiber. In order to fully understand and thus optimize the thermal actuator, an analytical thermal model for Joule heating and kinematic modeling will be used to predict actuator performance.

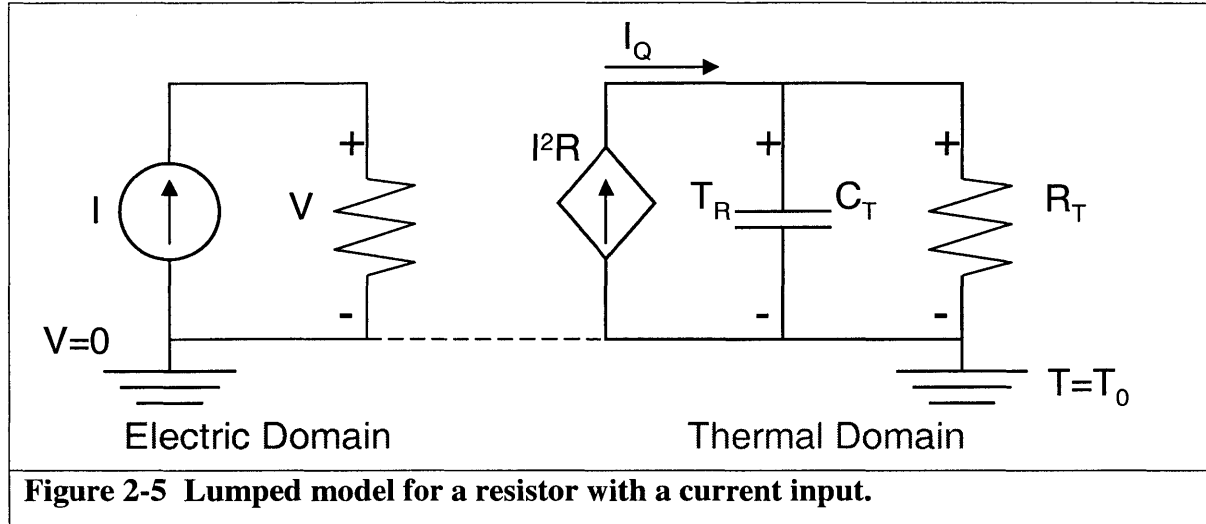
### 2.2.2.1 Self-Heating Effect

As shown in Figure 2-4 (d), a U-shaped thermal actuator consists of a thin beam connected from the current source, a thick beam on the top, and a thin neck which connects the thick beam to the ground. When a current runs through the thermal actuator, the thin beam heats up and elongates, thereby inducing displacement shown in Figure 2-4 (d).

The thermal actuator must be controlled to avoid an instability, which will result in a burnout. We know that the value of any non-perfect resistance will vary with changing temperature. The definition of temperature coefficient of resistance, TCR, is an important indication of this property. For moderate temperature variation, we can use a linear model to simulate the behavior of a resistance: [18]

$$R = R_0[1 + \alpha_R(T_R - T_0)] \quad (2-4)$$

where  $R_0$  is the resistance at the reference temperature  $T_0$ ,  $R$  is the resistance at temperature  $T_R$ , and  $\alpha_R$  is the temperature coefficient of resistance, which typically is positive for metals and can be either positive or negative for semiconductors. To determine whether the resistor is operated in the stable regime, two linear lumped models will be discussed here. The first one in Table 2-5 represents a lumped element model of a current running through a resistor. The electric model contains a current source and a resistor, where the voltage across the resistor is  $V$ .



**Figure 2-5 Lumped model for a resistor with a current input.**

In the thermal domain, there are three elements, a dependent current source which represents the Joule heating power  $I^2R$ , a capacitor which represents the heat capacity of the resistor, and a thermal resistor  $R_T$  representing the heat conduction from the resistor to a thermal reservoir held at temperature  $T_0$ . The current variable  $I_Q$ , which represents the energy flow, in the thermal circuit has the dimension of power. The ground symbol at the thermal circuits denotes the reference temperature  $T_0$ . Thus, according to the knowledge in system dynamics, we know the voltage across the thermal capacitor  $C_T$  is the temperature difference  $T_R - T_0$ , however, for the convenience in the following analysis,  $T_0$  is set be zero. From energy conservation theory:

$$C_T \frac{dT_R}{dt} = -\frac{T_R}{R_T} + I^2 R_0 (1 + \alpha_R T_R) \quad (2-5)$$

Collecting the terms, this simplifies to:

$$\frac{dT_R}{dt} = -\frac{1}{R_T C_T} (1 - \alpha_R R_0 R_T I^2) T_R + \frac{I^2 R_0}{C_T} \quad (2-6)$$

This is a first order system with input  $I^2 R_0 / C_T$ . The time constant of the system is given as:

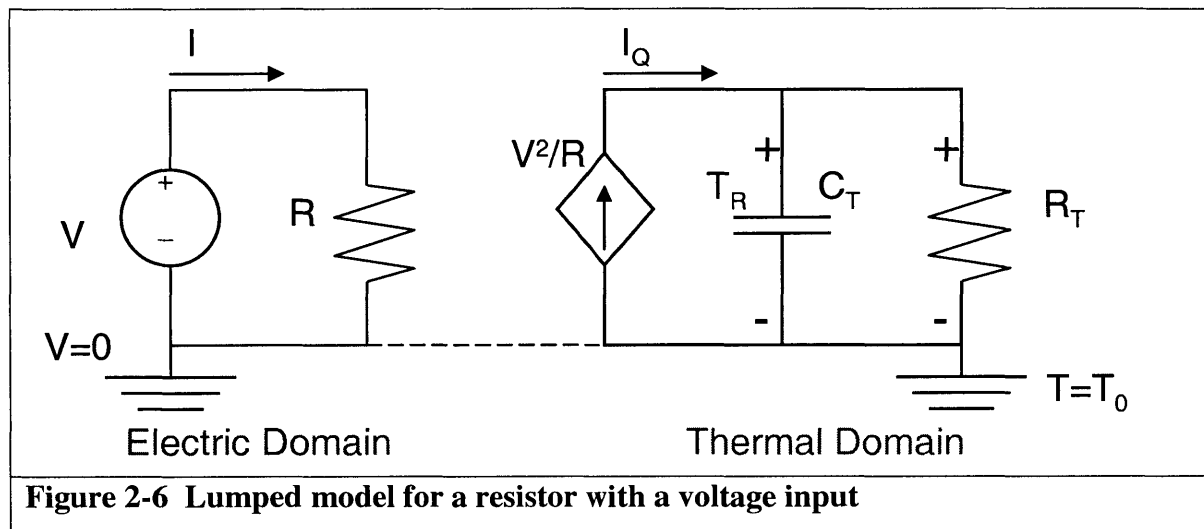
$$\tau_I = \frac{R_T C_T}{1 - \alpha_R R_0 R_T I^2} \quad (2-7)$$

The steady state temperature rise  $T_{SS}$  is

$$T_{SS} = \frac{R_0 R_T I^2}{1 - \alpha_R R_0 R_T I^2} \quad (2-8)$$

If the temperature coefficient of a resistor is positive, then using a current source might result in a fusing effect that will damage the device.

We now consider using a Voltage source to energize the actuator. As shown in Figure 2-6, the system model will change and thus have a different governing equation:



**Figure 2-6 Lumped model for a resistor with a voltage input**

$$C_T \frac{dT_R}{dt} = -\frac{T_R}{R_T} + \frac{V^2}{R_0(1 + \alpha_R T_R)} \quad (2-9)$$

If we assume that the total change in resistance is small; we can linearize the model by expanding the denominator to yield

$$\frac{V^2}{R_0(1 + \alpha_R T_R)} \approx \frac{V^2}{R_0} (1 - \alpha_R T_R) \quad (2-10)$$

By substituting and collecting terms, we have

$$\frac{dT_R}{dt} = -\frac{1}{R_T C_T} \left(1 + \frac{\alpha_R R_T V^2}{R_0}\right) T_R + \frac{V^2}{R_0} \quad (2-11)$$

Again, the time constant in this first order system can be derived as

$$\tau_V = \frac{R_T C_T}{1 + \frac{\alpha_R R_T V^2}{R_0}} \quad (2-12)$$

The steady temperature rise  $T_{SS}$  is

$$T_{SS} = \frac{R_T V^2 / R_0}{1 + \alpha_R R_T V^2 / R_0} \quad (2-13)$$

Thus, a resistor with a positive temperature coefficient of resistor will have a negative feedback that maintains and regulates the resistor so that it will not burn out. If our resistor has a negative temperature coefficient of resistor, we must use a current source to prevent burn out. In our case, single crystal silicon is a material of positive  $TCR$ , thus we use the current source to prevent damage.

### 2.2.2.2 Hear Conduction, Convection, and Thermal radiation consideration

Before modeling a thermal system in detail, three modes of energy (conduction, convection and radiation) must be considered. We must determine which are pertinent. From an energy balance, the thermal energy conservation (2-15) can be understood by comparison with the first law of thermodynamics (2-14). Equation (2-15) is a lumped capacitance model, which assumes the temperature gradient within the solid is negligible. This condition is valid for a Biot number smaller than 0.1. The definition of a Biot Number is the ratio of thermal resistance of conduction over thermal resistance over convection as shown in equation (2-16). For our case, the Biot Number is  $7.9 \times 10^{-6}$  in (2-17), which shows the use of (2-15) is reasonable.

$$\dot{E}_{STORED} = \dot{E}_{IN} - \dot{E}_{OUT} \quad (2-14)$$

$$\rho \cdot V \cdot \tilde{C} \cdot \frac{dT}{dt} = -\varepsilon \cdot \sigma \cdot A_s \cdot (T^4 - T_0^4) - k \frac{A_c}{L} (T - T_0) - hA_s (T - T_0) \quad (2-15)$$

$$Bi = \frac{R_{conduction}}{R_{convection}} = \frac{L/kA}{l/hA} = \frac{hL_c}{k} \quad (2-16)$$

$$Bi = \frac{hL}{k} = \frac{5[W/m^2K] \times 7.9 \times 10^{-6}[m]}{157[W/mK]} = 7.9 \times 10^{-6} \lll 0.1 \quad (2-17)$$

It is important to determine which of the three terms in equation (2-15) will be important. First, consider these modes of transport with respect to a long thin beam. We pick a dimension close to the size of the electrothermal actuators used in Micro-Hexflex. The thin beam is 250 microns long, and a four micron by eight micron cross section. The beam properties are listed in Table 2-9.

Table 2-9 Property values of single crystal silicon					
$\rho$ [kg/m <sup>3</sup> ]	$\tilde{C}$ [J/Kg-K]	$\varepsilon$	$\sigma$ [W/m <sup>2</sup> K <sup>4</sup> ]	$k$ [W/mK]	$h$ [W/m <sup>2</sup> K]
2330	704	0.9	5.67E-8	157	<5

The heat convection coefficient can vary depending on the environmental conditions. As the Micro-Hexflex will be used in a hermetically sealed environment for optical alignment, it is reasonable to assume the system is under an internal natural convection condition, and all the effects are caused by the gravitational and buoyancy force. From the literature, neutral convection coefficients for gases have a range from 0.05 to 50 W/m<sup>2</sup>K [19], and for the micro-scale case it should be much smaller (<<0.1 W/m<sup>2</sup>K) because of the correspondent small Rayleigh number. Now, we compare conduction, radiation, and convection numerically. Let each of them equal to constants  $P$ ,  $Q$ , and  $R$ . The variable  $T_0$  in each equation is set as room temperature at 300 °K. For a reasonable Micro-Hexflex use, the results are listed in ratio in Table 2-10.

$$P = k \frac{A_c}{L} (T - T_0) \quad (2-18)$$

$$Q = \varepsilon \cdot \sigma \cdot A_s \cdot (T^4 - T_0^4) \quad (2-19)$$

$$R = hA_s(T - T_0) \quad (2-20)$$

<b>Table 2-10 Conduction, convection, and radiation comparison</b>			
<b>Temperature (K)</b>	<b>350</b>	<b>500</b>	<b>900</b>
<b><math>Q/P</math></b>	0.41%	0.42%	1.48%
<b><math>R/P</math></b>	<0.15%	<0.15%	<0.15%

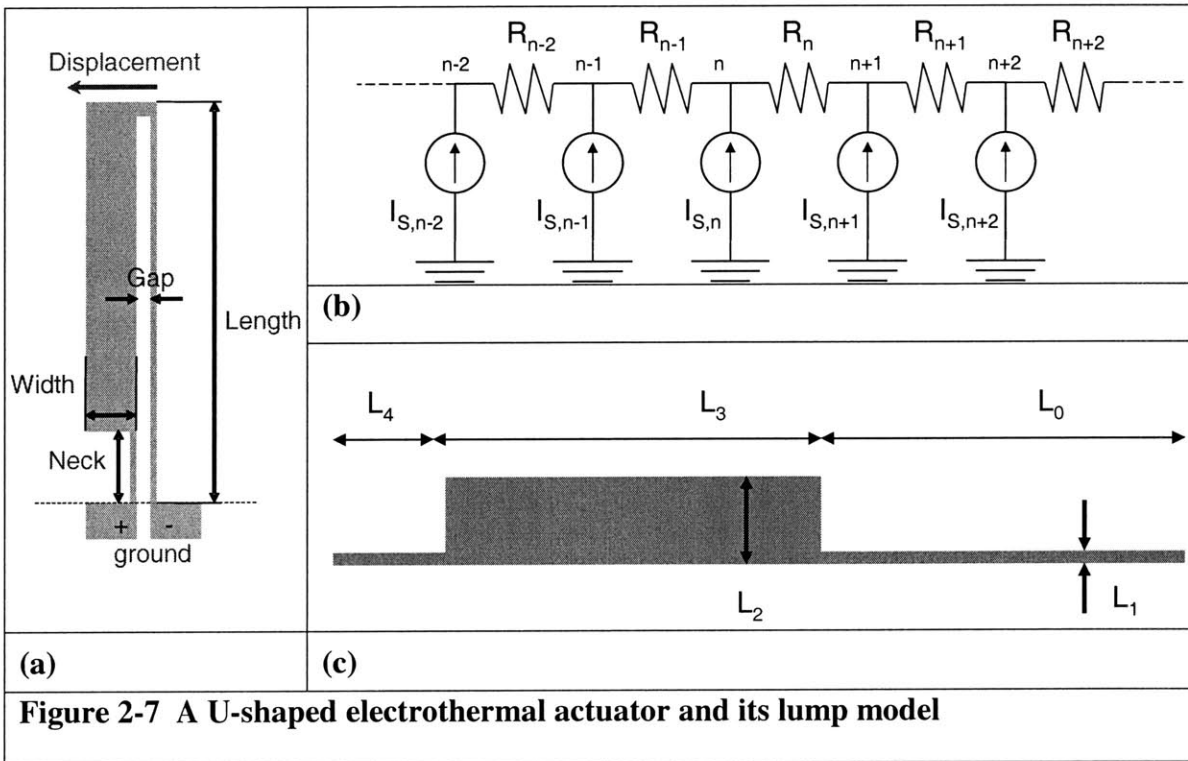
From the table above, it is clear that for a micro-electrothermal actuator, conduction is the dominant energy transport method.

### 2.2.2.3 Finite Difference Temperature Static Solution

Here we assume the thermal actuator has a uniform thickness. According to the standard resistor formula:

$$R = \frac{\rho l}{A} \quad (2-21)$$

The resistance is proportional to the length,  $l$ , and inverse proportional to its cross section area,  $A$ . Since the length of the thin beam and thick beam are equal, when the current runs through the thick beam section, it encounters a resistance at the ratio of  $L_1/L_2$ , which is smaller than the resistance of the thin beam section per unit length. Thus, the thin beam experiences much larger Joule heating.



**Figure 2-7 A U-shaped electrothermal actuator and its lump model**

We will now use a finite difference method to obtain a steady state solution of a simplified model of the thermal actuator. This model captures thermal conduction. The boundary condition assumed here is a constant temperature Dirichlet condition. Beginning from the heat flow equation in the fundamental heat transfer:



$$\frac{\partial}{\partial x} k \frac{\partial T}{\partial x} + \frac{\partial}{\partial y} k \frac{\partial T}{\partial y} + \frac{\partial}{\partial z} k \frac{\partial T}{\partial z} + \dot{q} = 0 \quad (2-22)$$

We assume the thermal conductivity is a constant, therefore,

$$\frac{\partial^2 T}{\partial x^2} + \frac{\partial^2 T}{\partial y^2} + \frac{\partial^2 T}{\partial z^2} = \nabla^2 T = -\frac{\dot{q}}{k} \quad (2-23)$$

which is the Poisson equation. The operator here can be reduced to  $d^2/dx^2$ , which can be approximated by the finite difference expression

$$\left. \frac{\partial^2 T}{\partial x^2} \right|_{x_n} \approx \frac{T(x_n + h) + T(x_n - h) - 2T(x_n)}{h^2} \quad (2-24)$$

Thus, the heat equation can be expressed as

$$\frac{T(x_n + h) + T(x_n - h) - 2T(x_n)}{h^2} = -\frac{\dot{q}}{k} \quad (2-25)$$

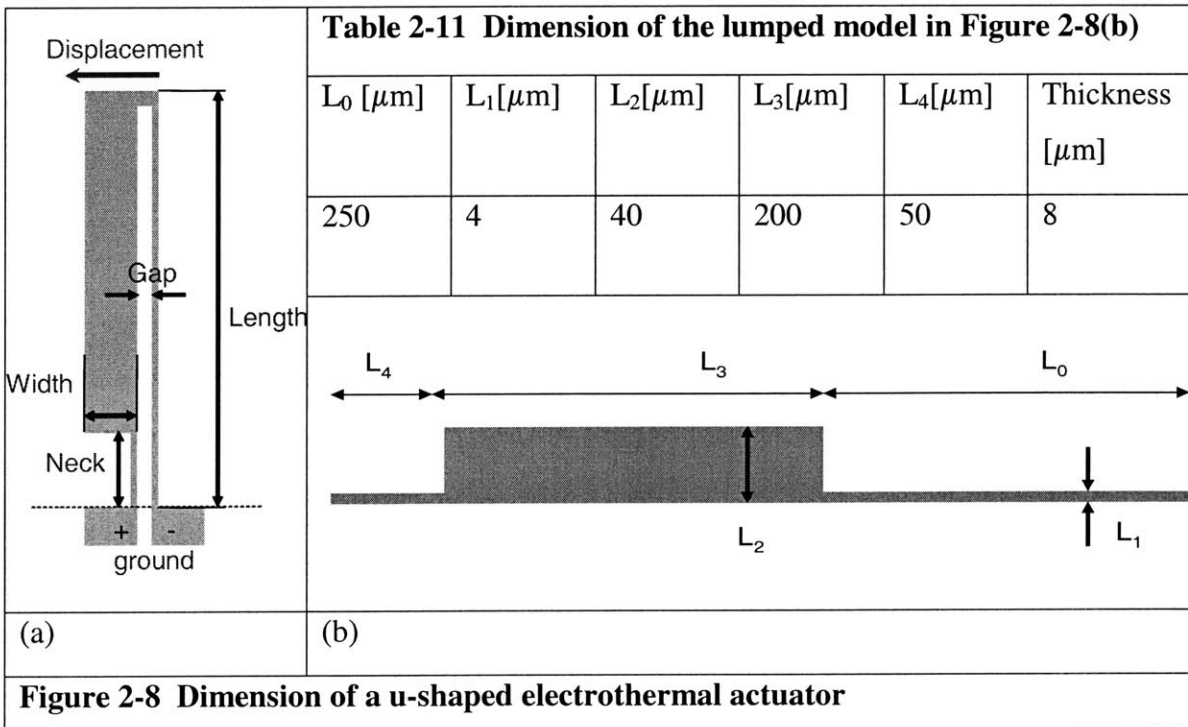
If we let the thermal resistance,  $R_m$ , be  $1/kh$ , then the equation becomes

$$\frac{T_{n+1} - T_n}{R_m} + \frac{T_{n-1} - T_n}{R_{l(n-1)}} = -h^3 \dot{q}(x_n) = I_{S,n} \quad (2-26)$$

The thermal actuator in Figure 2-7 (a) can be simplified to a one dimensional finite difference numerical model. We divide the resistor up meshing into  $N$  equal volume elements as a node in the network as shown in Figure 2-7 (b).  $I_{S,n}$  is defined as the power per unit volume and  $R_m$  is the thermal resistance with the units  $W/m$ . The recursive Poisson Equation can be represented and solved in a matrix form:

$$\begin{bmatrix}
 1 & 0 & 0 & \dots & 0 \\
 \frac{1}{R_0} & \frac{1}{R_0} + \frac{1}{R_1} & \frac{1}{R_1} & \dots & 0 \\
 0 & \frac{1}{R_1} & \frac{1}{R_1} + \frac{1}{R_2} & \dots & 0 \\
 \vdots & \vdots & \vdots & \ddots & \vdots \\
 0 & \dots & \frac{1}{R_{(n-2)}} + \frac{1}{R_{(n-1)}} & \frac{1}{R_{(n-1)}} & 0 \\
 0 & \dots & \frac{1}{R_{(n-1)}} & \frac{1}{R_{(n-1)}} + \frac{1}{R_n} & \frac{1}{R_n} \\
 0 & \dots & 0 & \frac{1}{R_n} & \frac{1}{R_n} + \frac{1}{R_{(n+1)}} \\
 \vdots & \vdots & \vdots & \vdots & \vdots \\
 0 & \dots & \dots & \dots & \frac{1}{R_{(N-2)}} + \frac{1}{R_{(N-1)}} & \frac{1}{R_{(N-1)}} \\
 0 & \dots & \dots & \dots & \frac{1}{R_{(N-1)}} & \frac{1}{R_{(N-1)}} + \frac{1}{R_N} \\
 0 & \dots & \dots & \dots & \frac{1}{R_{(N-1)}} & \frac{1}{R_{(N-1)}} + \frac{1}{R_N} \\
 0 & \dots & \dots & \dots & 0 & \frac{1}{R_N} \\
 0 & \dots & \dots & \dots & 0 & 1
 \end{bmatrix}
 \begin{pmatrix}
 T_0 \\
 T_1 \\
 T_2 \\
 \vdots \\
 T_{n-1} \\
 T_n \\
 T_{n+1} \\
 \vdots \\
 T_{N-1} \\
 T_N \\
 T_{N+1}
 \end{pmatrix}
 =
 \begin{pmatrix}
 0 \\
 I_1 \\
 I_2 \\
 \vdots \\
 I_{n-1} \\
 I_n \\
 I_{n+1} \\
 \vdots \\
 I_{N-1} \\
 I_N \\
 0
 \end{pmatrix}
 \quad (2-27)$$

To develop an idea of how the model works, we first analyze a model with the dimension listed in Table 2-11. The electrothermal actuator, shown in Figure 2-8 (a), is modeled as a straightened structure in Figure 2-8 (b).

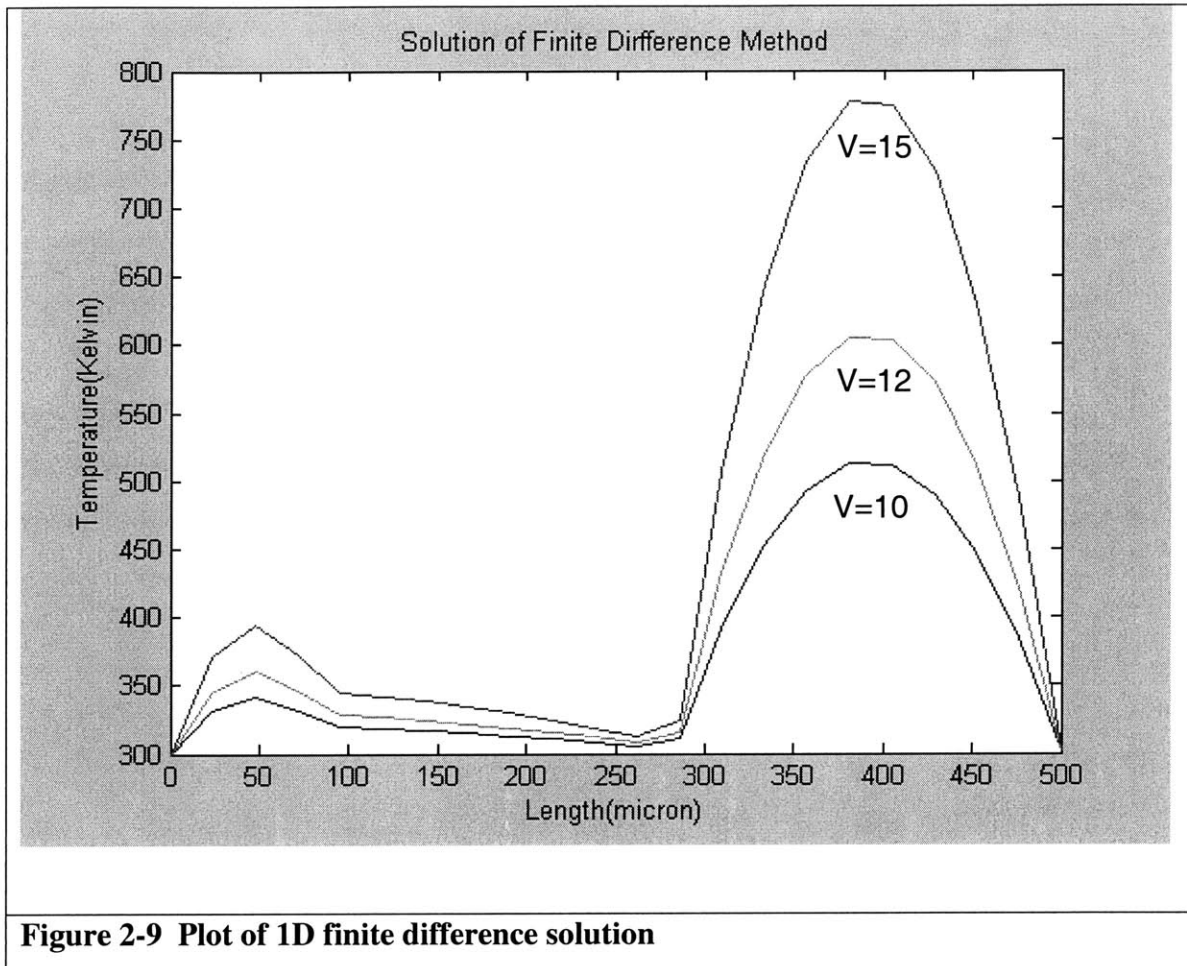


In Table 2-12, electrical resistances for each section are listed along with the voltage and current.

<b>Table 2-12 Properties of test parameters</b>					
Resistivity ( $\rho$ ) [Ohm-cm]	$R_{L0} = \rho l / wt$ [Ohm]	$R_{L3} = \rho l / wt$ [Ohm]	$R_{L4} = \rho l / wt$ [Ohm]	Voltage [Volts]	Current [Amps]
0.02	1562	125	312	10	0.005

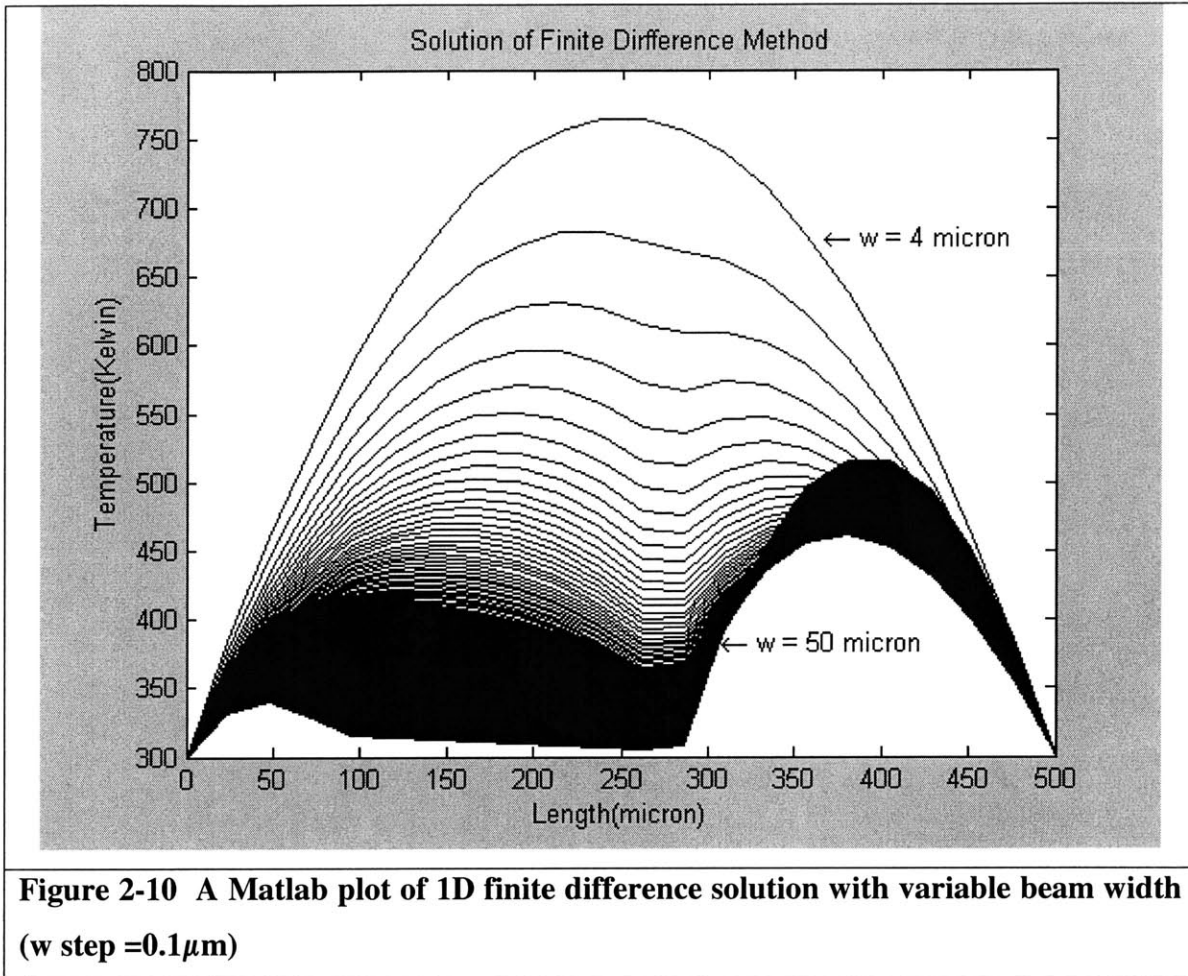
The beam is divided into  $N$  elements with a length  $L/N$ . For  $N=20$ , each unit equals  $L/N = 500/20 = 25 \mu\text{m}$ . Important calculated thermal parameters are presented in Table 2-13 for reference.

<b>Table 2-13 Thermal properties of test parameters</b>						
K[W/mK]	$R_{t0}$ [K/W]	$R_{t3}$ [K/W]	$R_{t4}$ [K/W]	$I_{S,0}$ [W]	$I_{S,3}$ [W]	$I_{S,4}$ [W]
148	$5.28 \times 10^4$	$4.22 \times 10^3$	$1.06 \times 10^4$	0.0391	0.0031	0.0078



**Figure 2-9 Plot of 1D finite difference solution**

The result of the one dimensional finite element analysis for the three voltages (10V, 12V, 15V) is presented in Figure 2-9. The temperature difference between the hot beam and the cold beam is large. In the end, this leads to a large displacement. It is also easy to conceive the relationship between the temperature distribution on the thermal actuator and the different geometries by changing the width,  $L_3$ , of the wide beam. In Figure 2-10, different widths, from  $w = 2 \mu\text{m}$  to  $40 \mu\text{m}$ , are presented. The width of the beam in each solution in Figure 2-10 is increased by a 0.1 micron per step. When the width of the thin beam,  $w$ , equals four microns, the temperature distribution converges to a parabola. From the result here, we get a good sense of how to design the geometry of the thermal actuator. Several different effects and different analysis methods will be taken into account in the later sections.

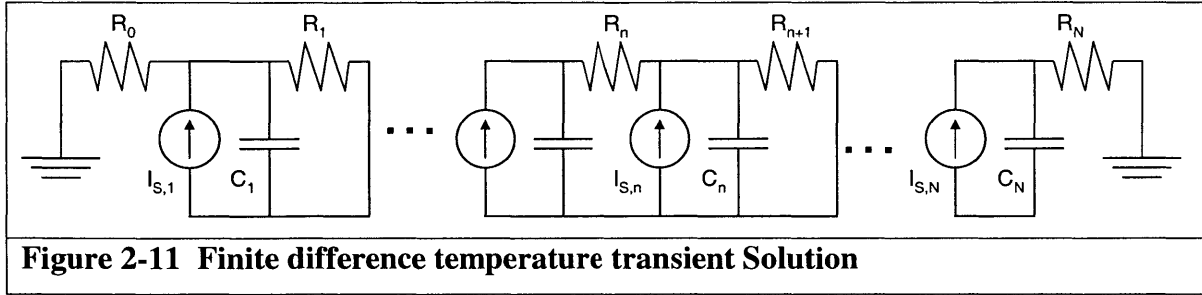


#### 2.2.2.4 Finite Difference Temperature Transient Solution

In the previous section, a model for determining the temperature distribution is established. The next important issue is to determine how fast the thermal actuator can be cycled. This is important because it tells us the fundamental speed limit of using an electrothermal actuator. According to the results from section 2.2.2.2, only thermal conduction is considered in this section. In section 2.2.2.6, we will build a finite element model, which takes convection and radiation into account to verify the correctness of this finite difference model.

To consider the transient response of a thermal system, capacitances are added into the original thermal model. Each finite element still has its own corresponding capacitance as

shown in Figure 2-11.



The transient thermal model uses the electrothermal actuator of same dimension as in Table 2-11 with a 10 Volts driving voltage in Table 2-12 and Table 2-13. The thermal capacitance of the single crystal silicon made thermal actuator is

$$C = \rho \cdot A \cdot L \cdot \tilde{C}$$

where  $\rho$  is the mass density,  $A$  is the cross-section area, and  $L$  is the length for the beam.

The results of the calculated capacitances of each section are shown in Table 2-14.

<b>Table 2-14 Capacitance of test parameters</b>				
Resistivity ( $\rho$ ) [Ohm-cm]	$\tilde{C}$ [J/Kg-K]	$C_{L0} = \rho A L_0 \tilde{C}$ [J/K]	$C_{L3} = \rho A L_3 \tilde{C}$ [J/K]	$C_{L4} = \rho A L_4 \tilde{C}$ [J/K]
0.02	712	$1.32 \times 10^{-8}$	$1.06 \times 10^{-7}$	$2.65 \times 10^{-9}$

In equation (2-28), the transient component “ $\tilde{C} dT/dt$ ” is added into the one dimensional static thermal equation. In equation (2-29) to (2-31), a mathematical model for solving one dimensional transient case is derived.

$$\tilde{C} \frac{\partial T}{\partial t} - K \frac{\partial^2 T}{\partial x^2} = \tilde{I} \tag{2-28}$$

$$\frac{\partial T}{\partial t} - D \frac{\partial^2 T}{\partial x^2} = \frac{\tilde{I}}{\tilde{C}}$$



$$BI = u = \begin{pmatrix} 0 \\ I_1/C_1 \\ I_2/C_2 \\ \vdots \\ I_{n-1}/C_{n-1} \\ I_n/C_n \\ I_{n+1}/C_{n+1} \\ \vdots \\ I_{N-1}/C_{N-1} \\ I_N/C_N \\ 0 \end{pmatrix}$$

$$\frac{T_{n+1} - T_n}{\Delta t} = AT_n + u$$

$$T_{n+1} = T_n + AT_n \Delta t + u \Delta t$$

$$T_{n+1} = (I + A \Delta t) T_n + u \Delta t$$

$$T_1 = (I + A \Delta t) T_0 + u \Delta t$$

$$T_2 = (I + A \Delta t) T_1 + u \Delta t$$

$$T_2 = [(I + A \Delta t) T_0 + u \Delta t] (I + A \Delta t) + u \Delta t$$

$$T_2 = (I + A \Delta t)^2 T_0 + u \Delta t (I + A \Delta t) + u \Delta t$$

⋮

$$T_n = (I + A \Delta t)^n T_0 + u \Delta t (I + A \Delta t)^{n-1} + \dots + u \Delta t (I + A \Delta t) + u \Delta t$$

$$T_n = (I + A \Delta t)^n T_0 + [I - (I + A \Delta t)]^{-1} [I - (I + A \Delta t)^n] \cdot u \Delta t$$

(2-31)

The next step is to determine a suitable time step to make sure the solution will converge. For a matrix,  $M = (I + \Delta t C^{-1} A)$  in the (2-31), it is difficult to tell whether this is going to converge or diverge intuitively. However, if the matrix  $M$  is decomposed to its eigenvalue matrix  $\Lambda$  and eigenvector  $\tilde{V}$ :



$$M\bar{V} = \bar{V}\Lambda \Rightarrow M = \bar{V}\Lambda\bar{V}^{-1} = [\bar{v}_1 \bar{v}_2 \cdots \bar{v}_k] \begin{bmatrix} \lambda_1 & & & \\ & \lambda_2 & & \\ & & \ddots & \\ & & & \lambda_k \end{bmatrix} [\bar{v}_1 \bar{v}_2 \cdots \bar{v}_k]^{-1}$$

$$M^N = (\bar{V}\Lambda\bar{V}^{-1})^N = [\bar{v}_1 \bar{v}_2 \cdots \bar{v}_k] \begin{bmatrix} \lambda_1 & & & \\ & \lambda_2 & & \\ & & \ddots & \\ & & & \lambda_k \end{bmatrix}^N [\bar{v}_1 \bar{v}_2 \cdots \bar{v}_k]^{-1}$$

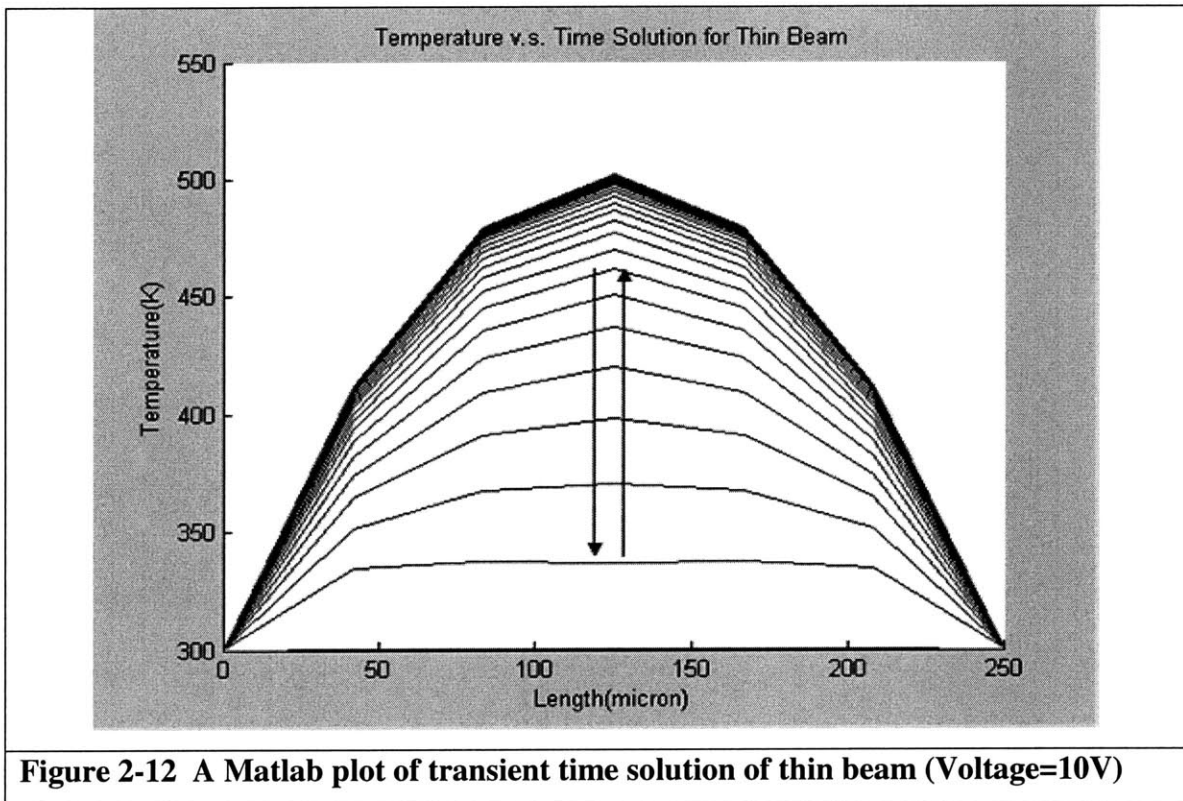
$$M^N = (\bar{V}\Lambda\bar{V}^{-1})^N = [\bar{v}_1 \bar{v}_2 \cdots \bar{v}_k] \begin{bmatrix} \lambda_1^N & & & \\ & \lambda_2^N & & \\ & & \ddots & \\ & & & \lambda_k^N \end{bmatrix} [\bar{v}_1 \bar{v}_2 \cdots \bar{v}_k]^{-1} \quad (2-32)$$

Thus, it is now obvious that if  $|\max(\lambda_i)| \leq 1$ , the  $N$  power matrix will converge. The tightest constraint is therefore produced by the negative eigenvalues whose magnitude is the largest:

$$\Delta t_{\max} < \frac{2}{|\lambda|_{\max}} \quad (2-33)$$

According to the result in Figure 2-10, as long as the width,  $w$ , is close to 40 to 50 micron, the temperature at the end of the thin beam is around 310 °K. On the other end of the thin beam is the boundary temperature, which is set to be 300 °K in the beginning. Since the thin beam section is the only “slow” section that will be heating up and cooling down; and its two ends are almost stays at  $\sim 300$  °K, we can further simplify the analysis to focus on the thin beam section. With only seven nodes ( $N=7$ ), we get a rapid understanding of how fast the system can be operated. The result of this simple model is shown in Figure 2-12. The time step used here is 0.00005 second. Exactly 0.0006 seconds are needed to reach a temperature 480 °K, which is 90% close to its static state solution 500 °K. The cooling process can also be analyzed in a similar way, and the time is found

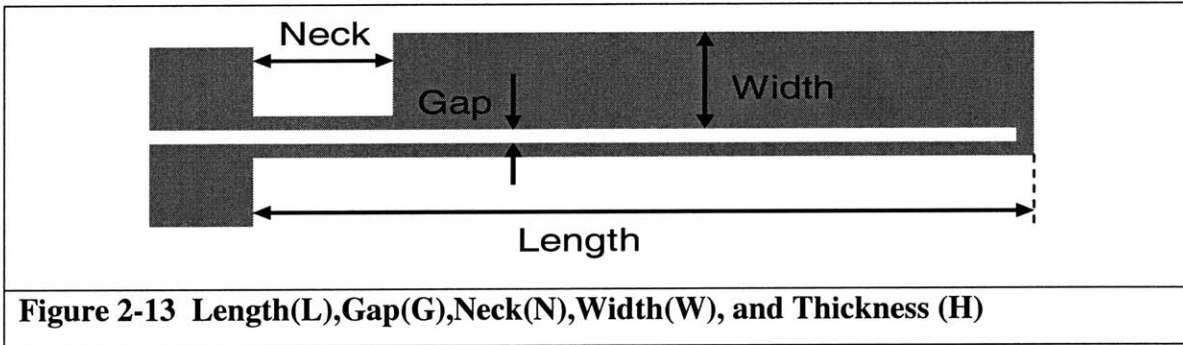
to be within 98% of the same as it takes to heat up. The reason is that a linear partial differential equation and its velocity propagation of information do not depend on the amplitude of the function. As a result, our thermal actuator will have a limit operating frequency around 1KHz. Compared to the first natural frequency of the Micro-Hexflex, which is at 8.273 KHz, we know the thermal operating cycle is the limiting dynamic element. The detail of natural frequency will be presented in section 2.2.2.6.



### 2.2.2.5 Dimensional analysis

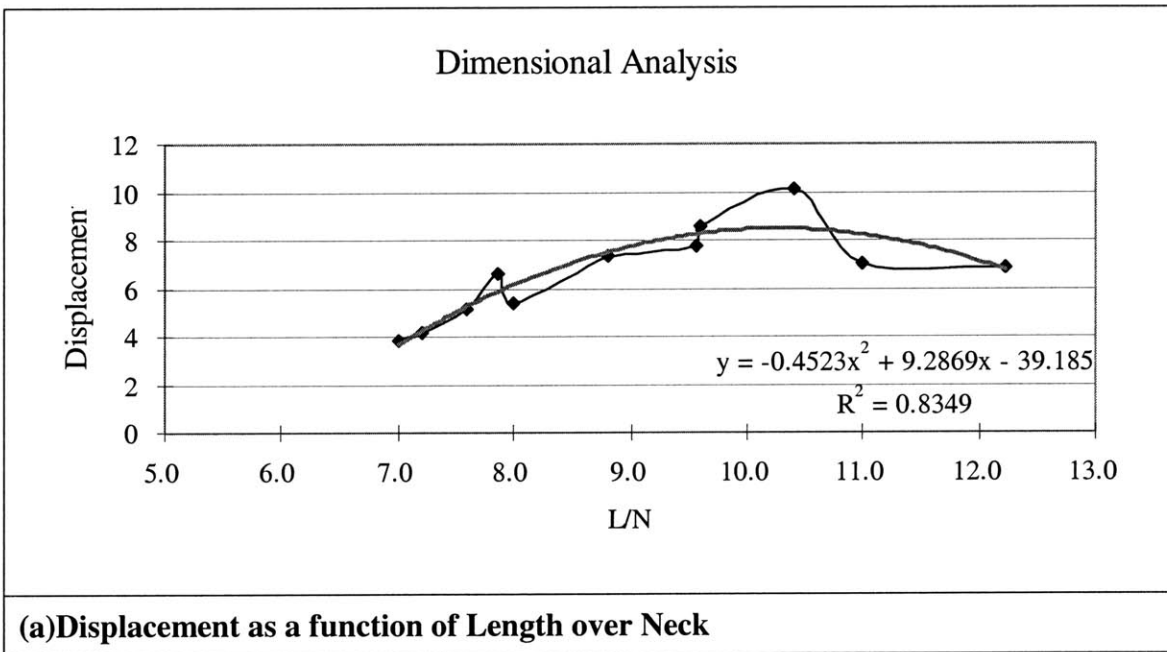
A dimensional analysis of the thermal actuator is used to rapidly optimize the geometry of thermal actuator and examine the incompleteness of the simplification process used during the derivation of finite element analysis. The goal of this dimensional analysis is to optimize the displacement as well as the force output. COSMOS Works<sup>TM</sup> and SOLIDWORKS<sup>TM</sup> are here used as tools to provide an appropriate and fast result to verify how different parameters affect each other. Five dimension parameters in the

thermal actuator have been chosen. Generally, we know that when the length ( $L$ ) is larger, the displacement increases. However, when  $L$  is too large, buckling effects start to happen in the deformation process, and the situation becomes more complicated. Thus, a simple dimensional analysis will be of great value to help to get a good sense to start the optimization before blindly applying any theoretical and numerical analysis to solve the problem.

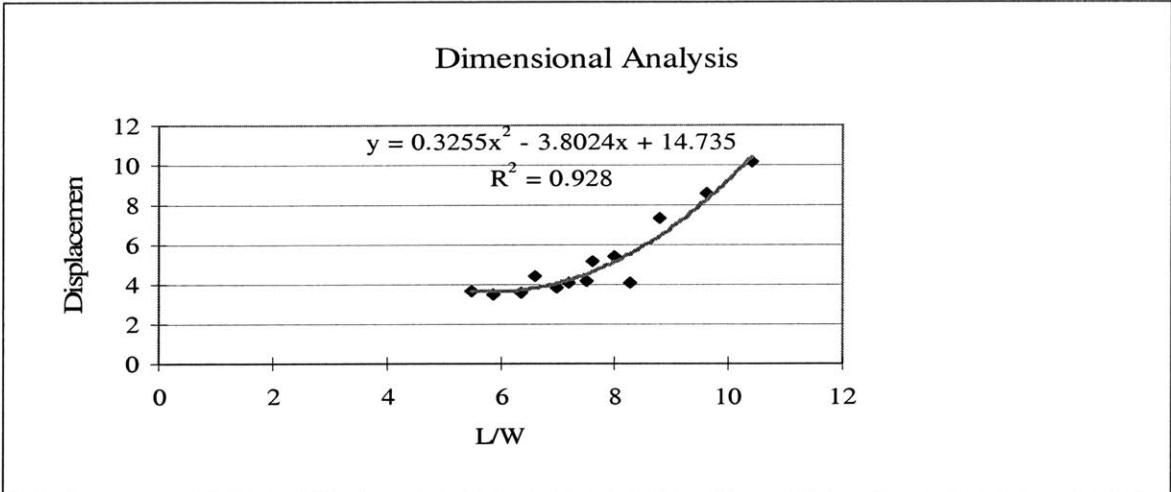


**Figure 2-13 Length( $L$ ),Gap( $G$ ),Neck( $N$ ),Width( $W$ ), and Thickness ( $H$ )**

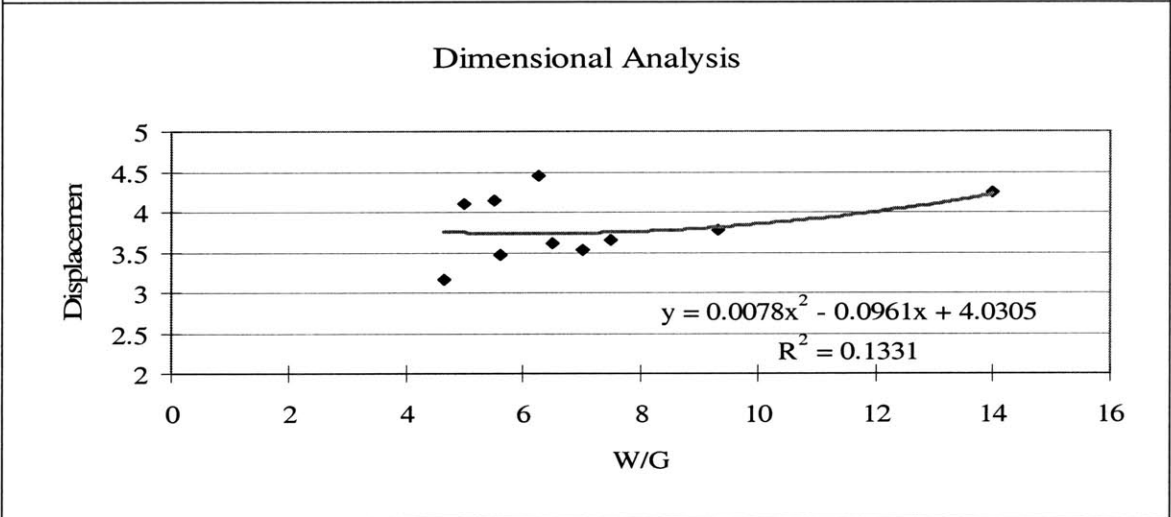
The results in Figure 2-14 are illustrated from (a) to (g).



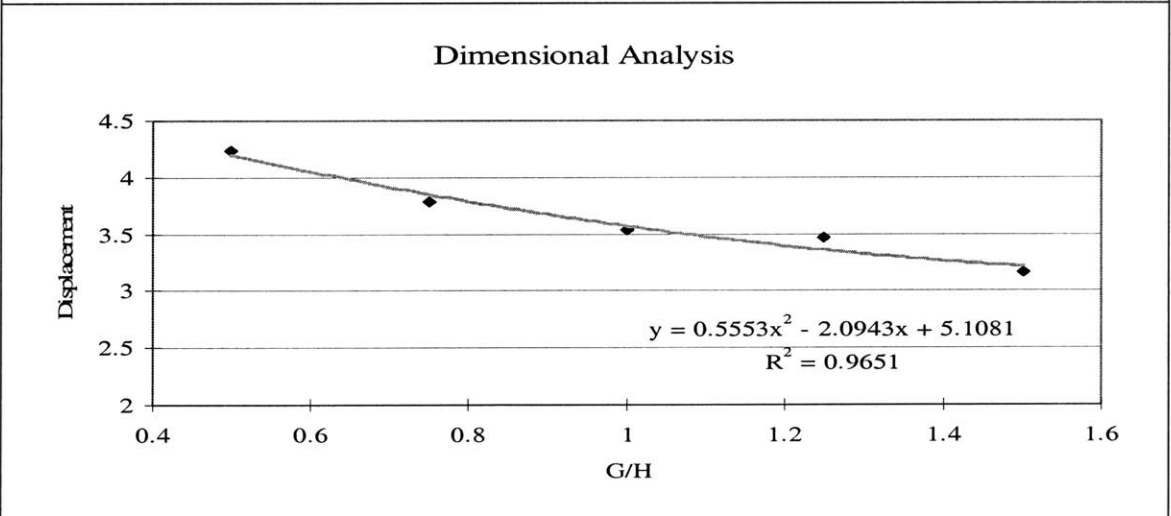
**(a) Displacement as a function of Length over Neck**



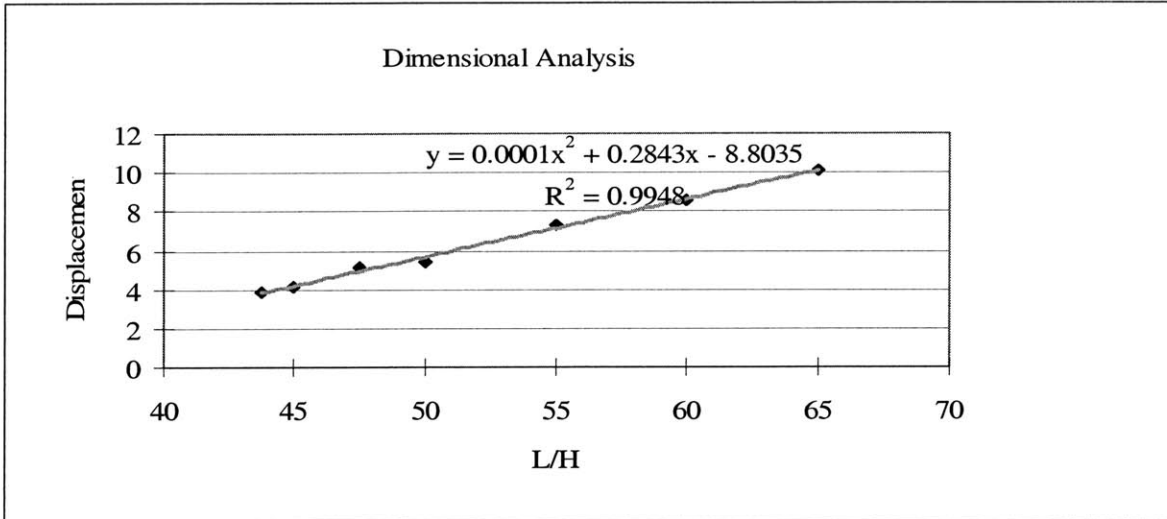
**(b) Displacement as a function of Neck over Width**



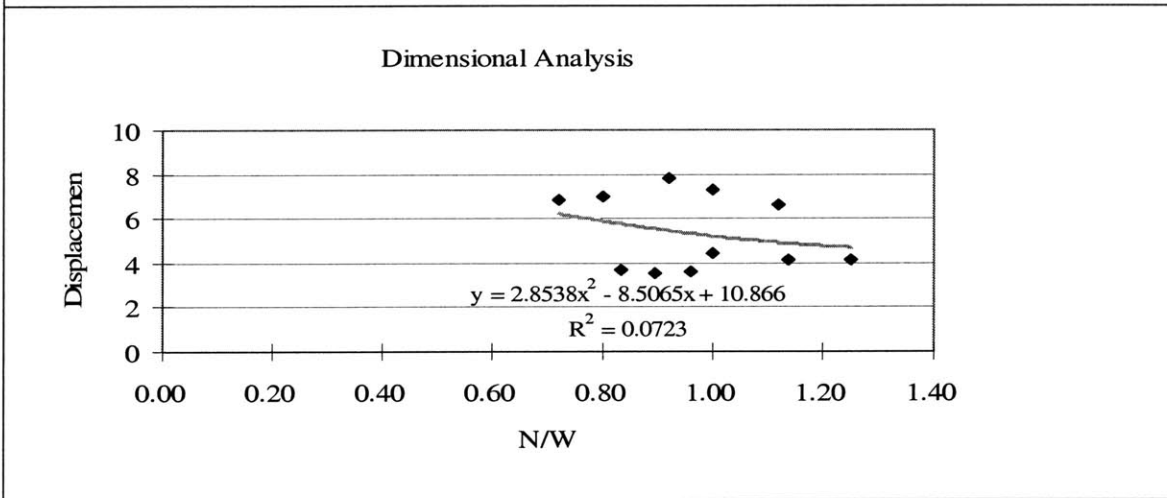
**(c) Displacement as a function of Width over Gap**



**(d) Displacement as a function of Gap over Thickness**



**(e) Displacement as a function of Length over Thickness**



**(f) Displacement as a function of Neck over Width**

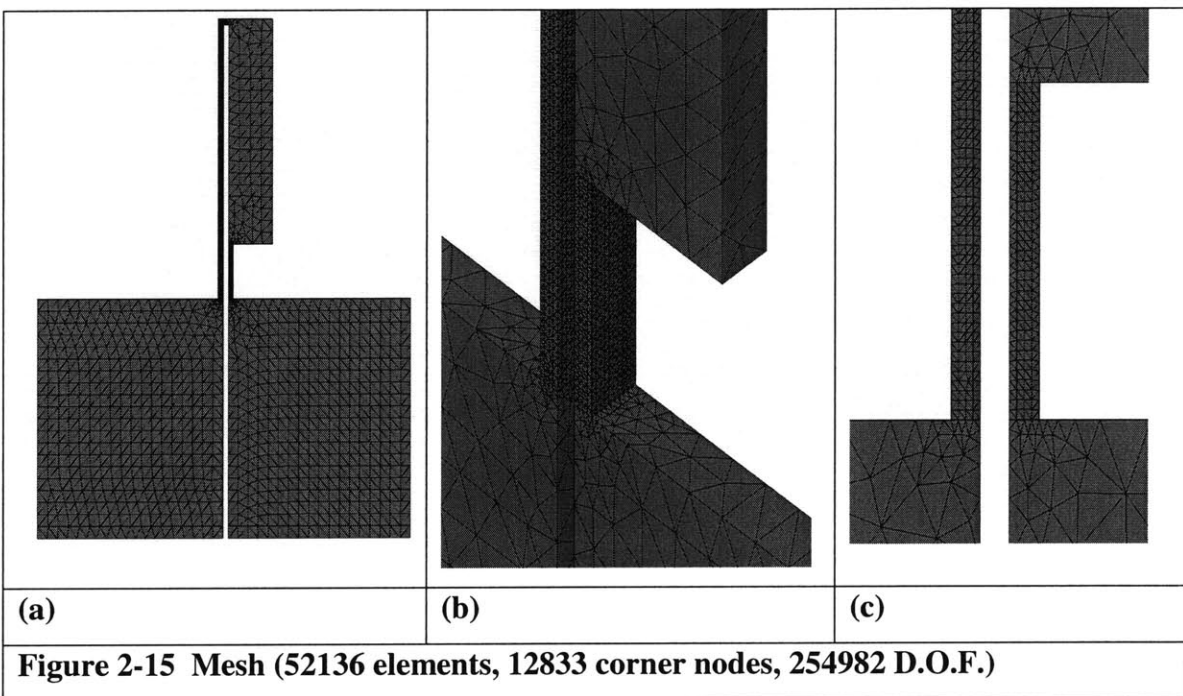
**Figure 2-14 Dimensional analysis from (a) to (g)**

In Figure 2-14 (a), the output displacement is a quadratic parabolic function of the ratio of length ( $L$ ) and neck ( $N$ ), where it is obvious at the ratio 9, the displacement could be optimized. In the example studied in section 2.2.2.3, if the length is without change (250 microns), the neck should be set at 27.8 micron to obtain the largest output displacement at the tip. In Figure 2-14 (b), it is inspected that as the ratio of length ( $L$ ) over width ( $W$ ) increase, the output will be increased together. This result is beneficial to the actuator design because when increasing the ratio of length ( $L$ ) and width ( $W$ ), the thermal resistance difference between two sections will also be increasing and thus result in good temperature distribution difference. In Figure 2-14 (c) and (f), with the low  $R^2$  values

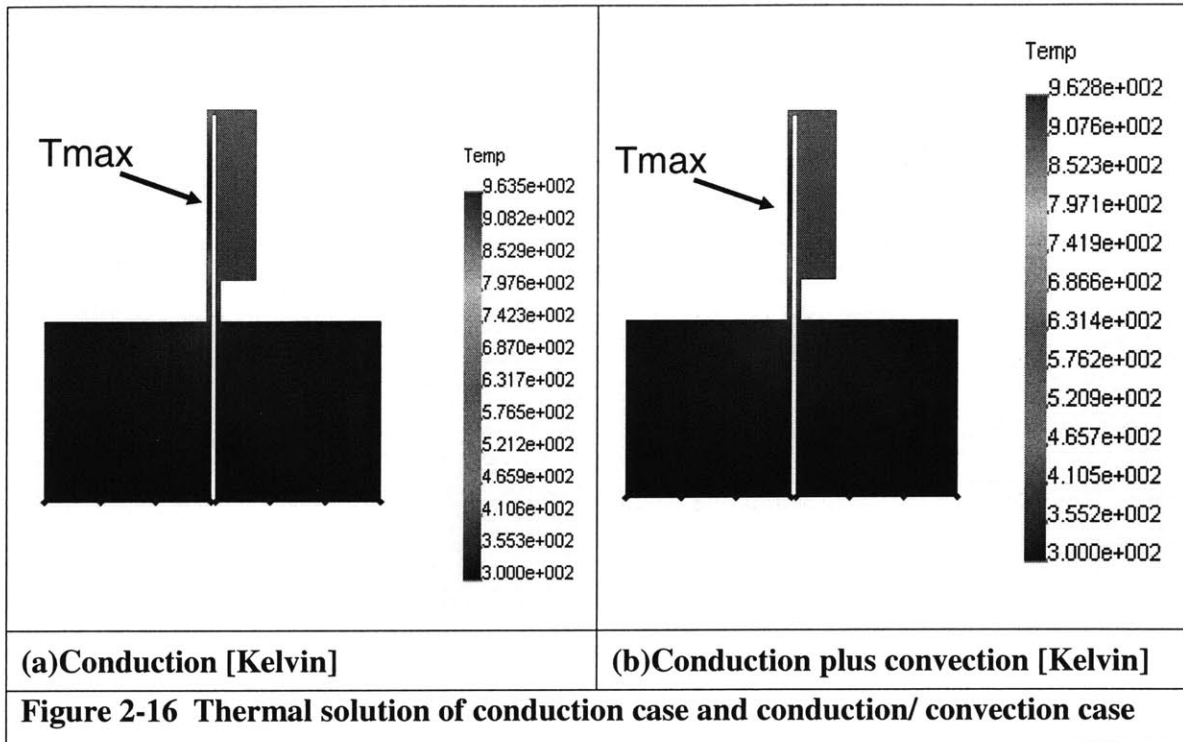
( $\sim 0.1$ ), it is apparent that there is no relationship between the width ( $W$ ) and gap ( $G$ ) or the neck ( $N$ ) and width ( $W$ ). Comparing Figure 2-14 (d) and (e), we notice the thickness ( $H$ ) contributes little to the displacement. This is intuitively clear and it is good to realize it in a sophisticated way. The best information from Figure 2-14 (d) and (e) is that the output displacement is proportional to the length ( $L$ ). From Comtois' experiment and paper [12], we know if the length ( $L$ ) is too long, buckling effect might happen and this will not be found in a linear model, thus this dimensional analysis has its limits.

### 2.2.2.6 Finite element Solution from COSMOS Works

We again here build a test model shown in Figure 2-15. The thermal actuator model has a length 200 micron, width 35 micron, both the gap and thin beam four micron wide, and a thickness of eight microns. Figure 2-15 (b) and (c), shows the mesh components of the neck. We apply control to the mesh at the thinnest section and make sure it at least has four elements crossing the neck to accurately capture bending and shear in this portion of the device.

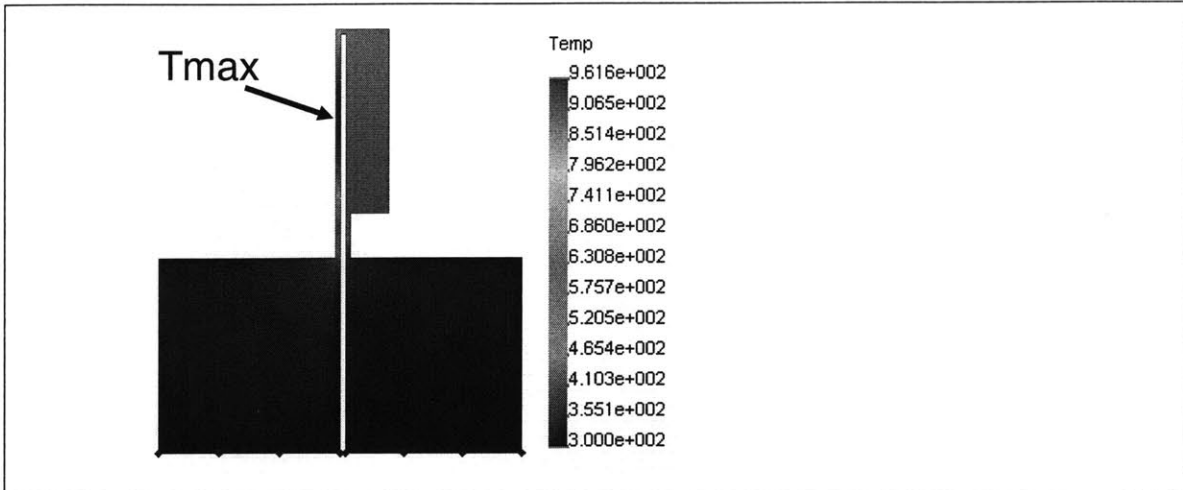


The material properties of this single crystalline silicon thermal actuator are the same as the case study in Section 2.2.2.3. They and are listed in Table 2-12. In this model, the applied voltage is 10 Volts. We calculate the power dissipated in thermal actuator is 0.9 W. These inputs were used with the COSMOS Works thermal solver to obtain results shown in Figure 2-16 and Figure 2-17. In Figure 2-16 (a), only thermal conduction is taken into account, in Figure 2-16 (b) both conduction and convection are counted.



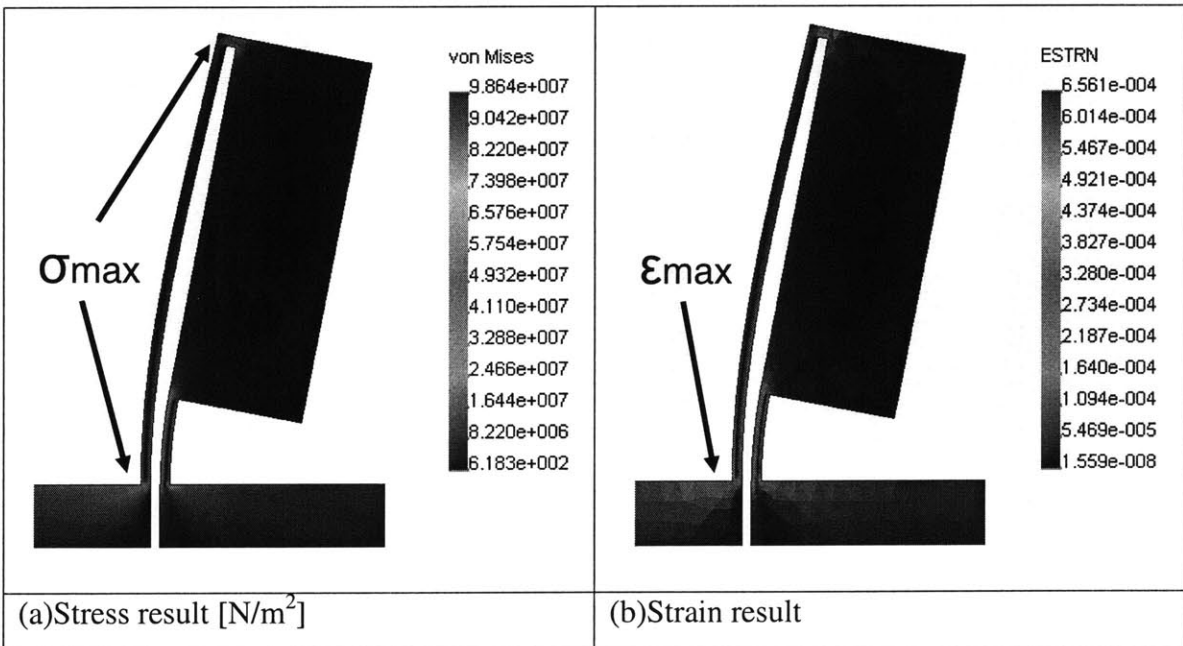
In Figure 2-17, thermal radiation effects are added into the simulation, where the emissivity 0.9 is assumed. We found that the highest temperature in the hot beam of Figure 2-16(a) is 963.5°K, and in (b) is 962.8°K, which only differs by 0.7 °K. The convection effect is about 0.07% compared to the conduction effect. The thermal radiation compared to conduction is about 0.19%. In both case, the results agree with Table 2-10. Thus, in most of the later simulation to enhance the performance of the device, only thermal conduction is taken into account to speed up the simulation.





**Figure 2-17 Thermal solution with conduction, convection, and radiation effects**

We now, substitute the results of thermal solver into the static structure solver in COSMOS Works. It gives the stress and strain distribution in Figure 2-18 (a) and (b). The largest stress here is 98.6 MPa, which is only about 1.5% compared to the failure stress of single crystalline silicon, 7000MPa [20].



(a) Stress result [N/m<sup>2</sup>]

(b) Strain result

**Figure 2-18 Stress and strain results**

Additional results for total displacement and displacement in x-axis direction are illustrated in Figure 2-19 (a) and (b). We can see the largest displacement in x-axis direction for this case is 1.63 microns, and the total displacement is 1.66 microns.

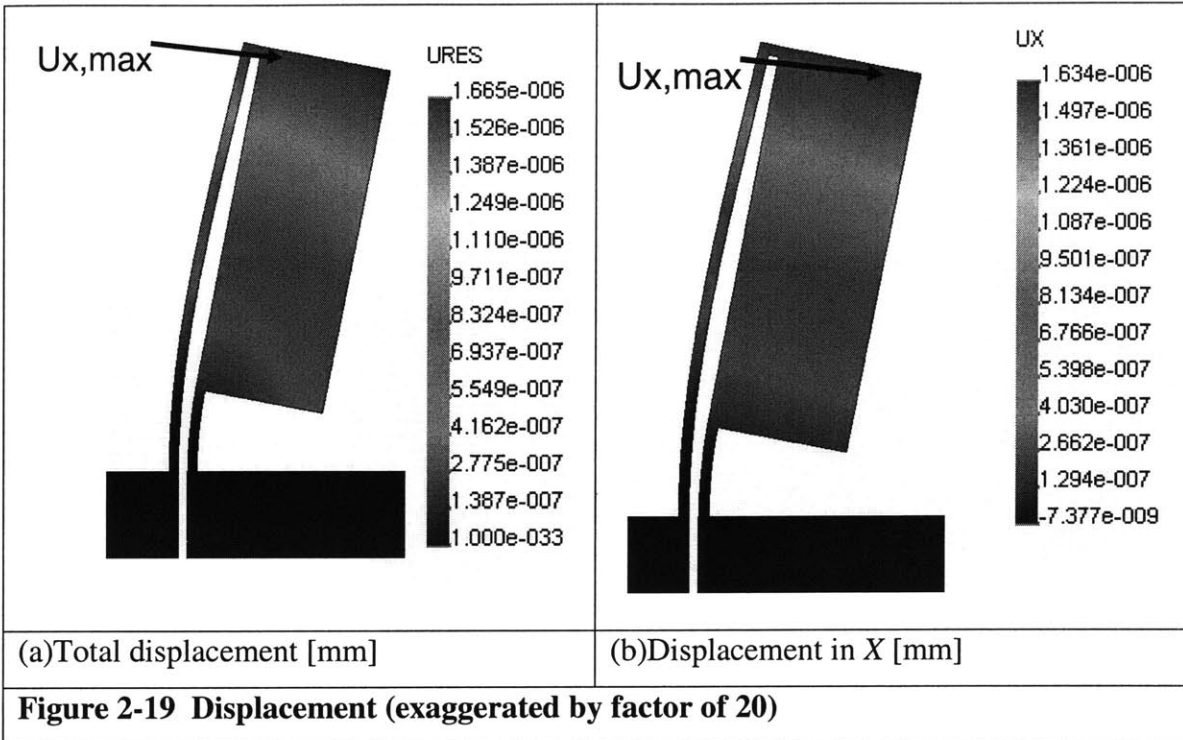
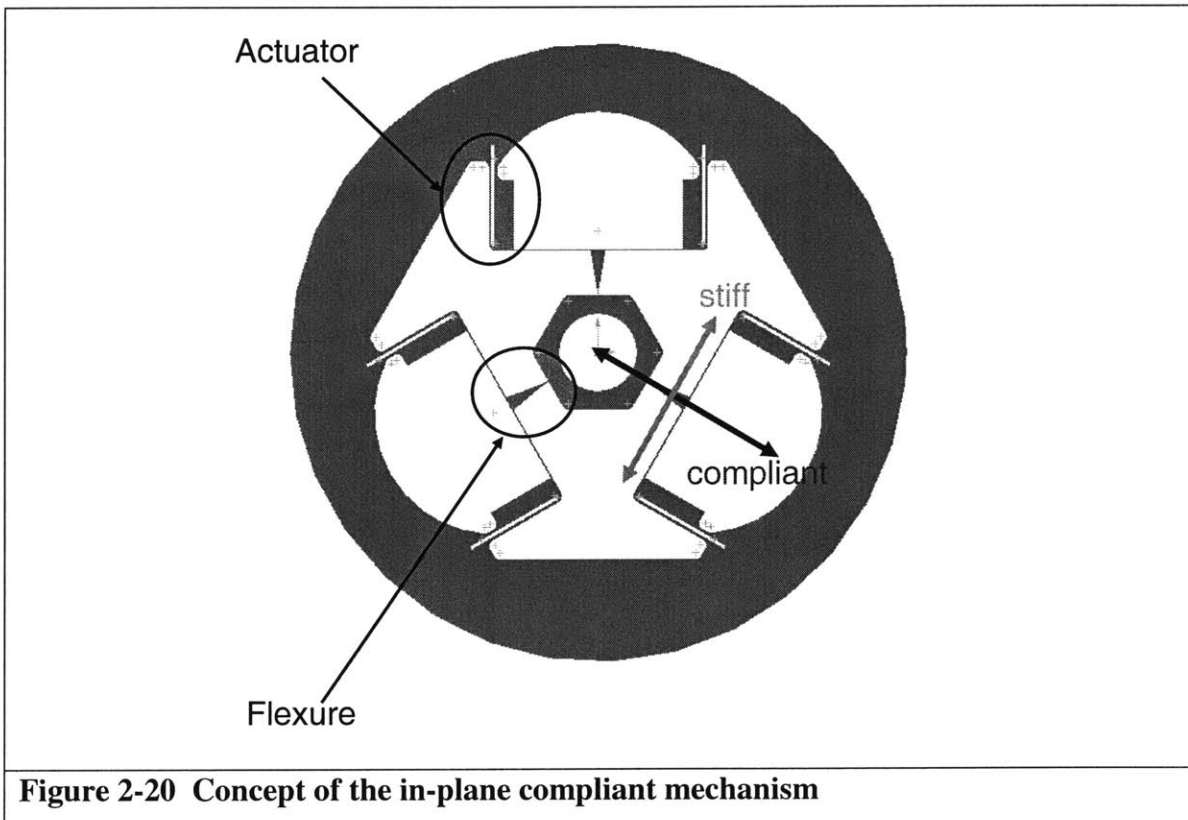


Table 2-15 shows the result of frequency analysis from the frequency solver in COSMOS Works. The first mode occurs at 8 KHz. In section 2.2.2.4, we learn the time for the thermal actuator to heat up and cool down is about 0.001 second (1 KHz). Accordingly, the resonant frequency is not a limiting dynamics issue.

<b>Table 2-15 Frequency analysis</b>		
Mode	Frequency [Hz]	Period [second]
1	8273.4	$1.21 \times 10^{-4}$
2	34355	$2.91 \times 10^{-5}$
3	37955	$2.63 \times 10^{-5}$

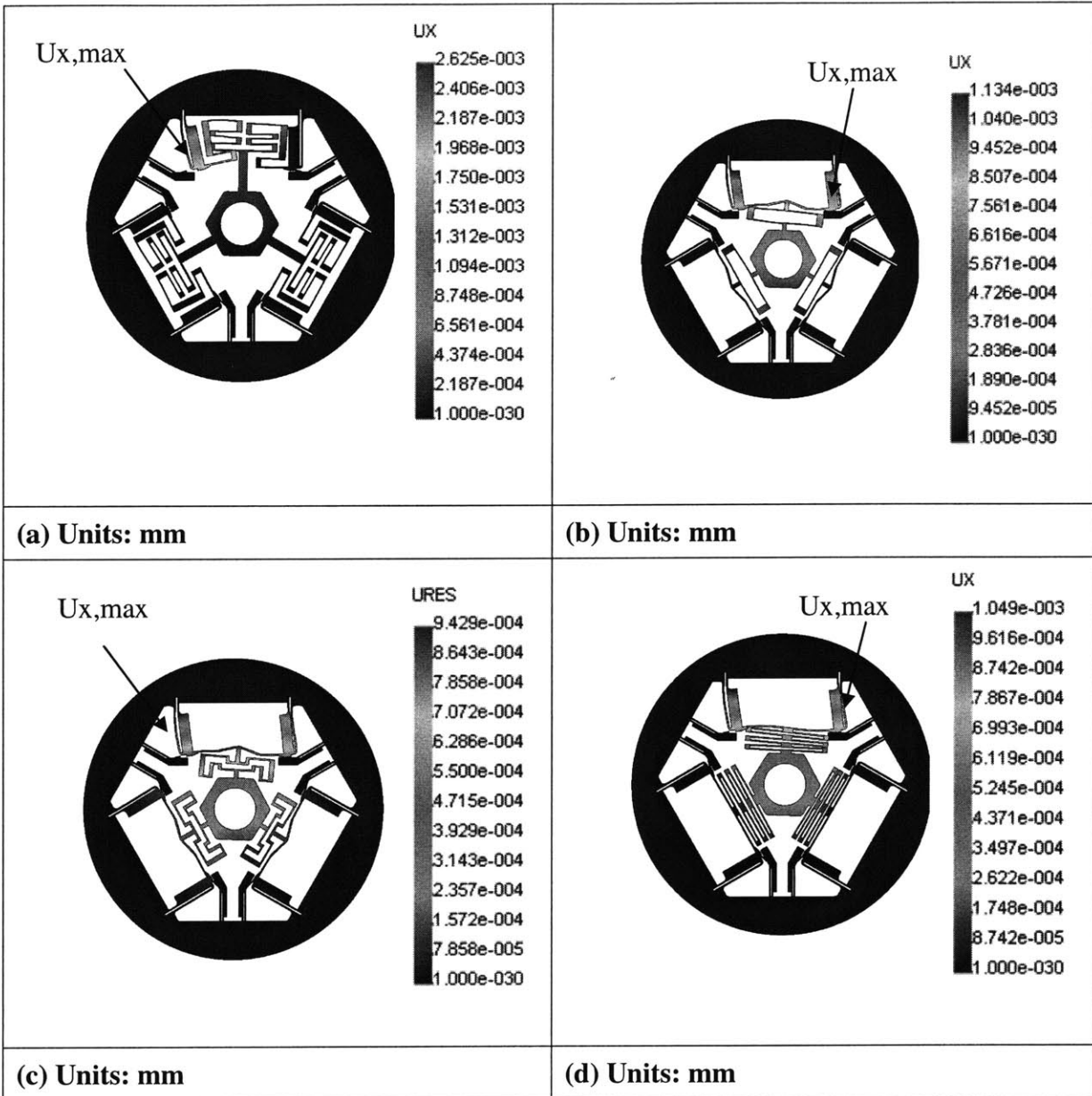
### 2.2.3 In-Plane Compliant Mechanism Design

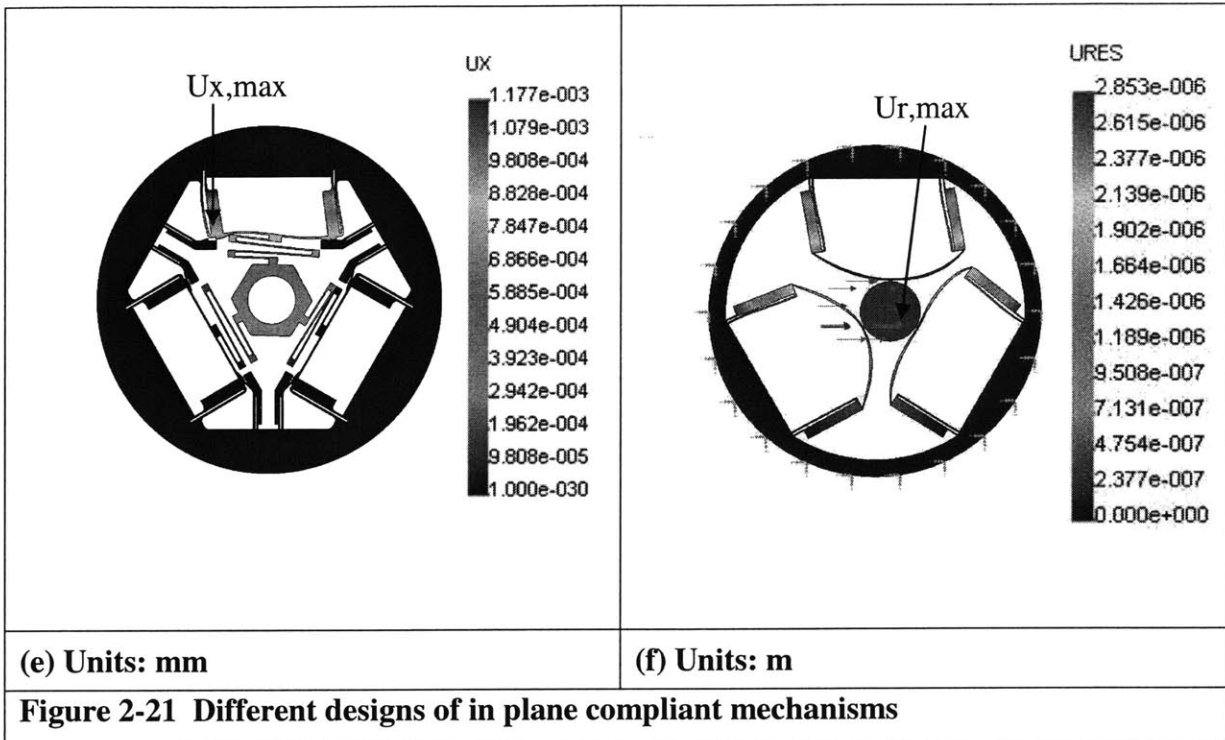
The Micro-Hexflex is a planar compliant mechanism, which uses the optimized electrothermal actuator. As shown in Figure 2-20, portions of the compliant mechanism must be designed stiff in the lateral direction and compliant in the longitudinal direction to ensure proper function. The Micro-Hexflex must be designed stiff along the lateral direction so that the actuator can have a high transmission ratio between the actuator and the stage. The Micro-Hexflex must be compliant in the direction shown to allow useful stage motions.



**Figure 2-20 Concept of the in-plane compliant mechanism**

Different versions of compliant flexure designs have been studied and their transmission ratios are listed in Table 2-16. The transmission ratio is defined as the ratio of the central stag displacement to the displacement of the tip of the thermal actuator. We use the transmission ratio and total displacement as the primary metrics to optimize the compliant mechanism of the Micro-Hexflex.





The evolution sequence of the compliant mechanism designs are shown in Figure 2-21 to obtain the largest working volume out of the limited one millimeter diameter circle. Based on the results in Table 2-16, the bow-shaped compliant mechanism is chosen as the final optimized version.

Type	(a)	(b)	(c)	(d)	(e)	(f)
<b>Maximum Displacement of actuator in X [micron]</b>	2.10	0.87	0.80	0.8	0.92	1.3
<b>Maximum Displacement on the center stage [micron]</b>	0.099	0.470	0.456	0.504	0.589	0.816
<b>Transmission Ratio</b>	4.7%	54%	57%	63%	64%	68%

Figure 2-22 illustrates how actuation combinations are used to obtain various motions.

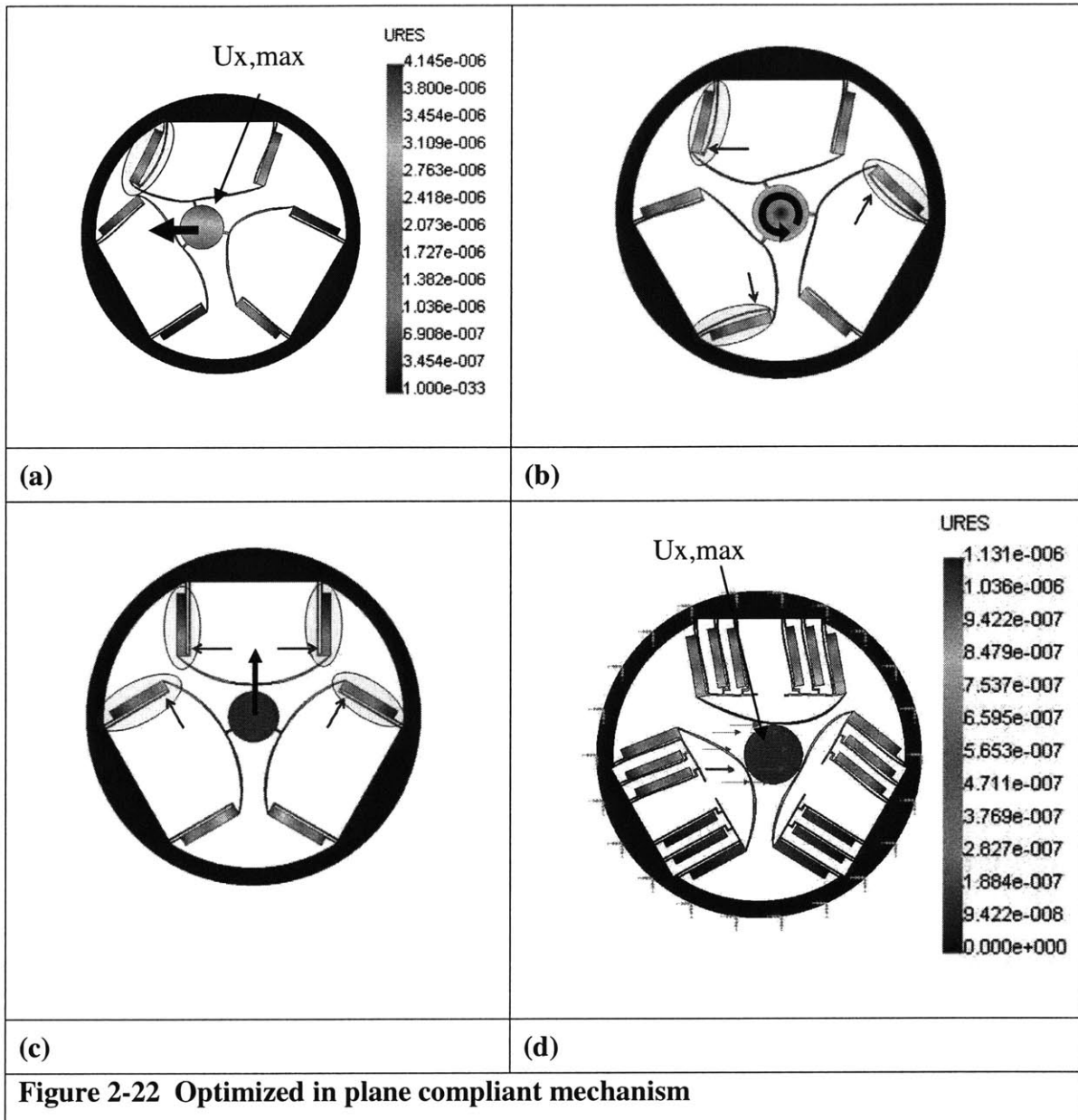


Table 2-17 gives the optimized performance of the Micro-Hexflex from COSMOS Works. The Micro-Hexflex gives a four by four micron in-plane range and a 2.84 degree rotation about z-axis. This satisfies the function requirement for fiber alignment estimated in Section 2.1 Table 2-5.

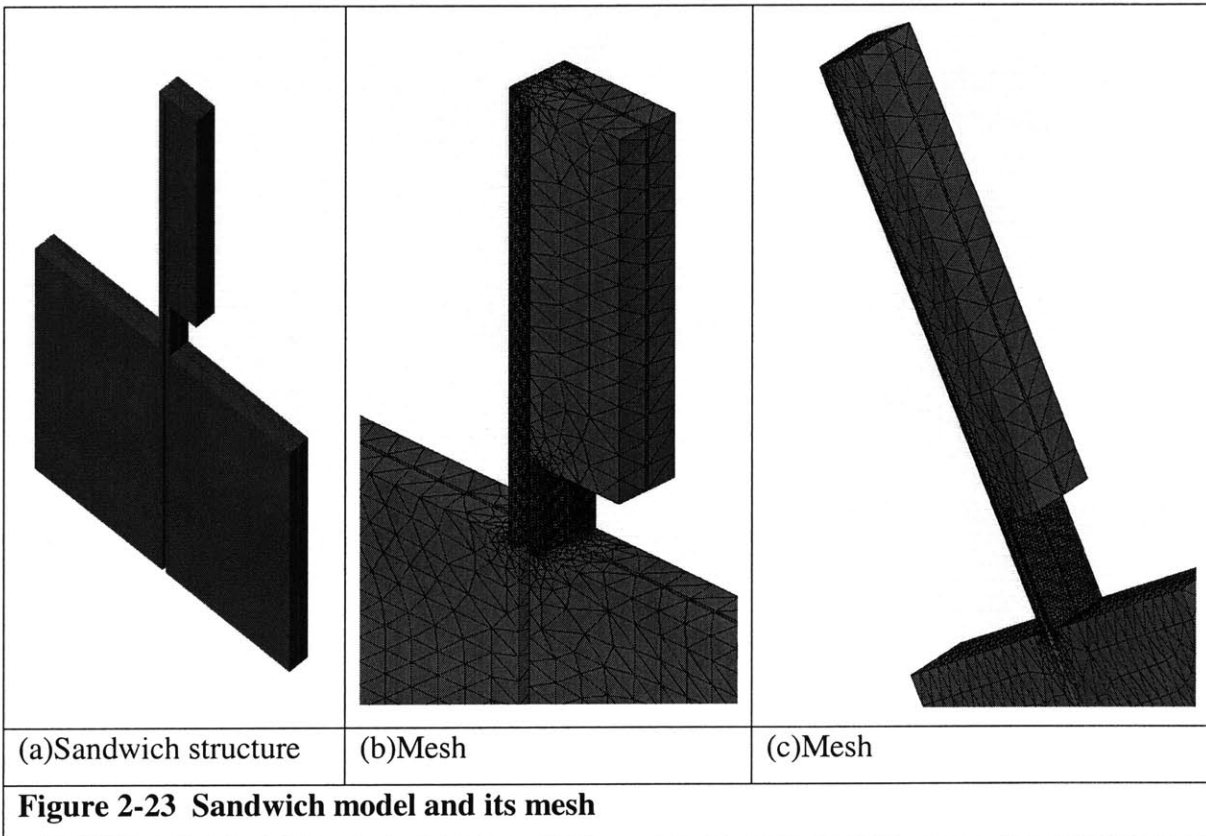
<b>Table 2-17 Micro-Hexflex in plane displacement</b>			
	X(micron)	Y(micron)	$\theta_z$ (degree)
Positive	+2.08	+2.18	+1.42
Negative	-2.08	-2.18	-1.42
Total	4.16	4.36	2.84

In Table 2-18, we have the simulated force and stiffness output for a Micro-Hexflex. The working temperature is set from 300°K to 800°K. From the literature of MIT micro-engine's group [21], the ultimate tensile yield stress for single crystalline silicon will remain unchanged until 900°K. The melting point for single crystalline silicon is at 1400°K. Thus, the maximum operating temperature, 800°K, is quite safe for the device.

<b>Table 2-18 Micro-Hexflex predicted performance</b>			
	Force (micro N)	Stiffness (N/m)	Working Temp (°K)
Single layer	~180	120-150	300-800

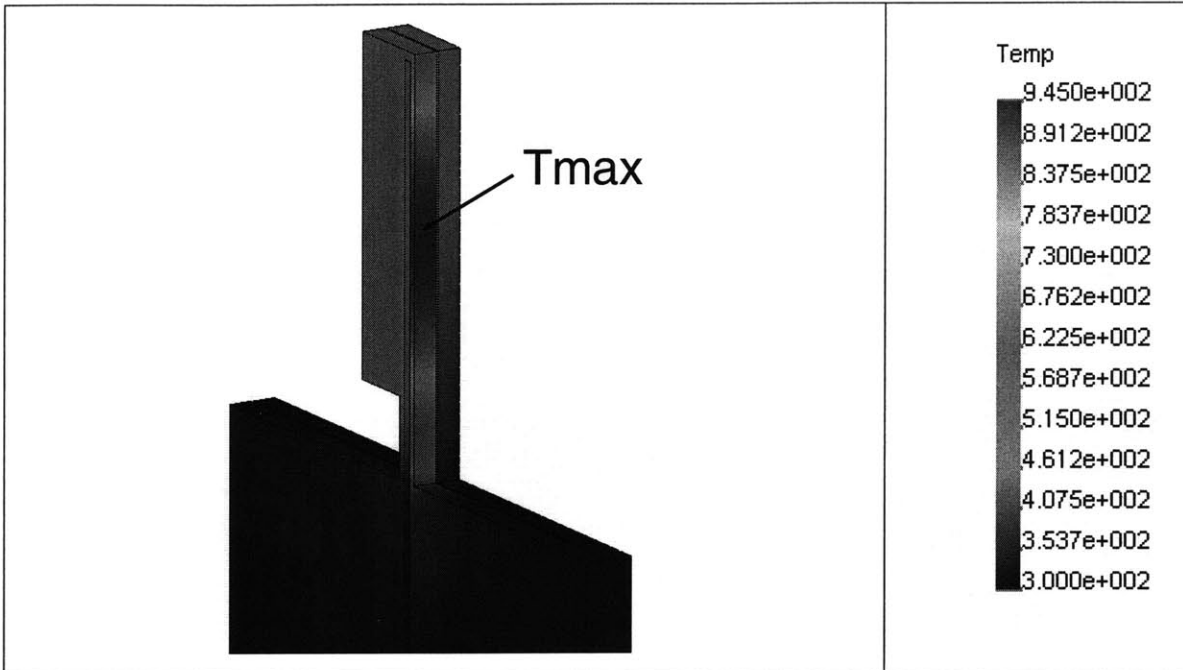
## 2.2.4 Out-of-Plane Actuation Design

The out-of-plane actuation is achieved by attaching two layers of thermal actuators together to create the out-of-plane displacement. This is made possible by the material silicon dioxide between the layers. Silicon dioxide has a thermal conductivity of 1.4 W/mK, which is about 100 times smaller than the single crystal silicon. It also has a large thermal capacitance of 1000 J/KgK, which serves as a perfect thermal insulator between two Micro-Hexflex layers. In Figure 2-23, an out-of-plane thermal actuator model and its mesh are shown. Again, make sure the thinnest section has at least four finite elements.



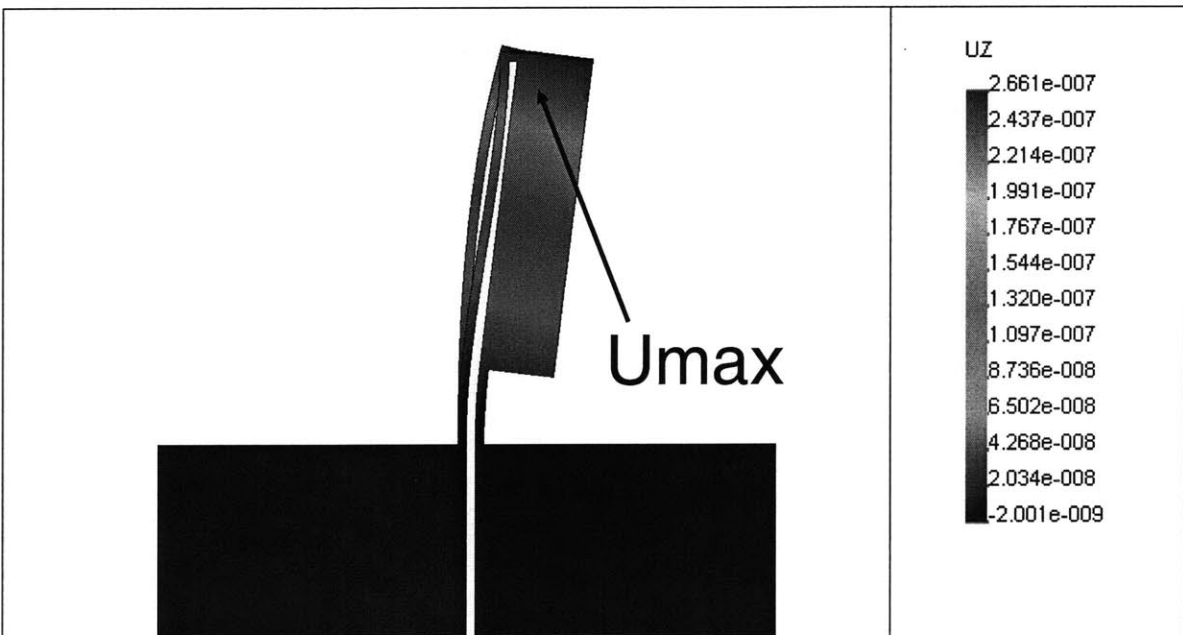
The results from the thermal solver are presented in Figure 2-24. There is a temperature difference between two thin beams from two layers. As the hot beam elongates, the thermal actuator will have out-of-plane displacement.





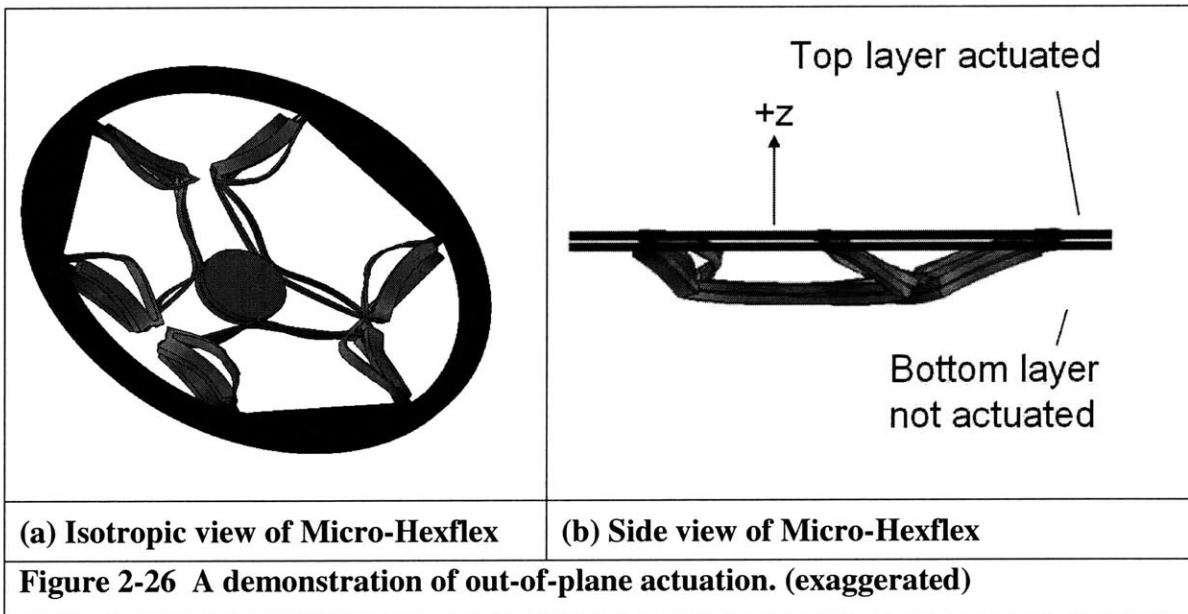
**Figure 2-24 Temperature solution of sandwich structure**

When the result from the temperature solver in Figure 2-24 is substituted into the static structure solver, we find that the thermal actuator provides a 0.26 micron out-of-plane motion as shown in Figure 2-25.



**Figure 2-25 Out-of-plane actuation (exaggerated by factor of 25)**

The basic geometry of the Micro-Hexflex out-of-plane actuation system is built in two layers. The top and bottom layers are identical. The thin middle layer, made of thermal silicon dioxide, anchors the top and bottom layer together by fusion bonding at selected spots. For example, if we actuate the thermal actuators on the top layer, the whole stage will be push down in the direction of negative Z-axis, shown in Figure 2-26 (b). Obviously, we can do out-of-plane rotations of the stage by actuating combinations of different thermal actuators.



A frequency analysis is run again to obtain the first mode of the double-layered Micro-Hexflex. Results are shown in Table 2-19. The first mode is around 34 kHz, which is far above from the operating frequency of the thermal actuator. Thus, the device is safe from resonance effects due to actuation inputs.

Mode	Frequency [Hz]	Period [second]
1	34853	$2.87 \times 10^{-5}$
2	35802	$2.79 \times 10^{-5}$
3	50459	$1.98 \times 10^{-5}$

With a fiber optic cable loaded on the Micro-Hexflex, the in-plane motion would be at most reduced by a factor of 1/2 (for a single layer Hexflex). However, we can still enhance performance by (1) adding more parallel thermal actuators and (2) make the sandwich structure. Figure 2-27 is a model, which the fiber is pivoted/fixed ten millimeter away from the Micro-Hexflex actuator.

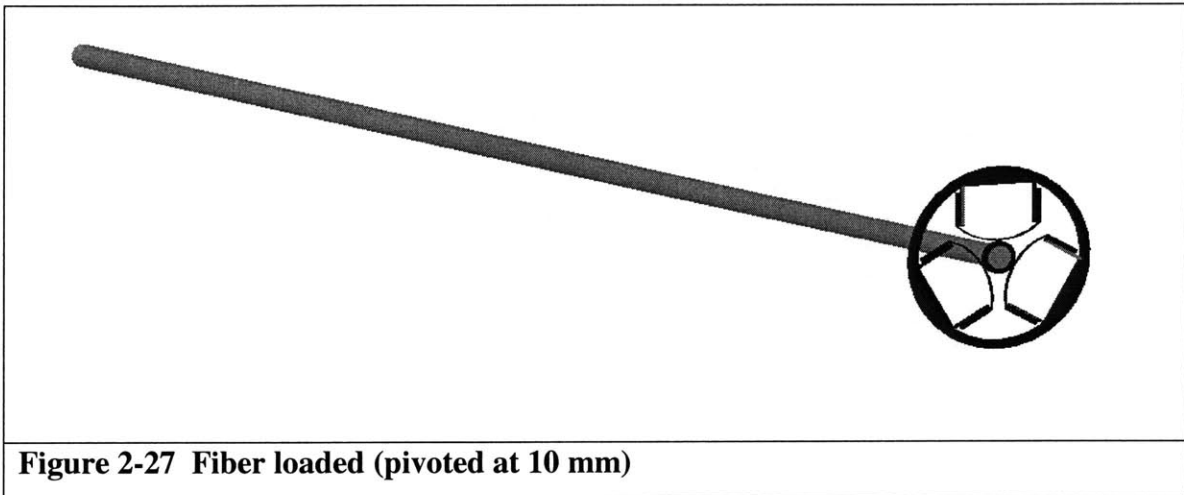
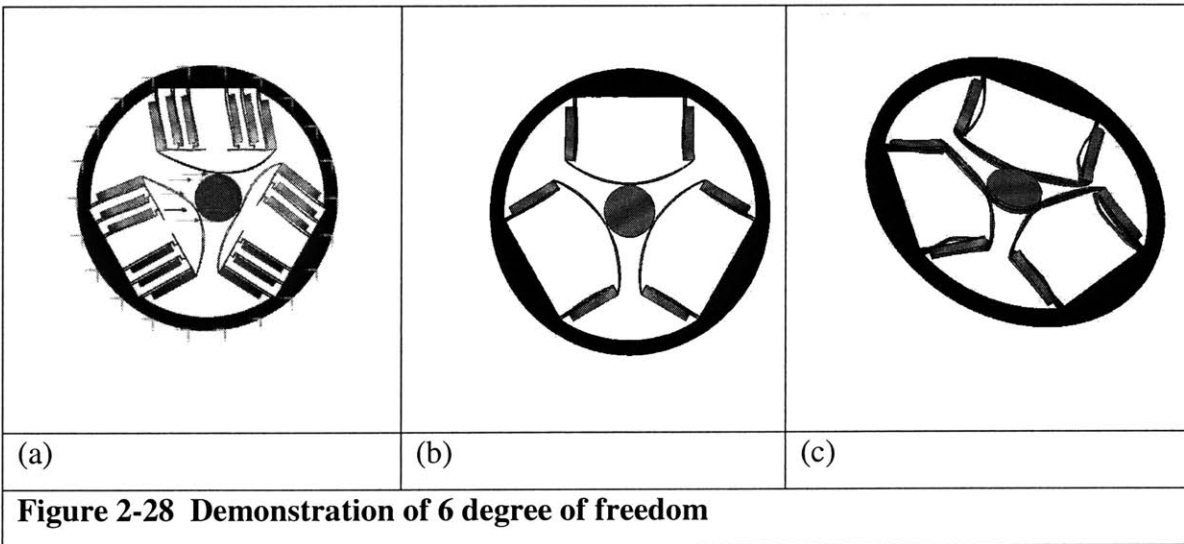
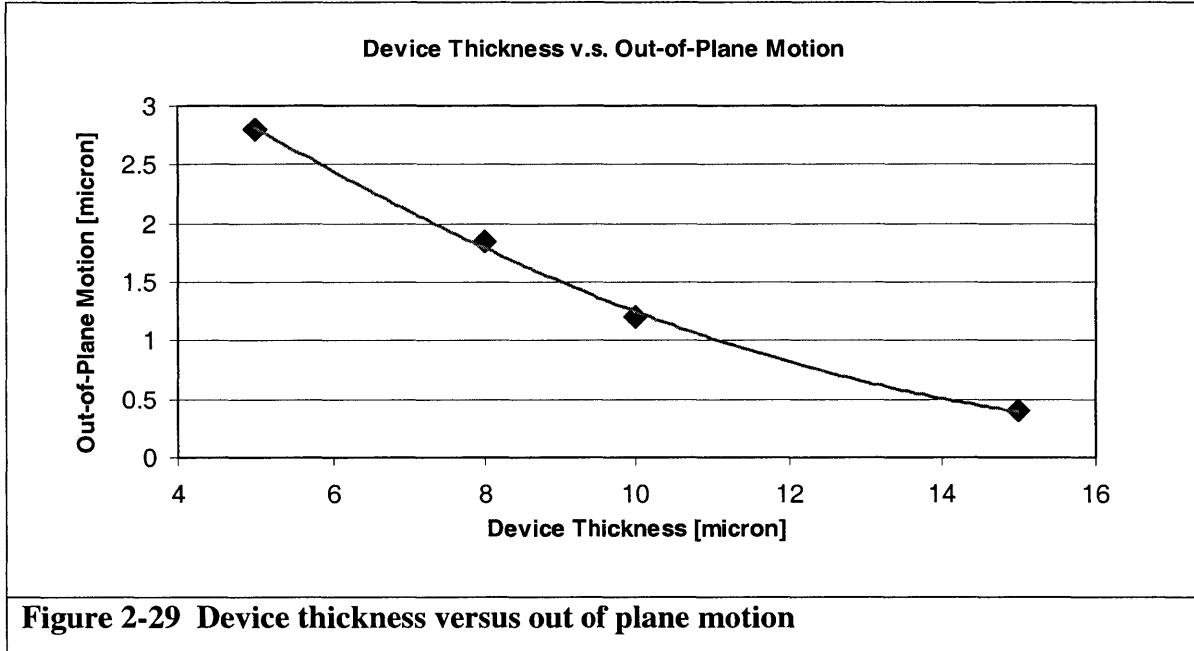


Figure 2-28 (a) shows a concept for parallel actuators, which help to increase the force output. Figure 2-28 (b) and (c) give the demonstration of six-degree-of-freedom motion at different angle.



As for the case of a pair of thermal actuators in Figure 2-25, the Micro-Hexflex only gives the out-of-plane motion about 0.2 microns. However, the out-of-plane displacement

is in fact a function of the thickness of each layer, shown in Figure 2-29. From Figure 2-29, we know for our optimized Micro-Hexflex, where each layer is eight microns thick, the out-of-plane displacement can be around 1.8 microns.



With the double-layered concept, we rebuild the model, and the final optimized performance of double-layered Micro-Hexflex is presented in Table 2-20 and Table 2-21.

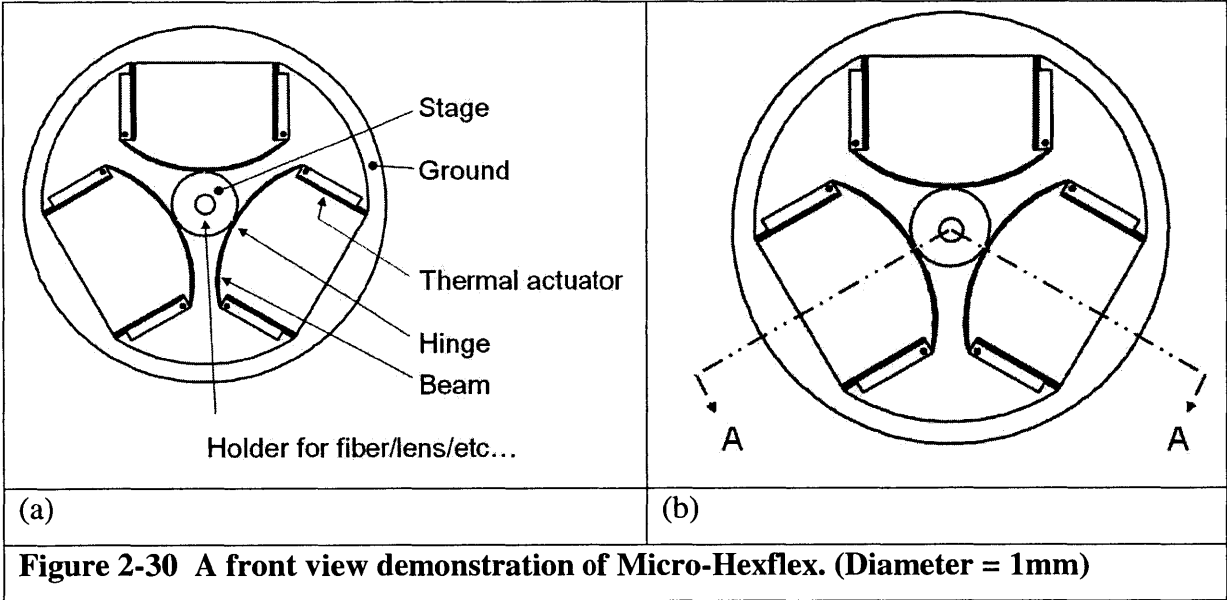
	<b>X[micron]</b>	<b>Y[micron]</b>	<b>Z[micron]</b>	$\theta_x$ <b>[degree]</b>	$\theta_y$ <b>[degree]</b>	$\theta_z$ <b>[degree]</b>
Positive	+2.08	+2.18	+0.90	+1.60	+1.42	+1.42
Negative	-2.08	-2.18	-0.90	-1.60	-1.42	-1.42
Total	4.16	4.36	1.80	3.20	2.84	2.84

Compared to Table 2-17 and Table 2-18, we notice that with the double-layered design, the range of the displacement is not increased and the force output is doubled. This indicates that the displacement is not limited by the output force, but by the geometry of the thermal actuator and compliant mechanism design. However, with the fiber loaded, a larger force output definitely gives more displacement.

<b>Table 2-21 Double-layered Micro-Hexflex predicted performance</b>			
	Force (micro N)	Stiffness (N/m)	Working Temp (°K)
Single layer	~360	120-150	300-800

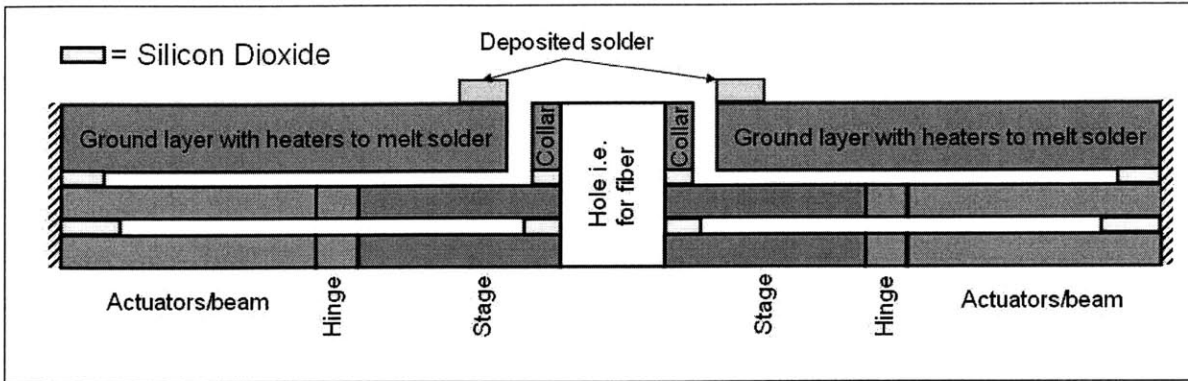
### 2.3 Fixation Design

A low energy consumption stop mechanism needed to fix the load at the desired position. It is not possible to afford the unlimited power or current that flows into the electrothermal actuator. Here, an alignment and fixation process with solder preforms is proposed. Fixation is not a deliverable of this work and is therefore only described. For simplicity, a single structure layer is used to represent the double-layered Micro-Hexflex. Figure 2-30 is the current design result of the top view of the Micro-Hexflex.



**Figure 2-30 A front view demonstration of Micro-Hexflex. (Diameter = 1mm)**

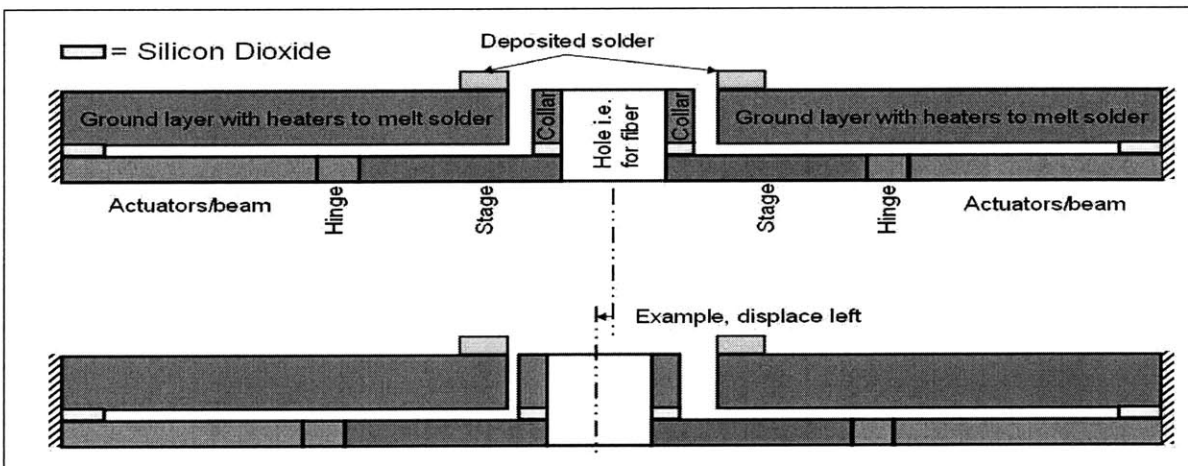
Figure 2-31, Figure 2-32, and Figure 2-33 show cross section A-A of Figure 2-30 (b) during different phases of the fixation procedure.



**Figure 2-31 A cross section of the Micro-Hexflex from (Figure 2-30 (b))**

Step 1: Structure in default position, as shown in Figure 2-31.

Step 2: Actuators stage to desired position, shown in Figure 2-32.



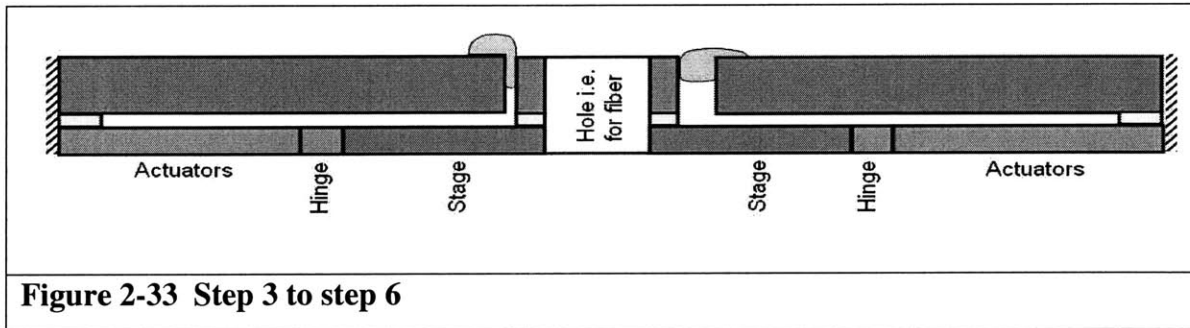
**Figure 2-32 Step 1 and step 2**

Step 3: Solder is melted, flows onto metallized surfaces between second layer and collar.

Step 4: Fixation - Actuators hold stage in place while solder solidifies. Notice here, because the actuators are far removed from solder, heat dissipation will not affect solidification.

Step 5: Power down - Actuators are turned off, solder now holds position

Step 6: Realignment - Solder may be re-melted and alignment adjusted, as shown in Figure 2-33.



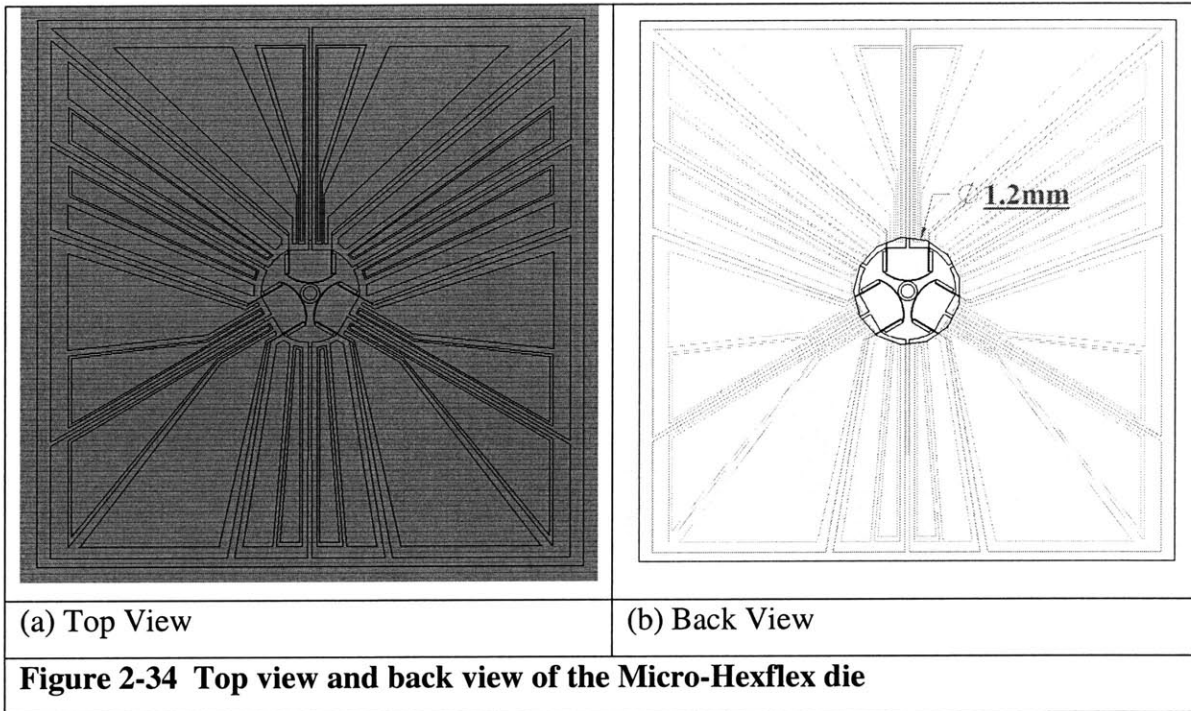


## 2.4 Packaging

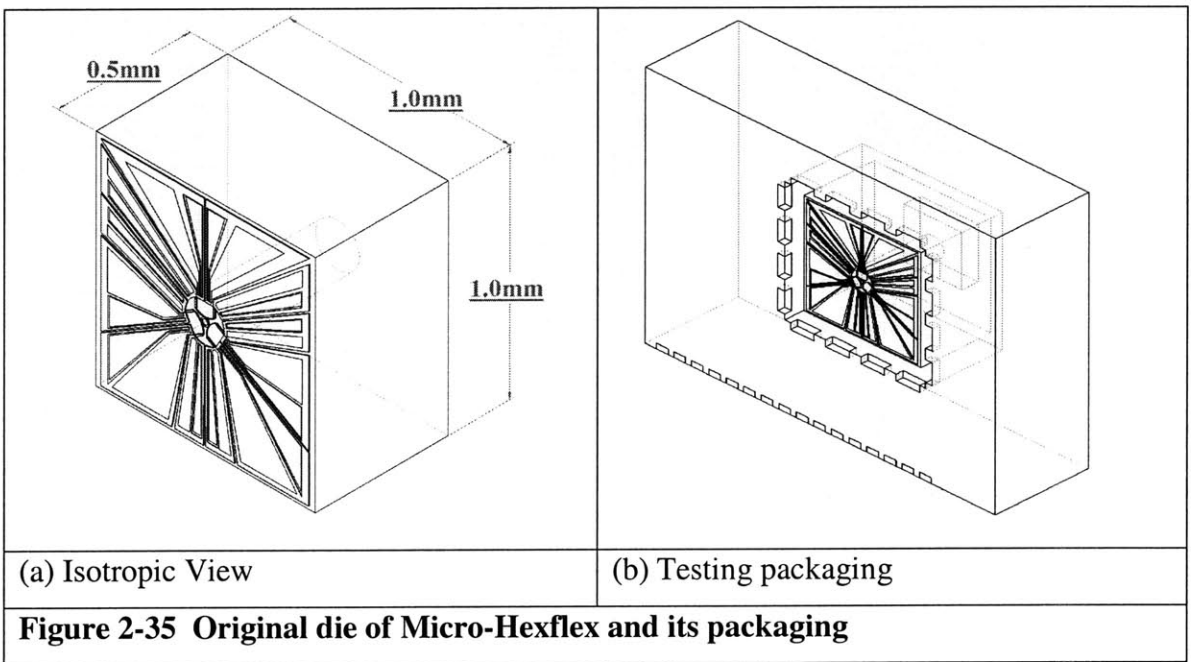
Difficulty with packaging is the biggest obstacle to impede the commercialization of MEMS products. Due to the fact that MEMS usually integrates many different engineering domains into one system, e.g. electrical to mechanical or electrical to fluidic, it is difficult to standardize MEMS packaging. Accordingly, one has to design a specific packaging procedure for each MEMS product. Thus, a better way to prevent an impossible packaging quandary while finalizing the design process is to incorporate the packaging with the development of the device. It is also valuable to do a survey of the current existing foundry and make sure the product can be fabricated with the proper steps and machinery.

The packaging design of Micro-Hexflex will be started with the device design, which ensured the final product would be able to be packaged and reliable. Following factors were taken into consideration when designing the packaging: reliability, cost, fixity, electric inputs/outputs, thermal loading, and hermetical seal.

On the current stage, the packaging of the testing setup for Micro-Hexflex is designed with a larger metal contact for the easy placement of the probes and microscope setup. The wafer, after finishing the process in MTL, will be die-sawed at the size of one centimeter square as shown in Figure 2-34 (a) and Figure 2-35 (a). A hole with a diameter 1.2 millimeter on the backside of the wafer is opened to prevent the stiction effect between the Micro-Hexflex stage and the substrate, as shown in Figure 2-34 (b).



The die-sawed Micro-Hexflex will then be placed into a butterfly lead-out package and wired-bounded for the lab testing, as shown in Figure 2-35 (b).



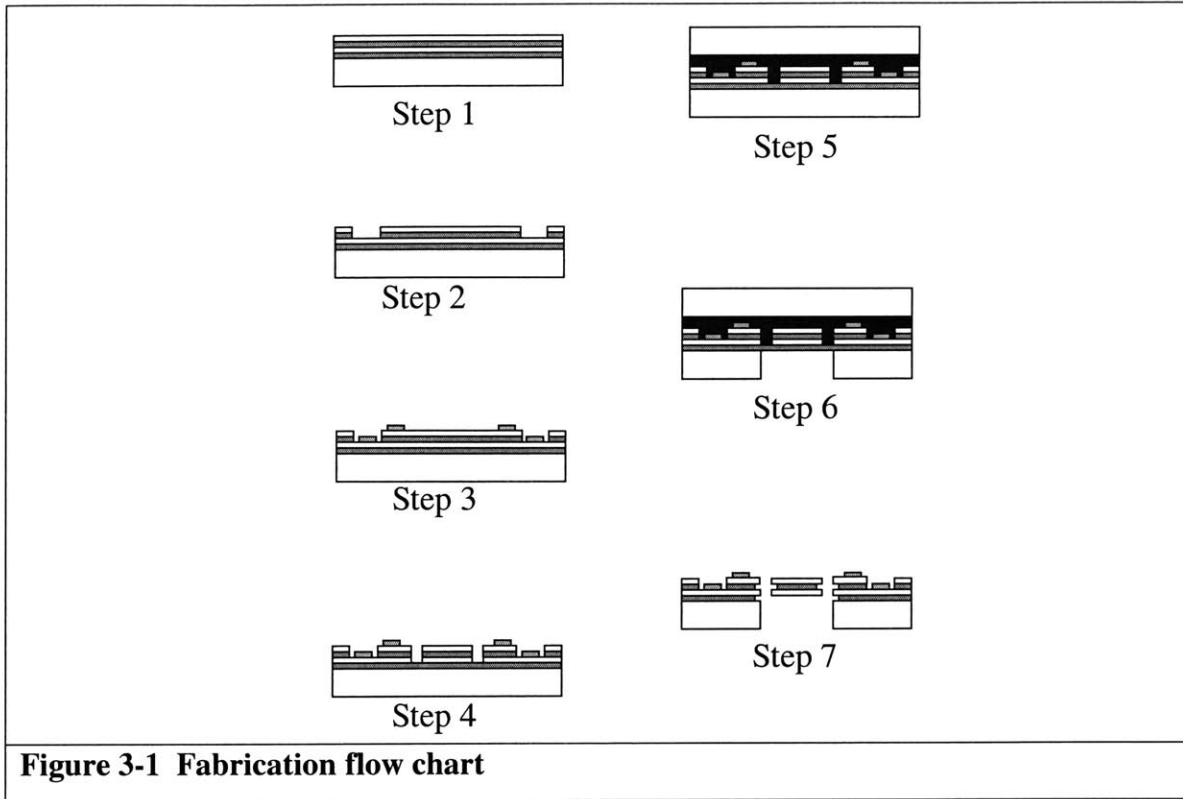
# Chapter 3 Device Fabrication

---

The fabrication of the Micro-Hexflex was carried out in Micro System Laboratory (MTL) at MIT. The MTL houses three clean room facilities: the Integrated Circuits Laboratory - ICL, the Technology Research Laboratory - TRL, and the Nano Structures Laboratory – NSL. Most of facilities for MEMS and micro-fabrication are located in TRL and ICL.

The fabrication process is based on the micro-fabrication technology used in integrated circuits (IC). Figure 3-1 is an overview of the micro-fabrication process of the final version of Micro-Hexflex. Following are the steps in Figure 3-1:

1. The process starts with a silicon on insulator (SOI) wafer of two device layers.
2. Pattern the metal contact opening for the second device layer.
3. Deposit and pattern metal contact of the device.
4. Pattern the Micro-Hexflex structure with deep reactive ion etch (DRIE) alternating with buffered oxide etch (BOE).
5. Use photoresist mount the device onto another silicon wafer.
6. Open the backside of device with DRIE.
7. Release the mounted device and clean the photoresist.



The steps here are only a brief idea of how the process is designed. More detailed discussions on the processes introduction and selection will be stated in the following sections.

## 3.1 Review of Micro-Fabrication Process to be Used

In this section, all the fabrication processes and methods used to build the Micro-Hexflex are introduced with emphasis on basic processes to make the fabrication process and design part more readable.

### 3.1.1 Wafers

Micro-Hexflex needs a multi-layer structure to achieve its out-of-plane motion and each layer should be of

1. High quality: single crystal silicon or thermal oxide
2. Thickness: at least 8 microns for the strength to move a fiber.

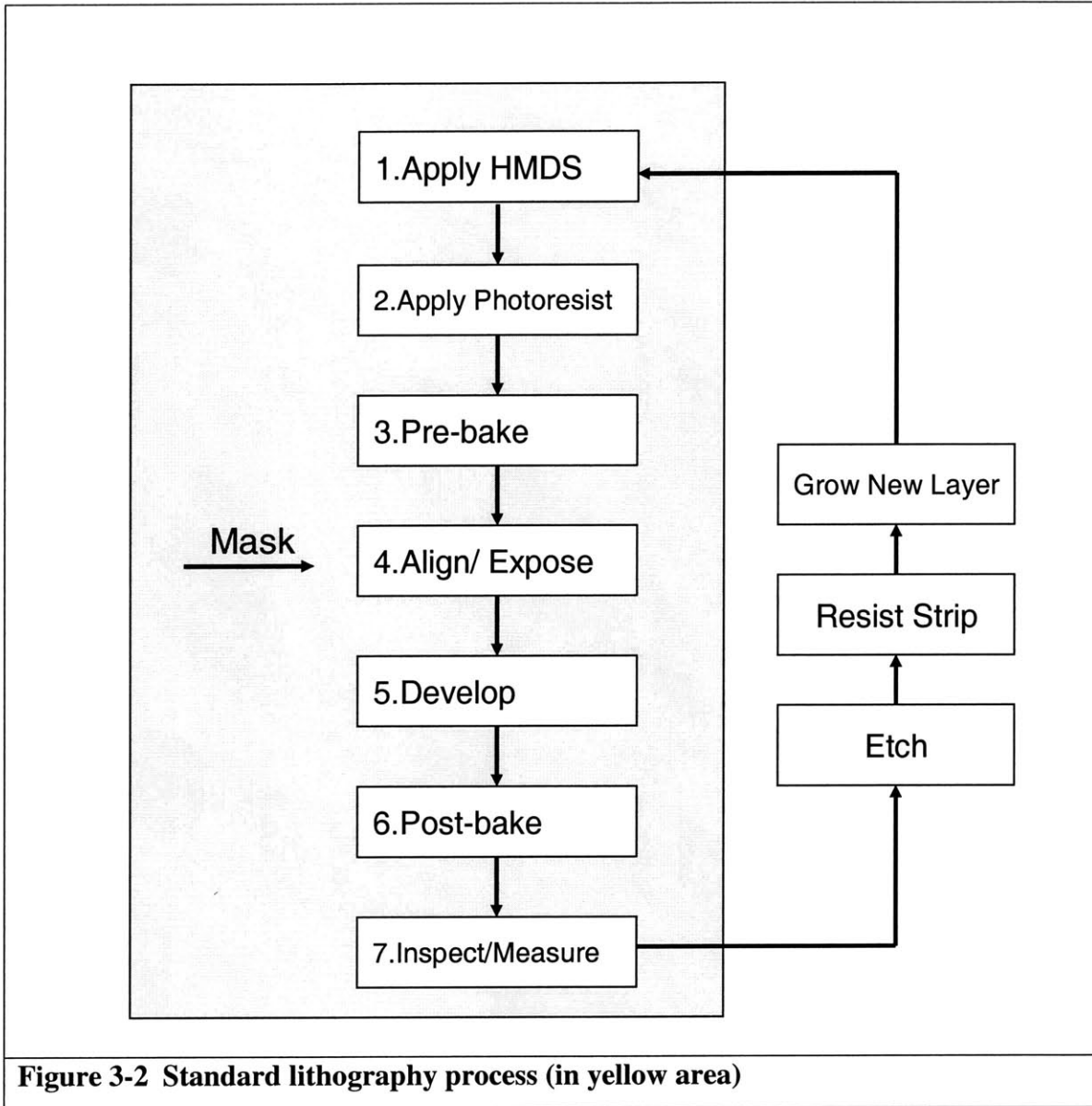
Surface micro machining is not the best choice for the Micro-Hexflex because the deposited or evaporated polycrystalline silicon is composed of microscopic grains of silicon, which results in a residual stress as a function of temperature. Thus, the silicon-on-insulator (SOI) wafer seems to be the best choice for the device requirement. In SOI, silicon wafers are replaced with wafers that have three layers: a device layer with silicon (from few angstroms to hundreds of microns), an underlying layer of insulating material, and a support or “handle” silicon layer [22]. The wafers are made by growing thermal oxide at the specified thickness on the handle layer, and subsequently bonding another wafer to the oxide layer. Chemical-mechanical polish the device and handle layers to the desired thickness. The SOI wafers possess excellent structural and electrical uniformity, and also the oxide layer can serve as the insulator between different layers.

A variation of an SOI wafer, a SOIOI is the right choice for Micro-Hexflex. The double-layered SOIOI wafer contains two device layers, two oxide layers, and a handle layer, which make the double-layered out of plane actuation fabrication plan feasible.

### **3.1.2 Lithography**

Lithography is the process of transferring patterns from a master mask onto a silicon substrate. Photolithography is the one used most common method in IC and MEMS fabrication. The combination of accurate registration in exposing a series of successive patterns enables complex multi-layer ICs. The lithography process, which occupies around 50% of the total time of device fabrication, is worthy of moderate detailed explanation. Lithography generally consists of five major steps: as illustrated in Figure 3-2:

1. Apply photoresist
2. Pre-bake
3. Align and expose
4. Develop
5. Post-bake



The following explains the processes in Figure 3-2:

1. The purpose of applying Hexamethyldisilazane (HMDS) vapor is to dehydrate the surface and promote the adhesion between the photoresist and the surface of the wafer. (In the TRL, HMDS oven.)
2. Static or dynamic dispense the photoresist on a vacuum wafer chuck. Then, spin coat the photoresist on the wafer. The thickness of the photoresist is a function of the spin speed at a variation speed from 2000-6000rpm, which depends on the etching requirement. (In the TRL, coater)

3. After the Photoresist is uniformly distributed on the wafer, the wafer is sent to the Prebake oven at 90oC. The soft-bake is to drive off the unnecessary solvents in the photoresist. (In the TRL, Pre-bake oven)
4. Expose the photoresist with appropriate energy source. For most quartz/chrome plates, ultra violet (UV) light or deep UV lights should be good. Bright sources are usually required for high throughput; the exposure time should be determined by experimental data. The aligner has three types/modes: contact, proximity, and projection. Projection is slow, but good for fine resolution. Contact mode is also of fine resolution. However, the mask and the wafer are in contact, which might damage each other by undesired scratching and particles. The resolution of every type of exposure mode here is in fact limited by the diffraction of optics. Thus, the only solution to define a nano-scale pattern is to use the light source with a shorter wavelength, for example X-ray, or electron beam. The Electronic Visions Model EV620 Mask Aligner (EV1) in the TRL, which uses an exposure system of 350-watt high pressure mercury lamp (the wavelengths are 365-405nm), can achieve a sub- micron resolution in contact mode on devices with appropriate masks. Thus, EV1 is chosen to be used in our device fabrication.(In the TRL, EV1)
5. After exposure, develop the pattern in the appropriate developer (Hydroxide). Puddle or spray in temperature controlled environment. Finally, rinse and dry with nitrogen gun.
6. Post-bake, also called hard-bake, bakes the wafers in a higher temperature at 120oC to harden the photoresist. (In the TRL, Post-bake oven)
7. Inspect the pattern under the microscope to see if the desired patterns are properly formed. Also, measure the thickness of the photoresist before sending the wafer to etch. If the pattern or thickness is not correct, the photoresist should be removed (by Piranha or Asher) and reapplied.



### **3.1.3 Metal Evaporation**

In metal evaporation, the substrate is placed in a high vacuum chamber at room temperature with a crucible containing the material to be deposited. A heating source is used to heat the crucible causing the material to evaporate and condense on all exposed cool surfaces of the vacuum chamber and substrate. The process is typically performed on one side of the substrate at a time. Typical sources of heating are: Electron beam (E-beam), Resistive heating, RF-inductive heating. In some systems the substrate can be heated during deposition to alter the composition and stress of the deposited material. The metal contact for the Micro-Hexflex is evaporated in ICL with E-beam, which gives the purest metal possible.

### **3.1.4 Etching**

Etching is the process of removal the undesired material that is uncovered by the photoresist. Several important parameters like etch rate, selectivity, isotropic etching (undercut), and anisotropic etching, are the ones we should pay more attention when design the etching process. A high etch rate is generally desirable in a manufacturing environment, however, too high of an etch rate may make a process difficult to control. Selectivity is the ratio of the etch rates over various materials, such as silicon (structure layer) over photoresist or substrate material (sacrificial layer). Undercut is the lateral extent of the etch under photoresist mask. It usually results from the isotropic etching.

#### **3.1.4.1 Wet etching**

Wet etching is a purely chemical process that has some unavoidable drawbacks: a lack of anisotropy, poor process control, and excessive particle contamination. However, it is usually high selective and does not damage the substrate. As a result, it continues to be used for a wide range of tasks. Comprehensive review of wet etching can be found elsewhere [23]. During the process of the fabrication of the Micro-Hexflex, most processes of removal silicon dioxide ( $\text{SiO}_2$ ) are done by wet etching with hydrofluoric acid (HF). HF solutions are extremely selective of oxide over silicon. Selectivities are

usually better than 100 [24]. Common HF etchants are 6:1, 10:1, or 20:1, meaning 6, 10, 20 parts of water to one part HF. A 6:1 HF solution will thermal dioxide at about 1200 Angstrom/min and deposited oxides are usually tend to etch much faster. The exact pathway is complex and depends on the ionic strength, the solution pH, and the etchant solution [25]. The overall reaction for etching SiO<sub>2</sub> is



Since the reaction consumes HF, the reaction rate will decrease with time. To avoid this, it is common to use HF with a buffering agent (Buffered Oxide Etch, BOE), such as ammonium fluoride (NH<sub>4</sub>F), which maintains a constant concentration of HF through the dissolution reaction



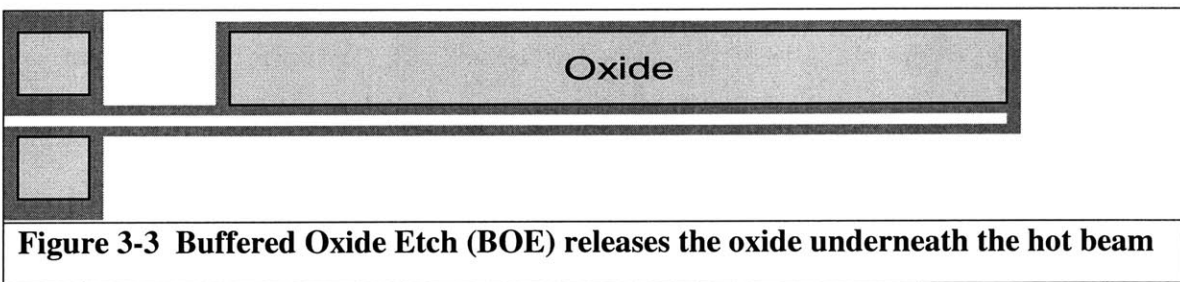
Buffering also controls the pH of the etchant, which minimizes the photoresist attack. For concentrated HF has a 49% proportion of HF, and the etch rate is from 18000 to 23000 angstrom/min to SiO<sub>2</sub>.

Wet etching of oxide in HF solution is completely isotropic, which helps the removal of the oxide lying between two hot beams in the thermal actuators. Since the HF will not go in too deep in limited time, it is required to use a wet etching in our purpose of application as shown in Figure 3-3 [25].

Now, we give an example to calculate how much time we should immerse the wafer into BOE to get a structure in Figure 3-3. The thin beam is 4 micron wide, and the etch rate for the BOE to oxide is 1000 Angstrom/min. Thus, the time we should use is:

$$\text{Time} = (4/2[\text{micron}]) / (0.1[\text{micron}/\text{min}]) = 20 \text{ minutes.}$$

Since a little bit over etch will not damage the device as shown in Figure 3-3, it is recommended to use a 25 to 30 minutes total to make sure the oxide is removed thoroughly.



### 3.1.4.2 Dry etching

Dry etching is also called physical etching, which refers to remove the undesired material from the target wafer in the gas or vapor phase in a physically way. It includes physically ion bombardment (Like, sputtering, or ion itching), chemically by a chemical reaction through a reactive species at the surface (Like, reactive ion etching), or by combined physical or chemical mechanisms. Usually, the dry etching is more anisotropic than wet etching. Following, a commonly used process in building Micro-Hexflex called deep reactive ion etching is introduced.

#### 3.1.4.2.1 Deep Reactive Ion Etching (DRIE)

Silicon deep reactive ion etching (DRIE) is a versatile tool for the fabrication of MEMS. It enables the bulk micromachining of silicon with aspect ratios (ratio depth to width) up to 30:1 and sidewall angles of  $90^\circ \pm 2^\circ$ . Compared to other bulk micromachining methods it is anisotropic and independent of the crystal orientation. Therefore it allows a

high degree of design freedom and thus will be the main dry etching tool to build the Micro-Hexflex.

The basic idea of silicon deep reactive ion etching (DRIE) is an alternating etch and surface passivation step. (It is developed and patented by Robert Bosch GmbH.) [26][27]. The dry etching of silicon according to this principle is also called High Aspect Ratio Silicon Etching (HARSE), Bosch Deep Silicon Etching, or Advanced Silicon Etching (ASE; Trademark of Surface Technology Systems Ltd.).

The etch rate can be over  $10\mu\text{m}/\text{min}$ , the surface roughness of the sidewall as low as 10nm, or the homogeneity of the etch depth less than  $\pm 3\%$  (on a 4" wafer). However, the final etch result is mostly a compromise. With a high etch rate, the surface roughness increases, with a large etched silicon area the homogeneity will increase to above  $\pm 10\%$ .

For the fabrication of movable structures silicon-on-insulator (SOI) wafers are often used. The oxide beneath the silicon acts as an etch stop layer. By a subsequently removal of the oxide the structures are released. Other applications require several planes with a varying etch depth. This is achieved by using more masks which are removed subsequently. For curved sidewall profiles grey-scale lithography can be applied [28] [29].

## 3.2 Design of Fabrication Process






Two prototypes of Micro-Hexflex are designed and fabricated. The first one is designed to test the thermal actuator and the in plane performance. It has three degree of freedom (in plane) and is made of a SOI wafer. The second prototype, which has been introduced in the beginning of this chapter, is the final device with six-degree-of-freedom, built on a double SOI wafer.

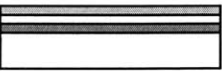
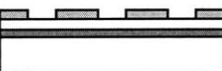
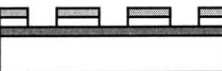
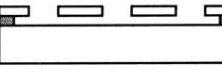

### 3.2.1 Single Layer Prototype Fabrication

The fabrication idea for first prototype is simple:

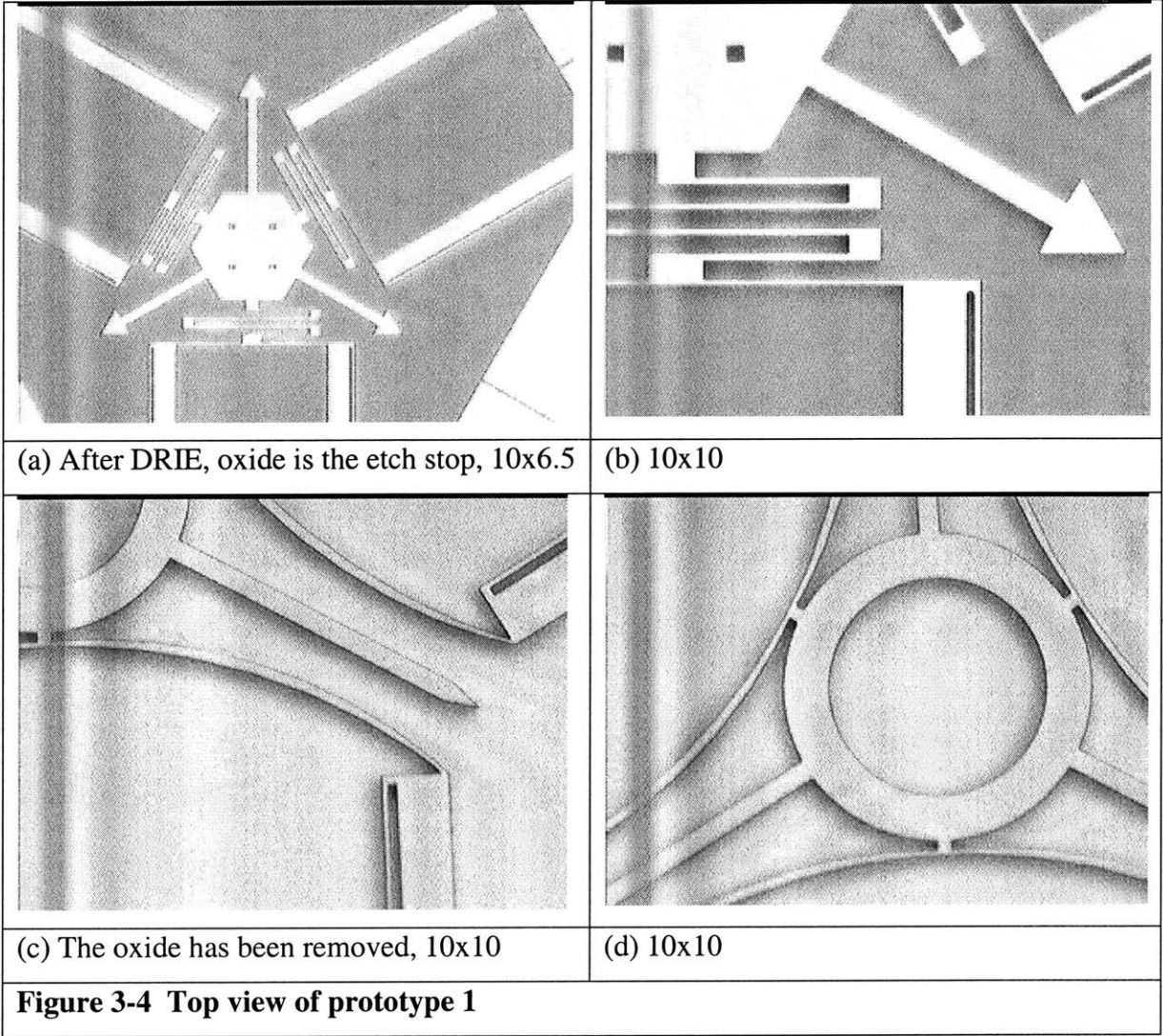
1. Pattern the device layer with DRIE.
2. Remove the oxide layer beneath by concentrated HF (49%), which has a etch rate about 23000 Angstrom/min for wet oxide.
3. Pattern the aluminum by E-beam.

The detailed process and fabrication variable of this in plane Hexflex is in Table 3-1.

<b>Table 3-1 Fabrication of prototype 1</b>			
			
<b>Oxide</b>	<b>Photoresist</b>	<b>Silicon</b>	<b>Aluminum</b>
Step	Lab	Machine(Café)	Recipe/Description
	TRL		Start with a 6 inch SOI wafer. The device layer is 15 microns thick, and oxide layers 0.8 micron thick.


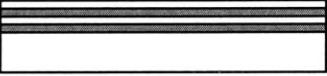

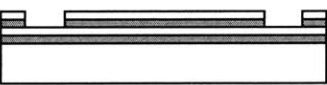
	TRL	HMDS	Apply HMDS in the oven with the thin photoresist recipe.
	TRL	Coater	Spin standard photoresist at 1micron
	TRL	Prebake	Pre-bake 30 minutes at 90°C.
	TRL	EV1	Expose to UV light for 2 seconds and Develop for 60 seconds.
	TRL	Postbake	Post-bake 30 minutes at 120°C.
	ICL	STS2	Etch unprotected Silicon device layer by DRIE.
	TRL	Acidhood	Etch Oxide layer with concentrated HF.
	TRL	Acidhood	Strip photoresist and do pre-metal clean with Piranha. (A solution of 3:1 H <sub>2</sub> SO <sub>4</sub> : H <sub>2</sub> O <sub>2</sub> .)
	ICL	E-beam	Aluminum (Al) Deposition.
		Rainbow	Pattern Al with metal dry etching.
	ICL	Asher	Strip photoresist (Oxygen Plasma Etching). Aluminum Sintering
		RTA2	(annealing). Device done.

The pictures of the first prototype are shown in Figure 3-4 from (a) to (d). In Figure 3-4 (a) and (b), the wafer is just taken out from the DRIE machines (STS2). There is a color difference between the structure and the substrate. The oxide, which serves as the etch stop for DRIE, appears purple and silicon is white. In Figure 3-4 (c) and (d), the oxide has been removed by concentrated HF, which makes the color the same again. Also, there is an observable distance (16 microns) between the device layer and the substrate.

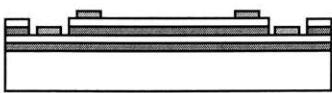


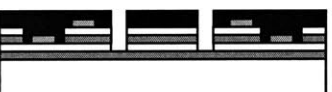




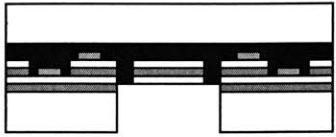

### 3.2.2 Double Layer: 6DOF Micro-Hexflex

The idea of the fabrication has been shown in the beginning of the chapter. Table 3-2 shows the detailed fabrication process of the double layered Micro-Hexflex.

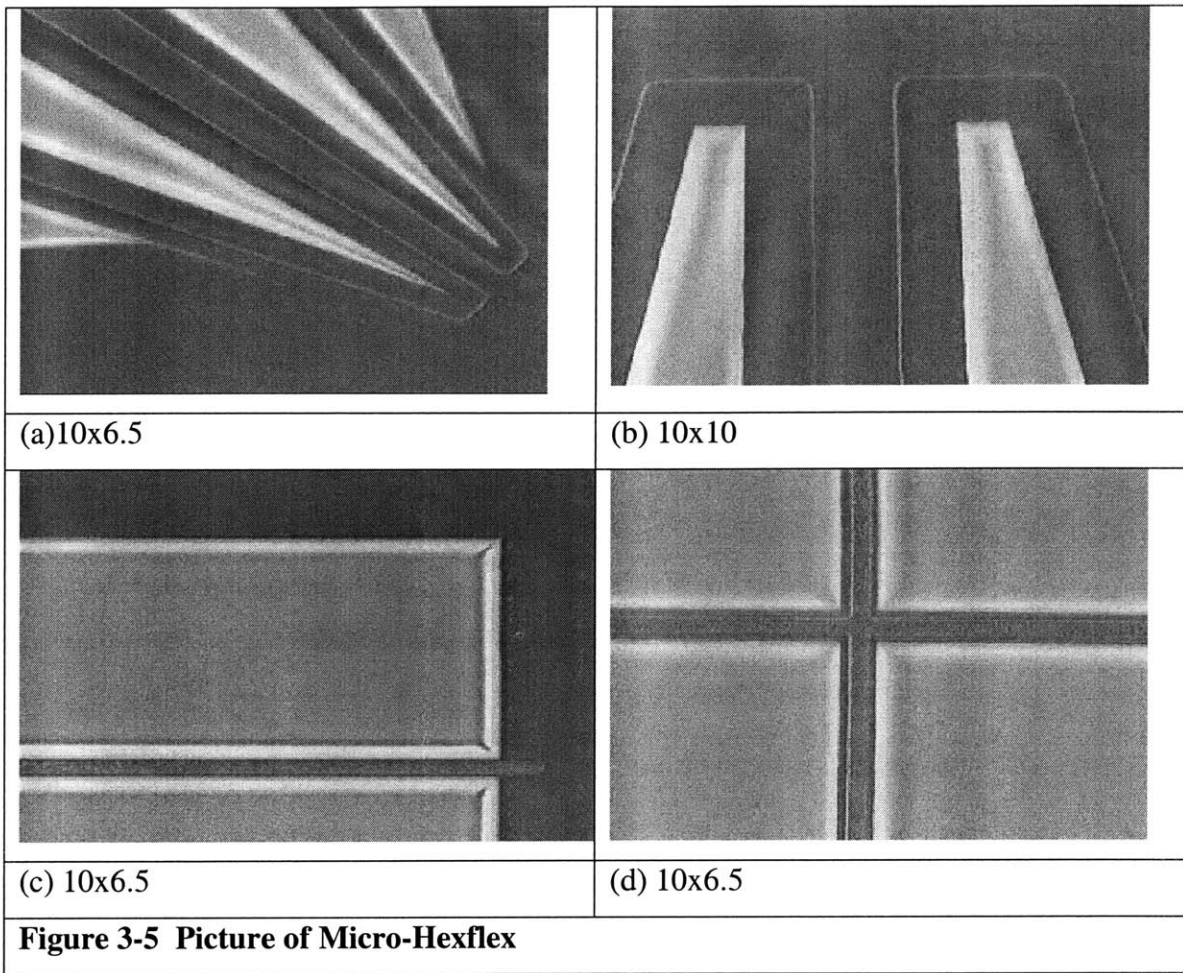
Table 3-2 Fabrication of prototype 2			
			
<p style="text-align: center;"> <span style="margin-right: 100px;">Oxide</span> <span style="margin-right: 100px;">Photoresist</span> <span style="margin-right: 100px;">Silicon</span> <span>Aluminum</span> </p>			
Step	Lab	Machine	Recipe/Description
	ICL	(Coral)	Start with a 4 inch SOI wafer with 2 device layers of thickness 8 microns, and both oxide layers 1 micron. (The wafers are ordered from Ultrasil. The 4" wafer is chosen because of this specific order can be available faster with a 4" wafer and also it's a lot cheaper.)
	TRL	Coater/Prebake/ EV1/photowet/P ostbake	Apply and pattern photoresist as a mask layer.
	TRL	STS1	Use recipe "Fardad" (A recipe developed in MTL for fine resolution thin silicon patterning.) in STS1. Wet etch the oxide layer in BOE. Remove the photoresist
	TRL	Acidhood	
	TRL	Asher	



			layer in Asher.
	ICL	E-beam	Pattern the CMOS metal, Al-2%Si, as the metal contact of the actuators on the first and second device layer. Thickness of Al: 5000 angstrom. The Al can also be patterned by BOE with an etching rate: 1400 angstrom/min.
	TRL	Coater/Prebake/ EV1/photowet/P ostbake	
	TRL	Acidhood	
	TRL	Asher	
	TRL	Coater/Prebake	Spin thick photoresist on device layer and pre-bake.
	TRL	EV1/photowet/ Postbake	Expose the photoresist in EV1. Develop and pattern the mask geometry. Postbake.
	TRL	STS1	Use recipe Fardad in STS1 to pattern first layer. Wet etch the oxide layer in between with BOE, Use STS1 again to pattern the second layer. The second structure layer here is 8 microns thick too.
	TRL	Acidhood	
	TRL	STS1	
	TRL	Postbake	Apply photoresist and target mount on another wafer before sending to STS1.
	TRL	Coater/Prebake/ EV1/photowet/P ostbake	Do backside alignment on EV1, pattern and open holes on the handle layer to prevent stiction effect.
	TRL	STS1	

	TRL	Acidhood	Use BOE to etch the undesired oxide layer at the opening and then immerse the wafer into acetone to release the wafer and dissolve the photoresist.
	TRL	Asher	Remove/clean the photoresist by plasma etching. The device is done.

The pictures in Figure 3-5 shows four 10x6.5 and 10x10 pictures taken from the microscope. Picture (a) and (b) are the metal contact of the Micro-Hexflex. It was then covered by the thick resist of 10 microns thick. The variation of the color says that it is tapered on the fringe of the thick resist. The background was covered by the Al-2%Si, which will be later removed by a BOE. Picture (c) and (d) shows the accurate registration of the alignment mark patterned by two different masks



### 3.3 Fabrication Considerations

Important fabrication concerns and selections of alternate fabrication process, which might affect the results and performances of the device, are discussed and presented in this section.

#### 3.3.1 Stiction effect

Stiction effect happens when the capillary forces are larger than the structure stiffness and thus “pull down” the structure during the rinsing or drying process. After two micro structures are in contact, van der Waal forces, electrostatic force, and hydrogen bond take place, and permanently bond two structures together. To avoid this, first, design the structure so that the capillary force is larger than the adhesion force. Secondly, supercritical or vapor-phase dry the deionized wafer (DI wafer<sup>2</sup>) on the surface. If these methods are unavailable due to equipment or device design, it is best to immerse and rinse the device in acetone several times to make sure there is no wafer beneath the structure.

In prototype one (In-plane Hexflex), stiction happened on most of the devices when releasing them. Finally, openings from the backside of the wafer beneath the devices are designed to thoroughly avoid the possibilities of stiction effect, which helps in design and fabrication in double-layered Micro-Hexflex.

---

<sup>2</sup> City water goes through a multi-media filter where large particles are removed. The water goes through an ultra-filter, where anything with a molecular weight above 100,000 is filtered out by hollow fiber filters. The chlorine is removed in charcoal beds. The water is then circulated through UV lamps, where bacteria are disabled. The water goes through a reverse osmosis filter, where the material flows against its concentration gradient. The result is very pure water with high ionic concentration. The ions are removed until the resistivity reached ~18 meg/ohm. This is the DI water that is sent to the processing labs in Teflon pipes.

### **3.3.2 Variations**

Small geometry variations of the micro-structures will sometimes affect the performance of the devices a lot. Thus, in the fabrication, how different variables/parameters affect the output device dimension/ property is important to mention. Preclude the error sources from the misalignment of the masks. There are still two main sources of errors:

1. Transferring the pattern from the mask to photoresist
2. Pattern the device from photoresist

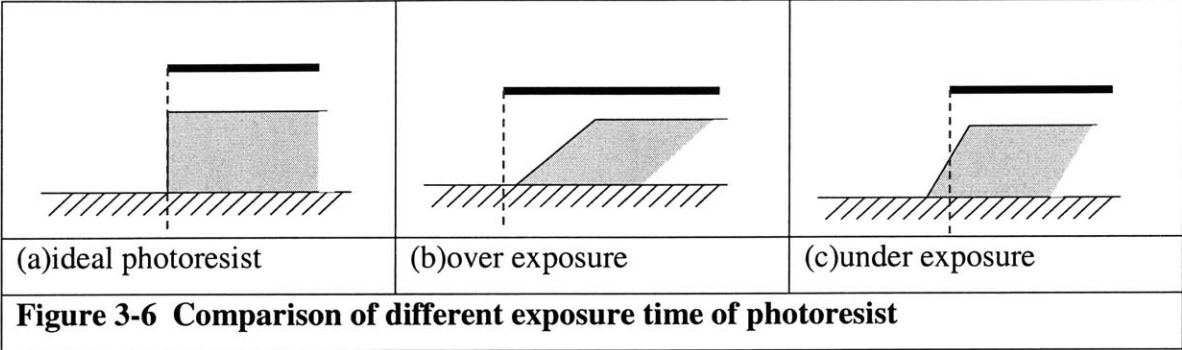
They will be discussed in the following sub-sections.

#### **3.3.2.1 Pattern Transfer of Photoresist**

In the process of lithography, the variables which affect the geometry/resolution are: exposure time, developing time, type of photoresist. Figure 3-6 (a) shows an ideal case of photoresist geometry, which protects the underneath desired structure. The thick line on top of the photoresist represents the mask location. In the over exposure case, shown in Figure 3-6 (b), the attenuated power (light) source, due to diffraction effect, will accumulate enough power to modulate the photoresist underneath the mask. In the under exposure case, shown in Figure 3-6 (c), the photoresist will not be thoroughly removed from the unwanted area. In the worst case, if the exposure is too short, the photoresist will not develop at all. In any case, photoresist profile will not be perfect straight as shown in Figure 3-6 (a). Because of a finite contrast of photoresist, the slope on the edge is not avoidable. However, better photoresist profile that creates right geometry still can be achieved by applying appropriate exposure/developing time. The exact time can be gained by doing a series of different exposure test on testing wafers. Inspect them under the microscope and decide the best exposure time for the case. The exposure time differs from case to case and from machine to machine. So, it is always recommended to do such a test before starting any fine resolution lithography.

Thin resist usually has a much higher resolution than thick resist. For example, the positive thin resist, OCG 825, used in our micro-fabrication can easily achieve a sub-

micro resolution. For a ten-micron-thick photoresist, its resolution comes down to around one micron. In Figure 3-6 (b) and (c), for example, it is obvious that a much higher resolution can be achieved by a thinner photoresist.



**3.3.3 Alternative Fabrication Process**

Some alternative fabrication methods which are able to replace some of the processes that have been used are presented in Table 3-3. The discussions and reasons are laid out in the comment column in Table 3-3.

<b>Table 3-3 Alternative fabrication solution for Micro-Hexflex</b>		
DRIE (pattern device)	RIE (reactive ion etching)	RIE works for shallower silicon patterning. However, to achieve a better aspect ration for our device. DRIE is used.
E-beam (deposit metal)	Metal sputtering	Sputtering also gives a low stress good quality metal film. Both E-beam and metal sputtering are good choices.
BOE (remove oxide)	Metal dry etcher	The isotropic undercut property is necessary for the Micro-Hexflex. So, BOE is used.

Asher (plasma removal of photoresist)	Piranha (A solution of 3:1 H <sub>2</sub> SO <sub>4</sub> : H <sub>2</sub> O <sub>2</sub> )	Piranha has lots bubbles coming up from the liquids. Thus, for fine structure devices, the slower plasma etcher is more often used.
EV1 (contact or soft contact alignment)	I-stepper (projection aligner)	Both of them have enough resolution for Micro-Hexflex. But, to keep most of the process in TRL, we choose EV1.

### 3.4 Summary

The chapter has introduced enough micro-fabrication technology to build and design a double-layered Micro-Hexflex. The prototype one, in-plane Micro-Hexflex, finally hasn't been used in testing because many of the structures are damaged by stiction effect. Based on prototype one, prototype two is designed and built to get a full range of six-degree-of-freedom motion. We have gained valuable fabrication experiences that are discussed in this chapter.

We have a successful design and fabrication plan of double-layered Micro-Hexflex. All the testing and characterization in the following chapters are based on the second version of Micro-Hexflex.

# Chapter 4 Testing and Characterization

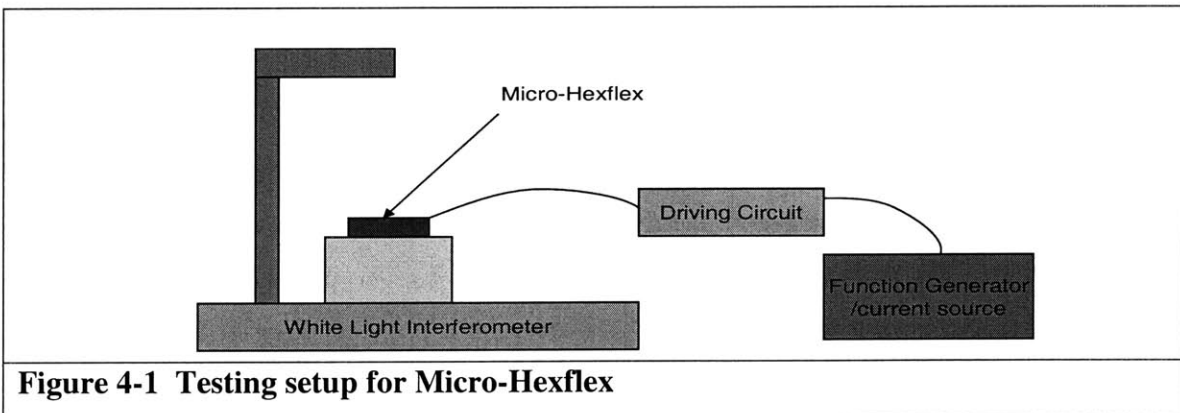
---

This chapter consists of two parts. In section 4.1, the proposed testing methodology for the Micro-Hexflex is presented. Sections 4.2 to 4.4 cover the fabrication and testing of a macro-scale version of the Micro-Hexflex to prove out the concept of the dual layered structure.

## 4.1 Proposed Testing Setup for Micro-Hexflex

### 4.1.1 Static Response

The linearity of the system between the output displacement and the input is important. The displacement of Micro-Hexflex will be inspected with the ZYGO, the white light interferometer, as shown in Figure 4-1. ZYGO has the ability to scan the 3D surface of a micro-structure and gives a resolution in Z direction of five nanometers. For the in-plane scanning, ZYGO provides 0.1 micron resolution.



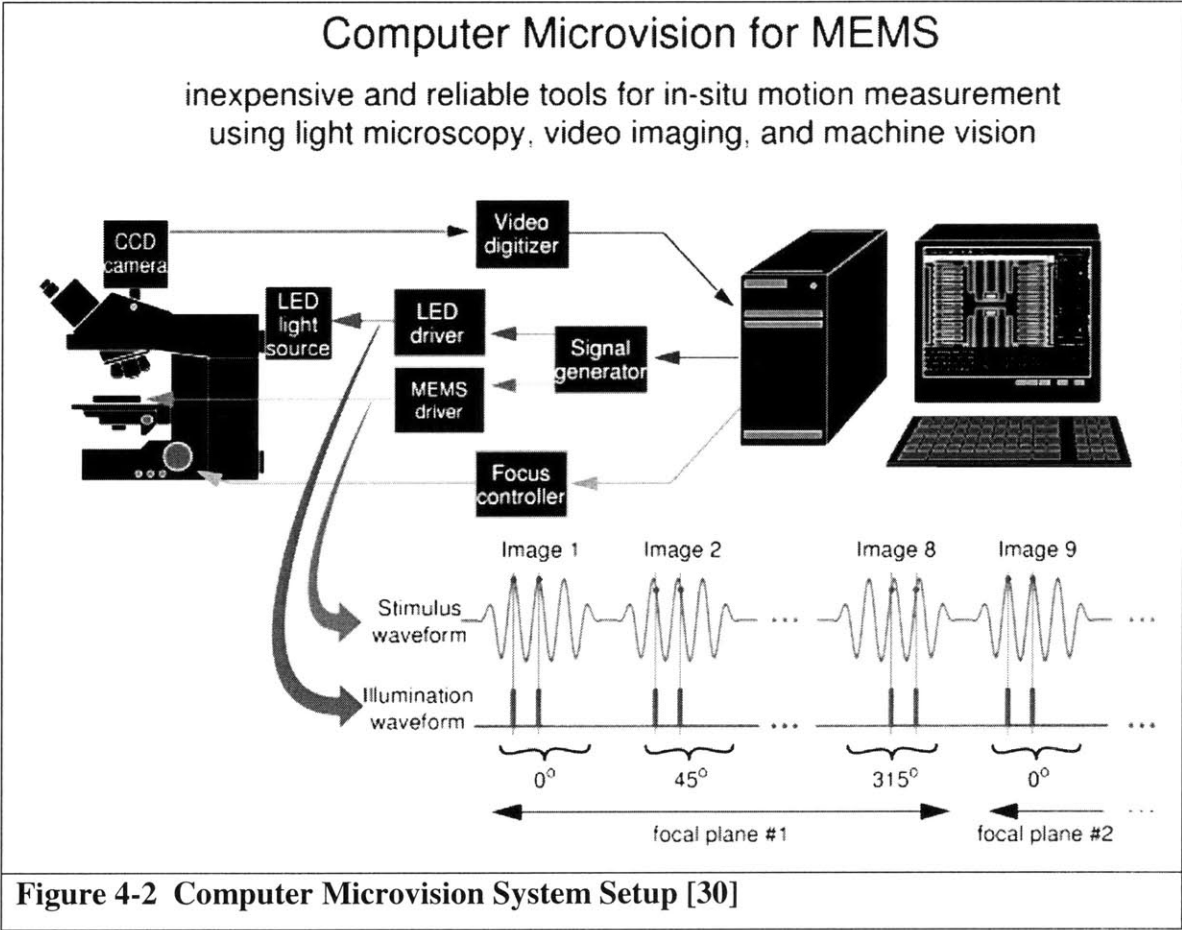
**Figure 4-1 Testing setup for Micro-Hexflex**

### 4.1.2 Dynamic Response

To test the dynamic response of Micro-Hexflex, the Computer Microvision System developed by Professor Dennis Freeman's group at MIT has been suggested. The Computer Microvision system has the ability to measure transient response with nanometer and milli-degree resolution. The measuring procedure is shown in Figure 4-2.



The magnified image data is collected through a microscope and recorded in the CCD camera. To detect the motion, stroboscopic illumination is used to take temporal sequence of images at multiple planes of focus. At each point of focus, images are taken at multiple stimulus phases that are in synchronization with the source signal generated by the computer. This process can be repeated at different frequencies and the images will be analyzed by Computer Microvision algorithm, which output the motion in three axes as a function of frequency [30]. Bode plots can then be generated and the dynamic characteristics of the system may be obtained. The Computer Microvision System has been used in many applications, including measuring 3D motion fatigue structures, mirror alignment in optical system, linear and non-linear behavior of a gyroscope [31].



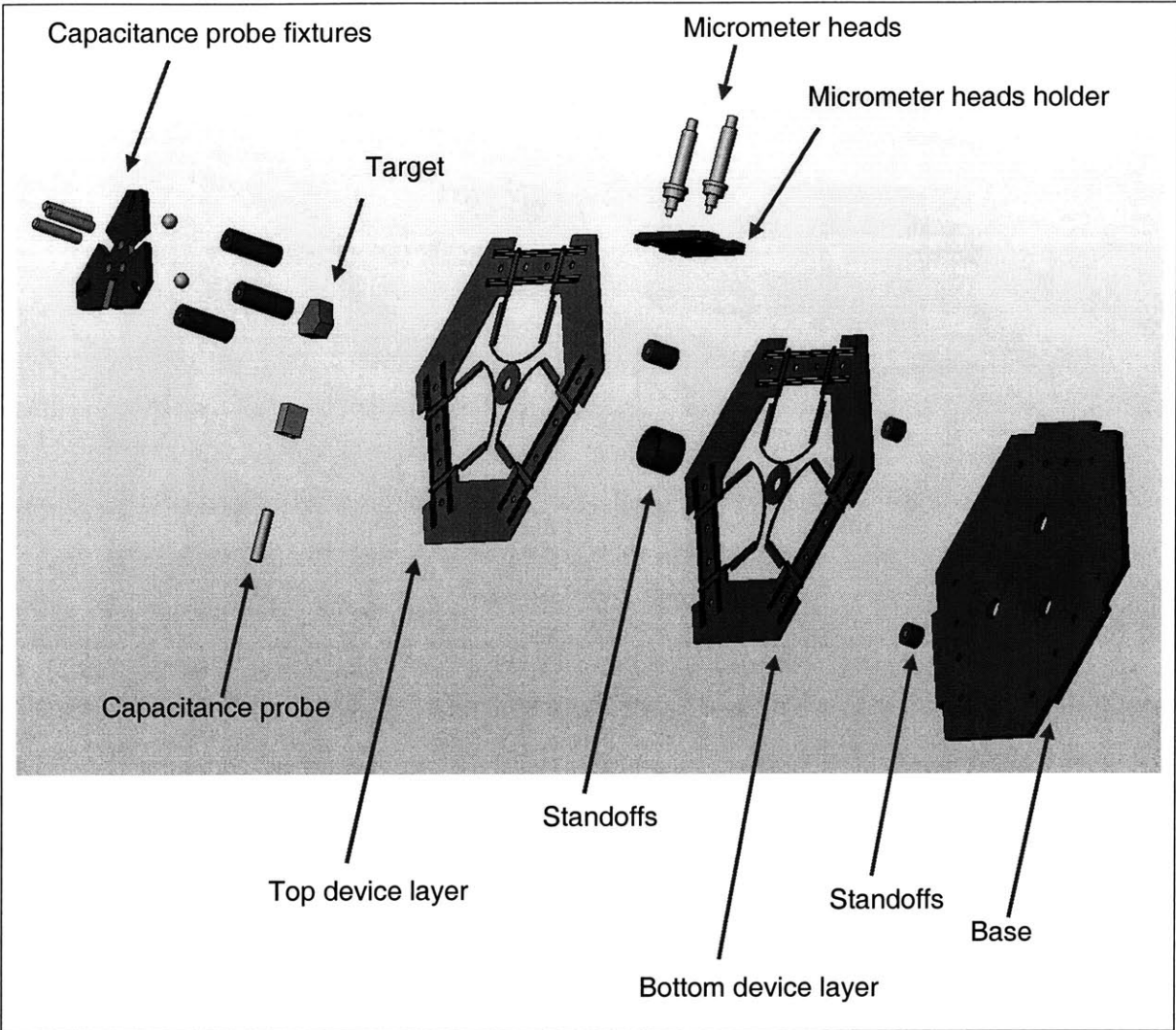
## 4.2 Testing of Macro-Scale Hexflex

To test and verify the feasibility of the dual-layerer concept, a macro-scale model of Micro-Hexflex was built and tested. The stage is built in two layers with one inch standoffs. An exploded view of the macro-scale model is shown in Figure 4-3. The original U-shaped thermal actuators are built-in to scale. However, they are actuated by micrometer heads (minimum increment 0.025 mm). Flexure designs are used to ensure that the kinematic behavior of the mechanism emulates micro-scale version.

Figure 4-3 consists of three sub-assemblies. The first part is the macro-scale Hexflex model, which is exploded into two device layers connected by twelve standoffs.

The second sub-assembly consists of the base and the micrometer head holder which positions the micrometer head in place for actuation.

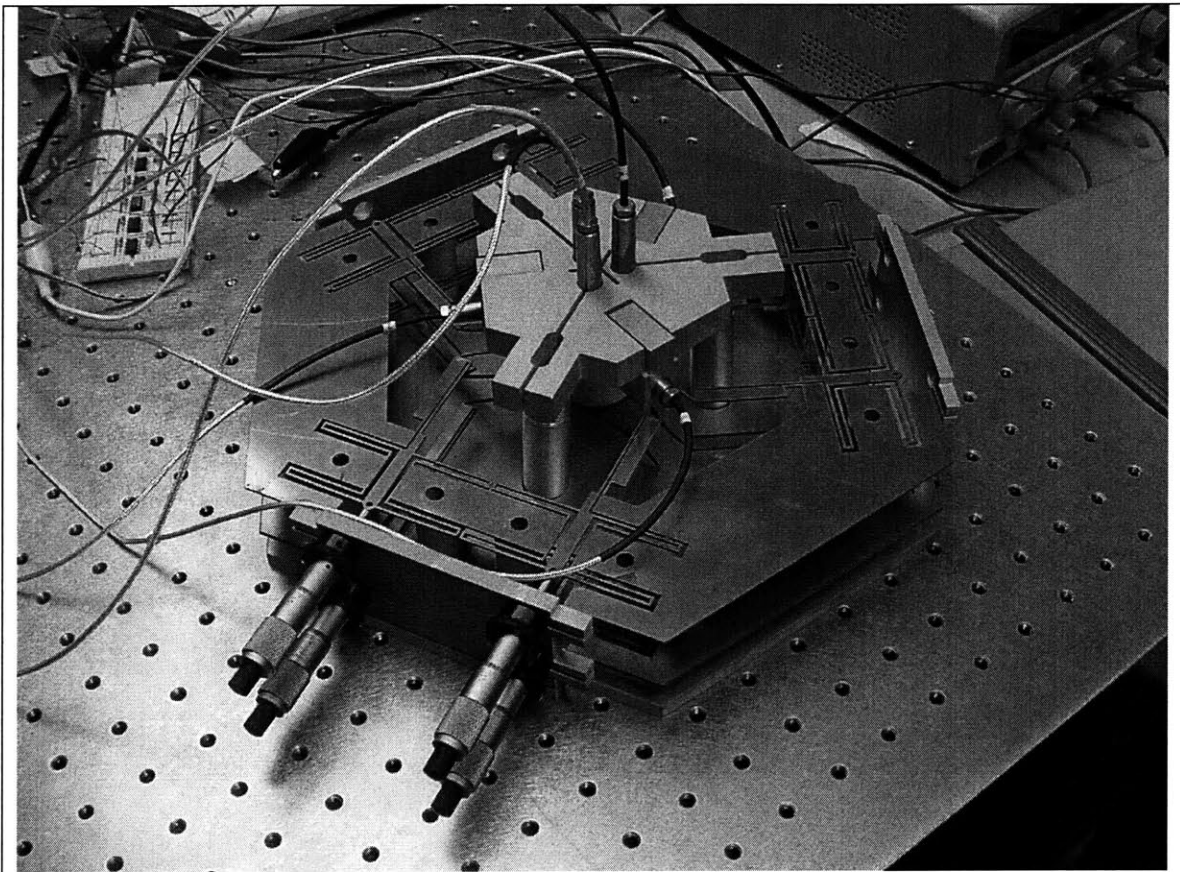
The third sub-assembly is the capacitance probe fixture assembly, which is designed to hold the capacitance probes in-place for displacement sensing. It includes three posts, each of which has a ball bearing on top. Through kinematic coupling theory, we know this probe fixture assembly will give a good repeatability and sustainable position. The detail dimensions of the macro-scale device layer are provided at Appendix B. The prototype was assembled together using hard-stops superglues.



**Figure 4-3 Exploded view of macro-scale testing model**

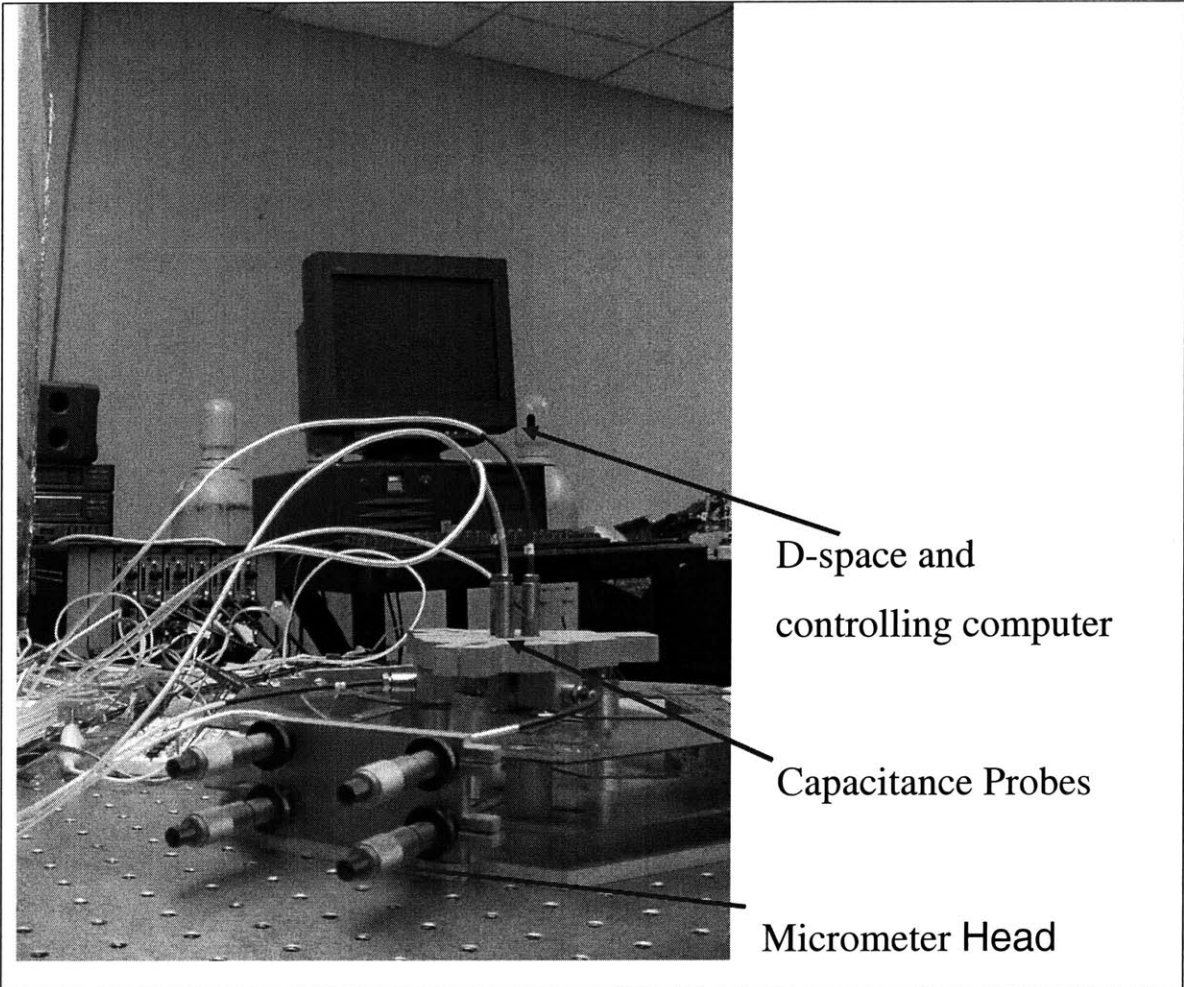
### 4.3 Macro-Scale Model Testing Setup

Figure 4-4 shows the testing setup. Six capacitance probes are used to measure displacements and rotations in six-degree-of-freedom.



**Figure 4-4 Macro-scale model testing setup**

As shown in Figure 4-5, the displacement and performance of the stage is measured by six Lion Precision capacitance probes, model C1-C. At high sensitivity, the resolution of these capacitance probes is 2.2 nanometers. The probe has a range of measurement of 125 microns. Data acquisition is obtained via D-Space and Matlab interfaces. The optical table is used to limit vibration error sources.



**Figure 4-5 Macro-scale model system setup**

## 4.4 Test Result from the Macro Model

To verify the performance of the macro stage, we test three of the major variables:

1. Displacement along Y axis
2. Out-of-plane displacement along Z axis
3. Rotational displacement around Z axis.

The results of the testing are plotted in Figure 4-6, Figure 4-7, Figure 4-8, and Figure 4-9. Figure 4-6 presents the testing result of the stage displacement along Y axis. Figure 4-6 is the original data taken from the capacitance probe. The data representing the top curve in Figure 4-6 shows theoretical solution obtained by a finite element analysis. This data has a slope (or stiffness)  $200 \text{ } [\mu\text{m}/100\mu\text{m}]$ . The constant in the linear equation comes from the micrometer head preload of the structure. Although the experimental data has a good linearity ( $R^2=0.99$ ), the slope of the two lines are differed by a factor of 6.5.

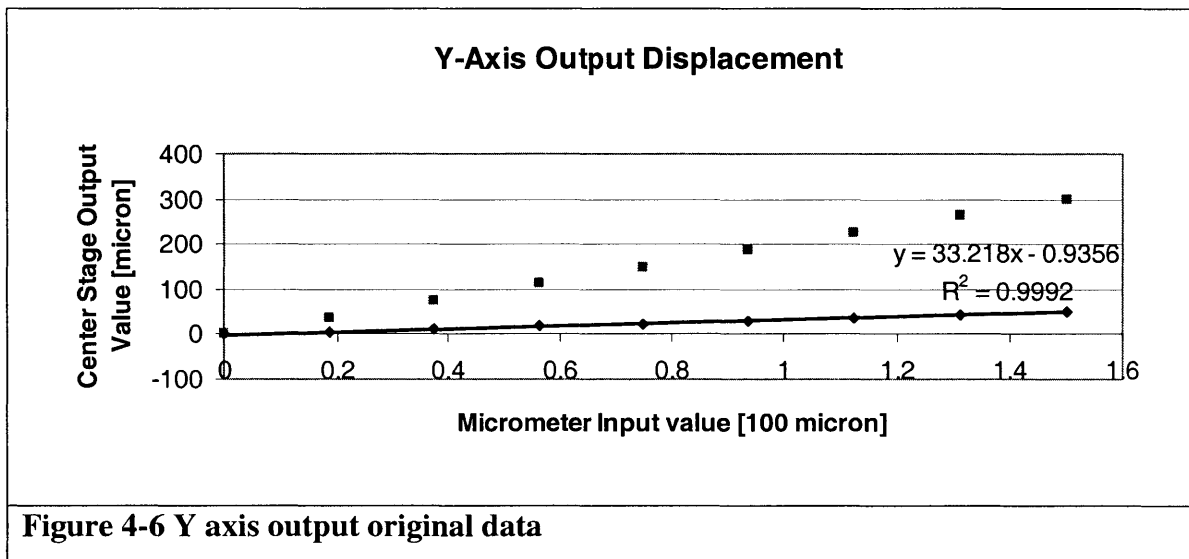
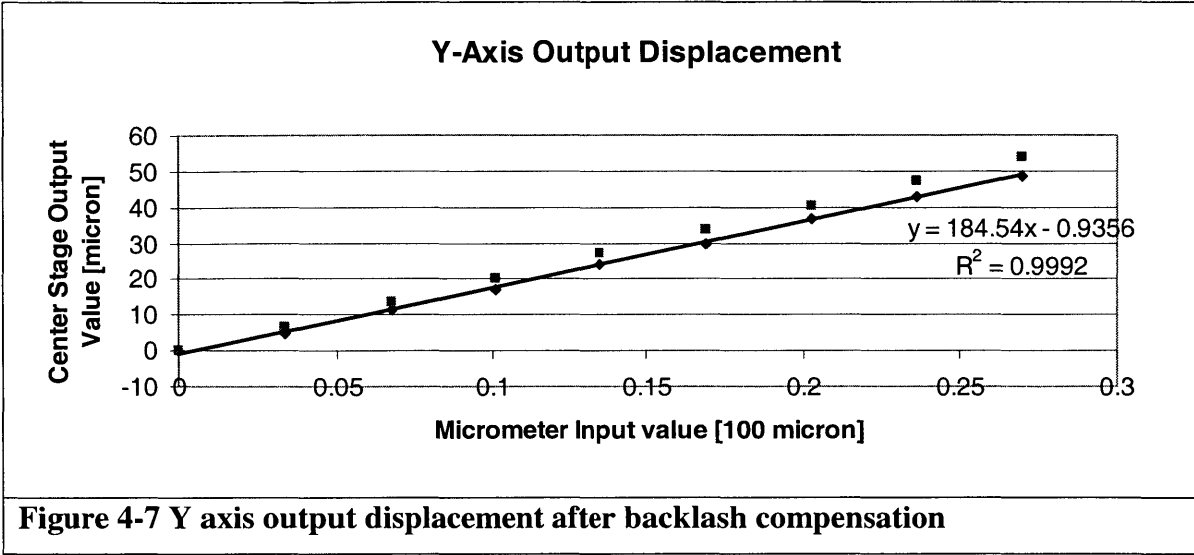


Figure 4-6 Y axis output original data

The reason of the data mismatch originates from the compliance of the micrometer holder. One of the reason could be the superglue connected joints (connects the micrometer head holder and the base) has a lower stiffness and thus affects the input actuation. If we do compensation adjustment, more accurate data can be obtained. The data after compensation computation is shown in Figure 4-7. A good linearity ( $R^2=0.99$ ) is

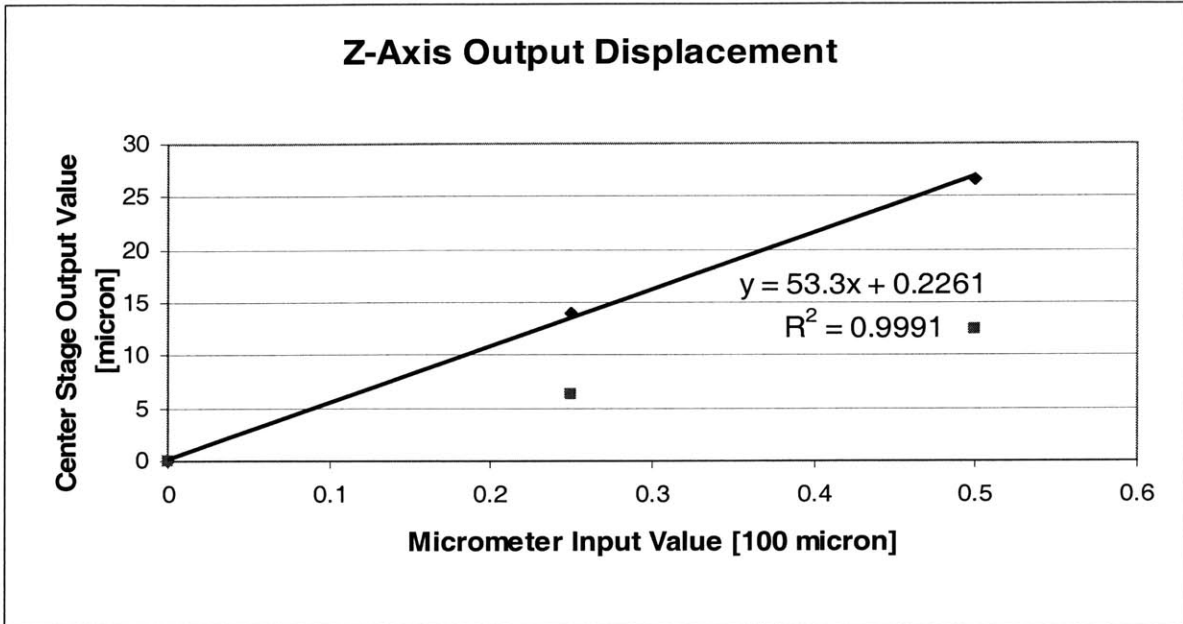
perceived throughout the testing range of fifty microns. Moreover, the ratio of the theoretical stiffness over experimental stiffness is now 1.08.



**Figure 4-7 Y axis output displacement after backlash compensation**

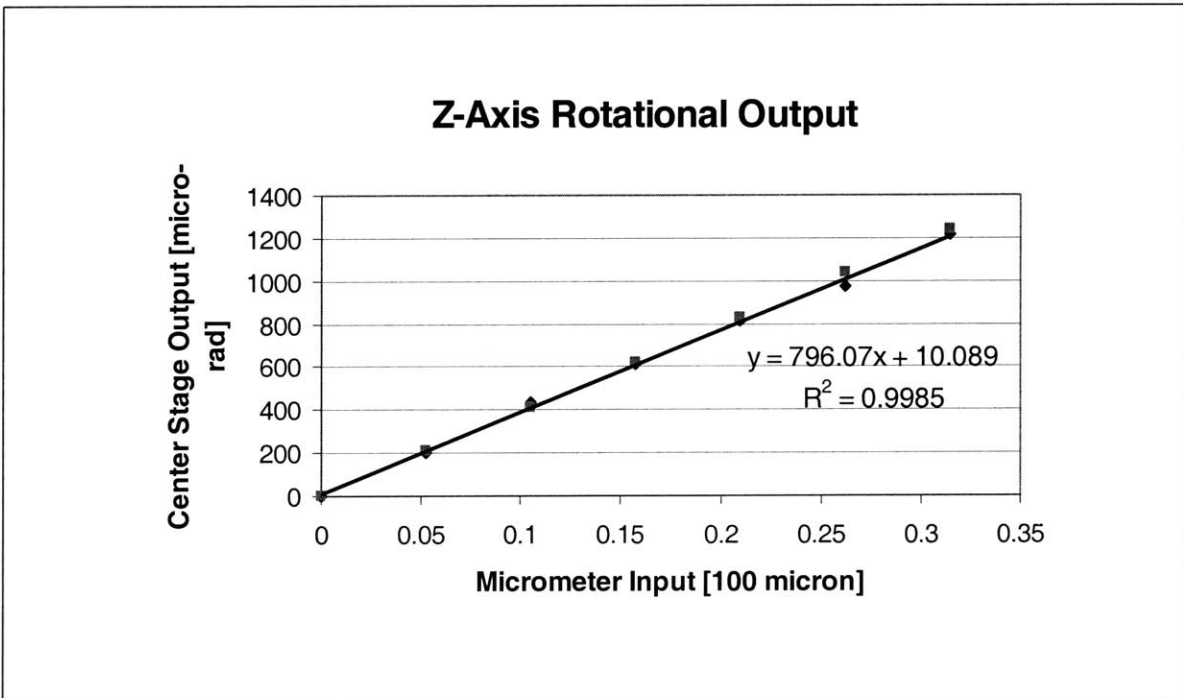
Figure 4-8 presents the testing result of the stage displacement along Z axis. This test also has a good linearity, with a  $R^2$  value of 0.99. In this case, compensation calculation can only reduce the amplification ratio of the experimental data to two, which is still larger than the finite element prediction. This means that the double-layered concept creates more than enough out-of-plane motion. We conclude two possible reasons for the unmatched results for out-of-plane case:

1. The inter-layer connections of the macro-scale version model are different from the micro-version, which are joined by silicon dioxide at both center stage and thermal actuators
2. The boundary constraint in the macro-scale model is a point/area type. The micro-scale device is fully constrained on all boundaries through silicon dioxide.



**Figure 4-8 Z axis output displacement**

Figure 4-9 presents the testing result of the counter-clockwise rotational displacement with respect to Z axis, which also possesses a high linearity of  $R^2 = 0.99$ . Again, using the data from the backlash, we compensate the errors. Thus, the result in Figure 4-9 matches the theoretical prediction quite well.



**Figure 4-9 Z axis rotational output**



# Chapter 5 Market Analysis

## 5.1 Potential Market

There is need for the in-package fiber alignment in the field of optical communication. Figure 5-1 shows a comparison of optical fiber assembly costs between: manual, automated, and an IPMA. From the figure, we know opportunity exists to save by replacing the current manual and automated dominant market.

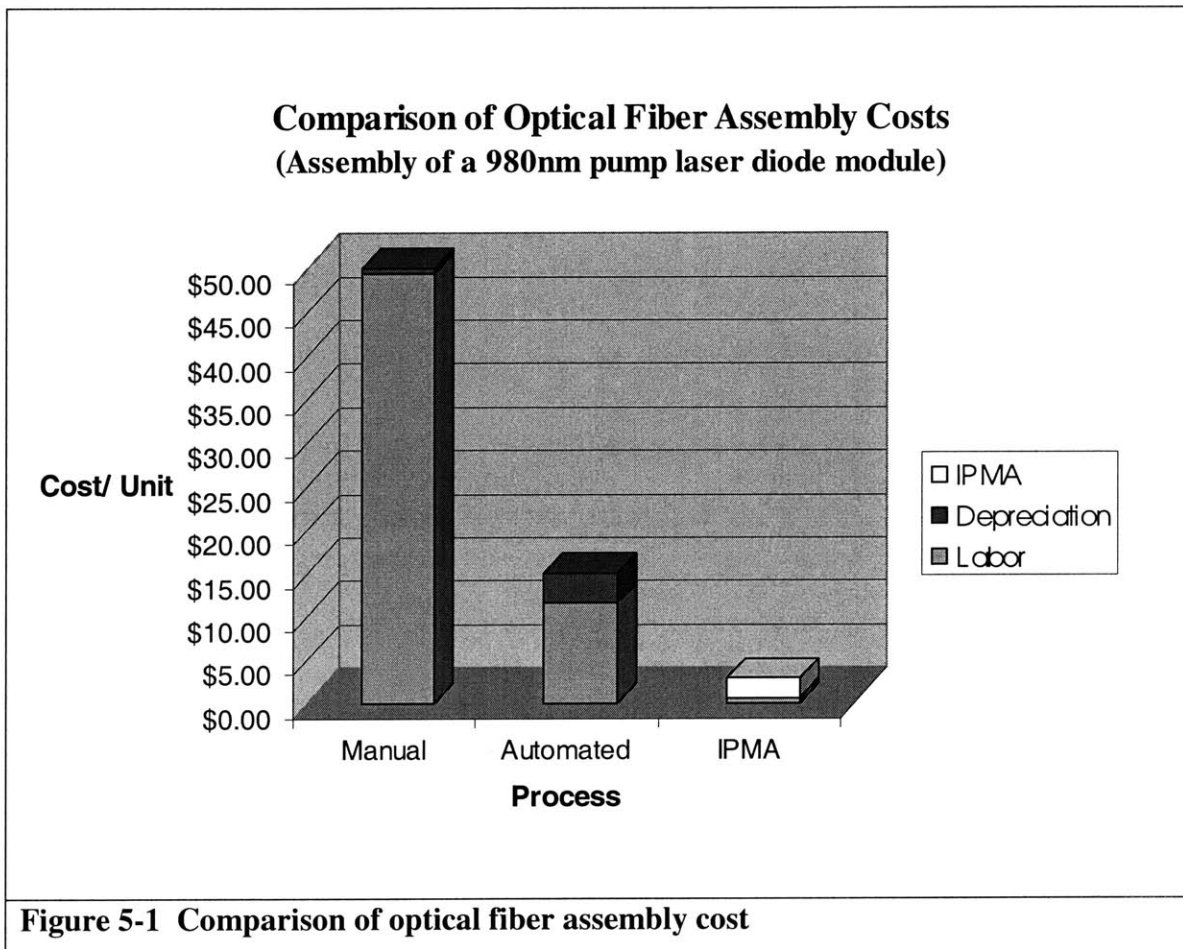


Table 5-1 shows major sectors of the optoelectronic industry [33].

<b>Table 5-1 Total world market (1997) for fiberoptic products in communication applications. CGAR= Compounded Annual Growth Rate.</b>			
Market Segment	Sales [\$Billions]	Percent Total [%]	Projected 5 Year CAGR [%]
Transmission Equipment	19.0	64	20
Optical Cable	6.8	25	12
Interconnect Hardware	1.8	7	20
Test and Measurement	0.8	4	23
Total	28.4	100	23

The Micro-Hexflex is designed to reduce the coupling loss (less than 0.1 dB), which will reduce the number of the required amplifiers.

## 5.2 Budget Analysis of Mass Fabrication: Micro-Hexflex

We will now examine whether the Micro-Hexflex will be a cost feasible solution to replace the current industry and product in a cost view.

During the initial stages of research and development, there is always a much higher cost to fabricate a device. The material costs for the second-generation Micro-Hexflex, for example, are listed in Table 5-2 and the process charge at MTL is listed in Table 5-3.

<b>Table 5-2 Cost for the material</b>				
Wafer Cost	Unit Price	Unit	Quantity	Price
4" SOIOI wafer	\$370	/wafer	1	\$370
4" Prime Wafer	\$25	/wafer	1	\$25
Mask Cost	Unit Price	Unit	Quantity	Price
soda lime mask	\$800		1	\$800
laser printing mask	\$70		3	\$210
<b>Sum</b>				<b>\$1,405</b>

Totaling the process cost from Table 5-2 to Table 5-3, we know the cost of a test version of Micro-Hexflex will totally add up to \$2,590. Each four-inch double SOI wafer includes 50 dies. As a result, each unit of Micro-Hexflex will cost \$51.8.

<b>Table 5-3 Process cost at MTL</b>				
Process Charge at MTL	Unit Price	Unit	Quantity	Price
STS1 (DRIE)	\$86.25	/run	4	\$345
Acidhood	\$143.75	/wafer	4	\$575
Coater/ Bake/ HMDS	\$0.00	/hour	4	\$0
Endura (metal sputtering)	\$40.25	/wafer	1	\$40
Asher (plasma clean)	\$28.75	/run	3	\$86

EV1(mask aligner)	\$34.50	/wafer	4	\$138
Sum				\$1,185

Now, we try to estimate the capital of the device on the base of an eight inch wafer, which is still the current industry standard. The assumptions are:

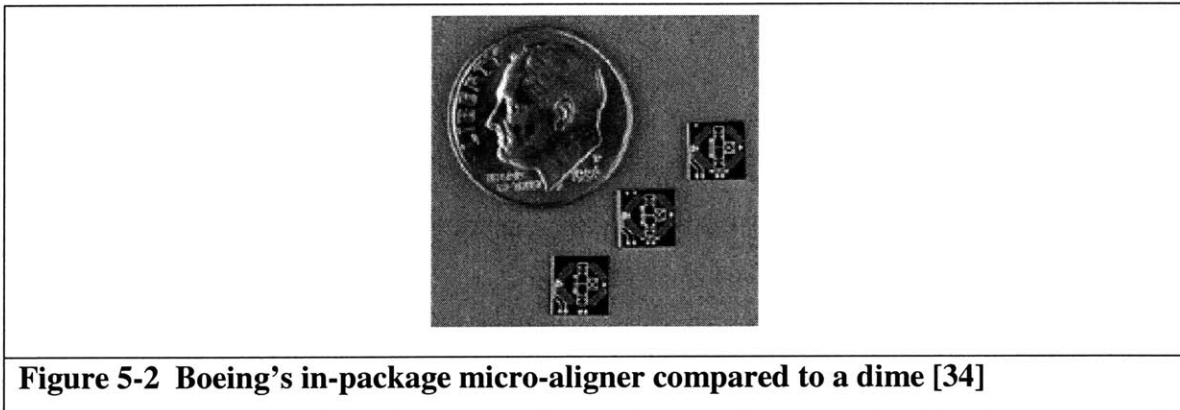
1. A three millimeter square die for each Micro-Hexflex
2. 60% effective area for each wafer
3. Capital of micro-fabrication base on MTL cost
4. Cost is estimated on the base of a single wafer processing

The results of the estimation are presented in Table 5-4. The assumptions of the capital estimation are conservative. The maximum cost is obtained by timing a 1.5 safety margin to the original capital, which is gained on the base of the assumptions above. As a result, each Micro-Hexflex should cost less than one dollar.

<b>Table 5-4 Product price estimation</b>				
	Functional area [mm <sup>2</sup> ]	Number of Micro-Hexflexs on a wafer	Percentage of effective area	Number of Hexflexs on a Wafer
8 inch wafer	31400	7850	60%	4710
Single Hexflex	4			
<b>Cost of a Single Hexflex Price</b>				
Maximum Cost			\$0.825	
Cost			\$0.550	

### 5.2.1 Case Study

The Micro-Hexflex is both less expensive and smaller in size than the existing in-package fiber alignment MEMS device designed by the Boeing Company. The maximum cost of a Micro-Hexflex is about one dollar (maximum) in comparison to three dollars, and the size of the whole package is about three millimeters in comparison to five, as shown in Figure 5-2.



# Chapter 6 Summary

---

## 6.1 Summary and Conclusion

Based on the Hexflex™ concept, a compliant six-degree-of-freedom device, a micro-scale version was designed to perform the in-package fiber alignment in Silicon Optical Bench technology. The impact of the device to the industry will be tremendous because it will change the way we perform active alignment with a low cost technology that conserves large amounts of energy.

In this thesis, the concept of Micro-Hexflex was made possible through careful selection and optimization of MEMS actuation and structure. Out-of-plane motion is achieved via a novel, double-layered silicon-silica-silicon structure. Both a simplified analytical solution and detailed finite element analysis are presented in the analysis part of this thesis. The micro-fabrication process of Micro-Hexflex and its packaging strategy are provided and discussed in detail in chapter three and four.

In the testing part, we successfully built and tested a macro-scale version of Micro-Hexflex, which proves the concept.

In the market analysis part, we concluded that the one-dollar Micro-HexFlex has excellent potential to affect the current industry.

## 6.2 Future Work

Within the limited time frame, it was not possible to fabricate a small-scale version of the Hexflex. New generations of Micro-Hexflex are scheduled to be fabricated in the near future.

# Reference

---

- [1] S.E. Miller, “*Integrated Optics: An Introduction*”, Bell Syst. Tech. J., Vol. 48, pp 2059-2068, 1969
- [2] Rao R. Tummala, “*Fundamentals of Microsystems Packaging*”, pp 472-473, McGraw-Hill, 2001
- [3] J. Sutherland et al., “Optical Coupling and Alignment Tolerances in Optoelectronic Array Interface Assemblies”, 1995 IEEE Electronic Components and Technology Conference.
- [4] Haake John M, “Micro-aligner for precisely aligning an optical fiber and an associated fabrication method,” US Patent, No. 6253011 B1.
- [5] Vusirikala, V.; Gopalan, B.P.; Kareenahalli, S.; Merritt, S.A.; Dagenais, M.; Wood, C.E.C.; Stone, D, “*GaAs-AlGaAs QW diluted waveguide laser with low-loss, alignment-tolerant coupling to a single-mode fiber*”,. IEEE Photonics Technology Letters , Volume: 8 Issue: 9 , Sep 1996, Page(s): 1130 -1132
- [6] Guckel, H.; Klein, J.; Christenson, T.; Skrobis, K.; Laudon, M.; Lovell, E.G., “*Thermo-magnetic metal flexure actuators,*” Solid-State Sensor and Actuator Workshop, 1992. 5th Technical Digest., IEEE , 22-25 Jun 1992 Page(s): 73
- [7] James M, Bustillo, Roger T. Howe, Richard S. Muller, “Surface Micromachining for Microelectromechanical Systems”, proceedings of the IEEE, Vol. 86, No. 8, August 1998.
- [8] DARPA, Computer Microvision for MEMS, 2001, <http://umech.mit.edu/MEMS/progress/rome/nov01.pdf>
- [9] Haake John M, Mark Beranek, “Integrated Microelectromechanical Alignment and Method for Fiber Optic Module Manufacturing,” US Patent No.: 6164837.
- [10] John M Haake, “Micro-aligner for precisely aligning an optical fiber and an associated fabrication method”, Patent No.: 6,253,011B1
- [11] Zhixiong Liu, Don L. DeVoe, “*Micromechanism fabrication using silicon fusion bonding*”, Robotics and Computer Integrated Manufacturing 17(2001) 131-137
- [12] Martin L. Culpepper, Gordon Anderson, “Design of a Low-cost Nano-manipulator

- Which Utilizes a monolithic, Spatial Compliant Mechanism”, Journal of Precision Engineering, 2002.
- [13] J. Sutherland, G. George, J.P. Krusius, “Optical coupling and Alignment tolerances in optoelectronic array interface assemblies,” Electronic Components and Technology Conference, 1996. Proceedings., 46th , 28-31 May 1996. Page(s): 480-486
- [14] Gordon’s Thesis
- [15] Guckel, H.; Klein, J.; Christenson, T.; Skrobis, K.; Laudon, M.; Lovell, E.G., “*Thermo-magnetic metal flexure actuators,*” Solid-State Sensor and Actuator Workshop, 1992. 5th Technical Digest., IEEE , 22-25 Jun 1992 Page(s): 73 -75
- [16] J.H. Comtois, M.A. Michalicek, C.C. Barron, “Fabricating Micro-Instruments in Surface-Micromachined Polycrystalline Silicon,” Proceedings of the 43<sup>rd</sup> International Society of America, 1997, Page: 169-179
- [17] Comtois, J.H.; Michalicek, M.A.; Barron, C.C “Characterization of electrothermal actuators and arrays fabricated in a four-level, planarized surface-micromachined polycrystalline silicon process,” Solid State Sensors and Actuators, 1997. TRANSDUCERS 97 Chicago., 1997 International Conference on , Volume: 2 , 16-19 Jun 1997
- [18] Stephen D. Senturia, “Microsystem Design”, p279-p282, Second Printing 2001
- [19] A.F. Mills, “Heat Transfer” second edition, 1999
- [20] K. Peterson, “Silicon as a Mechanical Material”, Proceedings of the IEEE, Vol 70, No. 5, May, 1982, pages 420-457.
- [21] H.-S. Moon, S.M. Spearing, et al.
- [22] Madou, “*Fundamentals of Micro Fabrication*”, p287-288, second edition, CRC, 2002.
- [23] W.A.Kern and C.A.Deckert, “Chemical Etching”, in *Thin Film Processing*, J.L. Vossen, ed., Academic, NewYork, 1978
- [24] S.M. Hu and D.R. Kerf, “Observation of Etching of n-type Silicon in Aqueous HF solutions”, *J. Electrochem. Soc.* 114:414 (1967)
- [25] Stephen A. Campbell, “*The Science and Engineering of Microelectronic*



*Fabrication*”, p258-260, second edition, Oxford, 2001.

- [26] F. Lärmer, A. Schilp: Method of Anisotropically Etching Silicon, US Patent #5501893, German Patent DE4241045
- [27] J.K. Bhardwaj, H. Ashraf: Advanced Silicon Etching Using High Density Plasmas, SPIE Proc. Series 2639 (1995) 224-233.
- [28] .K. Bhardwaj, H. Ashraf, A. McQuarrie: Dry Silicon Etching for MEMS, Symp. on Microstructures and Microfabricated Systems at the Annual Meeting of the Electrochem. Soc., Montreal, Quebec, Canada, May 4-9, 1997
- [29] Protron Mikrotechnik, 2003, <http://www.protron-mikrotechnik.de/>
- [30] DARPA, Computer Microvision for MEMS, 2001, <http://umech.mit.edu/MEMS/progress/darpa/feb01.pdf>
- [31] Computer Microvision for MEMS, 2001, <http://umech.mit.edu/MEMS.html>
- [32] QUID, 2003, <http://www.quid.com/ip/ipcs1.htm>
- [33] Rao R. Tummala, “Fundamentals of Microsystems Packaging”, pp 470-471, McGraw-Hill, 2001
- [34] SPIE Web, August, 1998, <http://www.spie.org/web/oer/august/aug98/home.html>

# Appendix A Multimode/ Single Mode Fiber Equations

---

## Multimode Fiber Equations<sup>3</sup>

### Transverse Offset

$$Loss = -10 \log \left( \frac{2}{\pi} \arctan \left( \frac{de}{x} \right) - \frac{2we}{\pi d} \right)$$

$$e = \left( 1 - \frac{y^2}{d^2} \right)^{0.5}$$

x = offset

d = core diameter

### Angular Misalignment

$$Loss = -10 \log \left( 1 - n_3 \frac{\theta}{\pi(N.A.)} \right)$$

$n_3$  = refractive index of gap

N.A. = numerical aperture

$\theta$  = angular misalignment

---

<sup>3</sup> Gilmore M, *Fibre Optic Cabling, Theory, Design and Installation Practice*, BH Newnes 1991, pp. 71, 73

## Separation

$$Loss = -10 \log \left( 1 - \frac{u(N.A.)}{2dn_3} \right)$$

u = separation

### 6.2.1 Single Mode Fiber Equations <sup>4</sup>

#### Size Mismatch

$$Loss \cong 4.343 \left( \frac{2(w_1 - w_2)}{w_1 + w_2} \right)^2$$

w<sub>1</sub> = mode field radius / spot size of fibre 1

w<sub>2</sub> = mode field radius / spot size of fibre 2

#### Transverse Offset

$$Loss \cong 4.343 \left( \frac{x}{w_0} \right)^2 \text{ [dB]}$$

w<sub>0</sub> = mode field radius / spot size

x = transverse offset

#### Longitudinal Separation

---

<sup>4</sup> Mickelson, A.R., Basavanhally, N.R., Lee, Y., "Optoelectronic Packaging" John Wiley & Sons, Inc., New York, p50

$$Loss \cong 5.3 \left( \frac{z\lambda}{10w_0^2} \right)^2 \text{ [dB]}$$

$z$  = longitudinal separation

$\lambda$  = wavelength

### **Angular Misalignment**

$$Loss \cong 8864 \left( \frac{w_0\theta}{10\lambda} \right)^2 \text{ [dB]}$$

$\theta$  = angular tilt [rad]

**Combined Loss equation [valid for individual losses < 1 dB<sup>5</sup>]**

$$Loss \cong 4.343 \left( \frac{x}{w_0^2} \right)^2 + 5.3 \left( \frac{z\lambda}{10w_0^2} \right)^2 + 8864 \left( \frac{w_0\theta}{10\lambda} \right)^2 \text{ [dB]}$$

---

<sup>5</sup> Jeunhomme, J.B., "Single-Mode Fiber Optics" Marcel Dekker, Inc., New York, 1983

# Appendix B Drawing of Macro-Scale Hexflex

